Material Properties of MBE Grown ZnTe, GaSb and Their Heterostructures for Optoelectronic Device Applications

by

Jin Fan

A Dissertation Presented in Partial Fulfillment
of the Requirements for the Degree
Doctor of Philosophy

Approved August 2012 by the
Graduate Supervisory Committee:

Yong-Hang Zhang, Chair
David Smith
Hongbin Yu
Jose Menendez
Shane Johnson

ARIZONA STATE UNIVERSITY

December 2012

ABSTRACT

Recently a new materials platform consisting of semiconductors grown on GaSb and InAs substrates with lattice constants close to 6.1 Å was proposed by our group for various electronic and optoelectronic applications. This materials platform consists of both II-VI (MgZnCdHg)(SeTe) and III-V (InGaAl)(AsSb) compound semiconductors, which have direct bandgaps spanning the entire energy spectrum from far-IR (~0 eV) up to UV (~3.4 eV). The broad range of bandgaps and material properties make it very attractive for a wide range of applications in optoelectronics, such as solar cells, laser diodes, light emitting diodes, and photodetectors. Moreover, this novel materials system potentially offers unlimited degrees of freedom for integration of electronic and optoelectronic devices onto a single substrate while keeping the best possible materials quality with very low densities of misfit dislocations. This capability is not achievable with any other known lattice-matched semiconductors on any available substrate.

In the 6.1-Å materials system, the semiconductors ZnTe and GaSb are almost perfectly lattice-matched with a lattice mismatch of only 0.13%. Correspondingly, it is expected that high quality ZnTe/GaSb and GaSb/ZnTe heterostructures can be achieved with very few dislocations generated during growth. To fulfill the task, their MBE growth and material properties are carefully investigated. High quality ZnTe layers grown on various III-V substrates and GaSb grown on ZnTe are successfully achieved using MBE. It is also noticed that

ZnTe and GaSb have a type-I band-edge alignment with large band offsets (ΔE_c=0.934 eV, ΔE_v=0.6 eV), which provides strong confinement for both electrons and holes. Furthermore, a large difference in refractive index is found between ZnTe and GaSb (2.7 and 3.9, respectively, at 0.7 eV), leading to excellent optical confinement of the guided optical modes in planar semiconductor lasers or distributed Bragg reflectors (DBR) for vertical-cavity surface-emitting lasers. Therefore, GaSb/ZnTe double-heterostructure and ZnTe/GaSb DBR structure are suitable for use in light emitting devices.

In this thesis work, experimental demonstration of these structures with excellent structural and optical properties is reported. During the exploration on the properties of various ZnTe heterostructures, it is found that residual tensile strains exist in the thick ZnTe epilayers when they are grown on GaAs, InP, InAs and GaSb substrates. The presence of tensile strains is due to the difference in thermal expansion coefficients between the epilayers and the substrates. The defect densities in these ZnTe layers become lower as the ZnTe layer thickness increases. Growth of high quality GaSb on ZnTe can be achieved using a temperature ramp during growth. The influence of temperature ramps with different ramping rates in the optical properties of GaSb layer is studied, and the samples grown with a temperature ramp from 360 to 470 ˚C at a rate of 33 ˚C/min show the narrowest bound exciton emission peak with a full width at half maximum of 15 meV. ZnTe/GaSb DBR structures show excellent reflectivity properties in the mid-infrared range. A peak reflectance of 99% with a wide

stopband of 480 nm centered at 2.5 μm is measured from a ZnTe/GaSb DBR sample of only 7 quarter-wavelength pairs.

ACKNOWLEDGMENTS

I express my sincere gratitude to my supervisor Prof. Yong-Hang Zhang for his guidance and supervision throughout my PhD study. He has been very patiently encouraging and supporting my research in many ways. I benefit significantly from his deep understanding of optoelectronic physics and the way how he applies the knowledge to solve a practical problem. I would like to show my profound obligation to Dr. David Smith for his plentiful help on electron microscopy studies and stimulating teachings on my research. I am also grateful to Dr. Xinyu Liu and Dr. Jacek Furdyna at University of Notre Dame, who spent lots of time and took great efforts in providing high quality molecular beam epitaxy grown materials for this work. I want to thank Dr. Jose Menendez for allowing me to use ellipsometer in his lab. I would also like to thank my other committee members, Dr. Hongbin Yu and Dr. Shane Johnson for their interest in my research and giving me advice.

Many colleagues and co-workers have helped me in several ways in my research work. I want to thank them all for the help, interest and team-support. Especially, I am obliged to Dr. Ding Ding, Dr. Lu Ouyang, Dr. Oray Orkun Cellek, Dr. Shiquing Yu, Dr. Jiangbo Wang, Dr. Songnan Wu, Dr. Shumin Wang, Dr. Xianfeng Lu, Dr. Qiang Zhang, Dr. Stuart Farrell, Dr. Vijay D'Costa, Dr. Benjamin Green, Dr. Elizabeth Steenbergen, Dr. Robin Scott, Dr. Jing-Jing Li, Mr. Junliang Chen and Mr. Michael DiNezza. In addition, I would like to acknowledge the use of facilities in the John M. Cowley Center for High

Resolution Electron Microscopy, the Center for Solid State Electronics Research, and the LeRoyEyring Center for Solid State Science at Arizona State University.

Above all, I would like to give special thanks to my wife Xiaoqian whose love, patience and understanding enabled me to complete this work. I am thankful to my parents for their love and sacrifices that have allowed their son to pursue his goals.

TABLE OF CONTENTS

Page

LIST OF TABLES viii

LIST OF FIGURES x

CHAPTER

1 INTRODUCTION 1

1.1 Background 1

1.2 6.1-Å II-VI and III-V materials platform 3

1.3 ZnTe and GaSb semiconductors 5

2 FUNDAMENTAL PRINCIPLES OF X-RAY DIFFRACTION AND PHOTOLUMINESCENCE TECHNIQUES 8

2.1 X-ray diffraction 8

2.2 Photoluminescence 19

3 GROWTH AND MATERIAL PROPERTIES OF ZnTe ON GaAs, InP, InAs, AND GaSb (001) SUBSTRATES 30

3.1 ZnTe virtual substrate 30

3.2 MBE growth of ZnTe virtual substrates 31

3.3 Characterization results and discussion 35

3.4 Summary 50

4 GROWTH AND MATERIAL PROPERTIES OF GaSb GROWN ON ZnTe 52

4.1 Motivation for GaSb grown on ZnTe 52

CHAPTER Page

4.2 MBE growth of GaSb on ZnTe 53

4.3 Characterization results and discussion..... 57

4.4 Summary 69

5 GaSb/ZnTe DOUBLE-HETEROSTRUCTURE..... 71

5.1 History of double-heterostructure..... 71

5.2 GaSb/ZnTe double-heterostructure structure 73

5.3 ZnTe/GaSb band offset..... 74

5.4 Critical thickness of ZnTe grown on GaSb 79

5.5 MBE growth of GaSb/ZnTe double-heterostructures 82

5.6 Characterization results and discussion..... 83

5.7 Summary 90

6 ZnTe/GaSb DISTRIBUTED BRAGG REFLECTORS..... 92

6.1 Vertical-cavity surface-emitting lasers..... 92

6.2 Distributed Bragg reflectors..... 94

6.3 Optical modeling for thin films 98

6.4 ZnTe/GaSb DBR modeling results and discussion..... 106

6.5 MBE growth of ZnTe/GaSb DBRs 110

6.6 Characterization results and discussion..... 111

6.7 Summary 117

7 CONCLUSION..... 119

REFERENCE 123

LIST OF TABLES

Table		Page
1.1	Conventional substrates used for various optoelectronic/electronic devices	3
1.2	List of devices and potential applications based on 6.1-Å materials system	5
1.3	Main parameters for four different AM0 four-junction solar cell designs ranging from the most practical Design I to optimal Design IV	6
2.1	Comparison among X-ray, electron, neutron diffractions	17
3.1	Growth parameters for ZnTe samples	34
3.2	Lattice parameters of ZnTe epilayers grown on different substrates	39
3.3	Lattice constants and thermal expansion coefficients of GaAs, InP, InAs, GaSb and ZnTe bulk materials	40
4.1	Growth parameters for GaSb samples	56
4.2	Simulation results of thicknesses for ZnTe and GaSb epilayers	62
5.1	Summary of theoretical and experimental h_c results for ZnTe grown on GaSb	82
5.2	Growth parameters for GaSb/ZnTe DH samples	83
6.1	Comparison of characteristics between VCSELs and stripe lasers	94
6.2	Comparison of DBRs used in NIR and MIR spectral range	97

Table Page

6.3 Comparison of different DBRs used for VCSELs emitting at 2.3 μm..... 110

6.4 Number of λ/4 pairs and layer thicknesses for the MBE grown ZnTe/GaSb DBR samples 111

LIST OF FIGURES

Figure		Page
1.1	Bandgaps of various II-VI and III-V alloys versus lattice constant.	4
2.1	Diffraction of an electromagnetic plan wave by crystal planes.	9
2.2	X-ray spectrum of copper at different accelerating voltages.	11
2.3	Schematic diagram for double-axis diffractometry.	17
2.4	Schematic diagram for triple-axis diffractometry.	19
2.5	(a) The absorption of a photon with upward energy transition. (b) The emission of a photon with downward energy transition.	20
2.6	Recombination of electron-hole pair.	20
2.7	Four basic transitions of SRH process: (a) hole capture, (b) hole emission, (c) electron emission, and (d) electron capture.	22
2.8	Schematic diagram for a PL system.	26
2.9	Experimental and fitting results of beam diameter measurement. The dots represent experimental data while the line represents the fitted curve.	27
2.10	The spectral irradiance of the standard tungsten-halogen lamp is measured when operated at 6.50 amperes DC. The spline curve is used to fit the experimental data.	28
2.11	Normalized throughput for the PL system with PMT detector from 300 nm to 900 nm.	29

Figure Page

2.12 Normalized throughput for the PL system with Ge detector from 600 nm to 1700 nm. 29

3.1 Dual-chamber MBE system..... 32

3.2 RHEED patterns for the growth of ZnTe/InAs (001) sample. 34

3.3 XRD pattern measured in the vicinity of the (004) and (311) diffraction peaks for ZnTe/GaSb (001) sample. The FWHMs of ZnTe and GaSb (004) diffraction peaks are 32.9 and 22.7 arcsec, respectively..... 35

3.4 XRD pattern measured in the vicinity of the (004) and (311) diffraction peaks for ZnTe/InAs (001) sample. The FWHMs of ZnTe and InAs (004) diffraction peaks are 59.9 and 30.5 arcsec, respectively..... 36

3.5 XRD pattern measured in the vicinity of the (004) and (311) diffraction peaks for ZnTe/InP (001) sample. The FWHMs of ZnTe and InP (004) diffraction peaks are 50.4 and 18.3 arcsec, respectively..... 36

3.6 XRD pattern measured in the vicinity of the (004) and (311) diffraction peaks for ZnTe/GaAs (001) sample. The FWHMs of ZnTe and GaAs (004) diffraction peaks are 45.0 and 22.1 arcsec, respectively..... 37

3.7 Layout of optical components in a TEM. 42

Figure Page

3.8 Low magnification TEM image of ZnTe/GaAs (001) sample. 44

3.9 High magnification TEM image of ZnTe/GaAs (001) sample with arrows pointing to dislocations. 44

3.10 High-resolution image showing ZnTe/GaAs interface with Burgers' circuit. S and F indicate the start and finish points for the Burgers' circuit analysis. 45

3.11 PL spectra of all the ZnTe samples measured at 300 K showing all the PL peaks positioned at 2.26 eV. 46

3.12 Temperature-dependent PL spectra of ZnTe/GaAs sample measured from 80 to 300 K. 47

3.13 Schematic diagram of ellipsometry measurement. 48

3.14 Experimental SE data and modeling result for ZnTe/InP sample..... 49

3.15 The real part of dielectric function (ε_1) for the ZnTe epilayers grown on GaSb, InP, GaAs substrates, and ZnTe bare substrate in the IR range from 2 μm to 30 μm. 50

4.1 GaSb sample structures grown under two different growth temperatures conditions, group A (left) and group B (right). 55

4.2 RHEED patterns for growth of GaSb on top of ZnTe. Patterns in upper and lower rows are referred to [110] and $[1\bar{1}0]$ axes, respectively. 57

Figure Page

4.3 Structures of sample #91118A, #91118B, and #91222D from left to right. 57

4.4 XRD (004) patterns for sample #91118A, #91118B, and #91222D. 58

4.5 XRD experimental data (in black) and simulated curve (in red) for sample #91118B. 59

4.6 Structures of sample #110131A, #110408B, and #110523A from left to right. 60

4.7 Experimental data (in black) and simulated curve (in red) of XRD (004) pattern for sample #110131A. Simulation result shows that the thicknesses for AlSb, ZnTe and GaSb layers are about 55, 325 and 410 nm, respectively. 60

4.8 Experimental data (in black) and simulated curve (in red) of XRD (004) pattern for sample #110408B. Simulation result shows that the thicknesses for ZnTe and GaSb layers are about 300 and 380 nm, respectively. 61

4.9 Experimental data (in black) and simulated curve (in red) of XRD (004) pattern for sample #110523A. Simulation result shows that the thicknesses for ZnTe and GaSb layers are about 280 and 380 nm, respectively. 61

4.10 Low-magnification TEM image of sample #110408B. 63

Figure Page

4.11 Low-magnification TEM image of sample #110523A. 64

4.12 PL spectra measured at 13 K with excitation density of 16 W/cm^2 for: (a) sample #91118B, (b) sample #110131A, (c) sample #110408B, and (d) sample #110523A. 66

4.13 Temperature-dependent PL spectra measured from 13 - 200 K with excitation density of 16 W/cm^2 for sample #110408B. 69

5.1 Energy band diagram at an abrupt interface (i) between a semiconductor and vacuum, metal, insulator, or a different semiconductor. 76

5.2 Energy band diagram at an abrupt interface between two semiconductors, X and Y. 77

5.3 Energy band diagram for ZnTe/GaSb (001) heterostructure. 78

5.4 XRD (004) ω-2θ curve for GaSb/ZnTe DH sample. 84

5.5 SEM image showing cross-section of GaSb/ZnTe DH sample. 85

5.6 Low-magnification TEM image of GaSb/ZnTe DH sample. 87

5.7 High-magnification TEM image of GaSb/ZnTe DH sample. 88

5.8 PL spectra for GaSb/ZnTe DH sample measured at 13 K and 30 K. 89

5.9 Temperature-dependent PL spectra for GaSb/ZnTe DH sample. 90

6.1 Schematic diagram of a typical VCSEL. 93

6.2 Reflection from a simple boundary. 99

Figure Page

6.3 Reflection and transmission for light of p-polarization. 100

6.4 Reflection and transmission for light of s-polarization. 100

6.5 Plane wave incident on a single layer film. 103

6.6 Refractive indices (*n*) for bulk ZnTe and GaSb. 107

6.7 Layer structure of the ZnTe/GaSb DBRs used in the calculation... 108

6.8 Calculated reflectivity spectra for ZnTe/GaSb DBRs..... 108

6.9 Peak reflectance versus number of λ/4 pairs. 109

6.10 Measured and simulated XRD patterns for a ZnTe/GaSb DBR with 7 pairs. 112

6.11 Cross-sectional SEM image of a ZnTe/GaSb DBR sample. 113

6.12 (a) AFM image for the surface of sample #4 (left). (b) AFM image for the surface of sample #5 (right). 113

6.13 Low-magnification TEM image of a DBR sample with 7 pairs..... 114

6.14 Reflectivity of Au in the range from 0.2 - 0.8 eV..... 115

6.15 Reflection signal measured from the Au film. 116

6.16 Reflection signal measured from a ZnTe/GaSb DBR sample. 116

6.17 Measured and simulated reflectance spectra for sample #5. 117

Chapter 1

INTRODUCTION

1.1 Background

Semiconductor optoelectronic materials and devices have experienced rapid development over several decades. The performance of almost all the optoelectronic devices has been improved by many orders of magnitude due to various innovative engineering designs and significant advancement in material quality. Nowadays, material quality, including crystallinity, background doping, uniformity, stability, etc., has become one of the most important aspects to achieve good device performance. Many material properties have to be considered in an optoelectronic device design, such as bandgap energies, lattice constants, band edge offsets, doping capability, carrier mobilities, refractive indices, thermal expansion coefficients, etc.

To achieve optoelectronic devices working in different spectral ranges, the choice of materials with suitable bandgaps is an important consideration. Meanwhile, to ensure a good device performance, it is highly desired to use materials with lattice constants matched or close to substrate lattice constant so that fewer dislocations can be generated during their epitaxial growth. Currently, there are only a few pairs of materials that have been found with lattice-matched structure and suitable bandgap energies for optoelectronic devices. To cover a spectral range from ultraviolet (UV) to infrared (IR), however, many material systems still have to be grown on different substrates. For example, blue light-

emitting diodes (LEDs) and UV photodetectors (PDs) based on nitride materials are grown on GaN, sapphire, or SiC substrates [1-7]; red and near infrared (NIR) laser diodes (LDs), and vertical-cavity surface-emitting lasers (VCSELs) are based on GaAs substrates [8-12]; most of 1.3 - 1.55 μm LDs and PDs for telecommunications are grown on InP substrates [13-15]; many quantum well infrared photodetectors (QWIPs) are grown on GaAs or InP [16-18]; type-II superlattices (T2SLs) for mid-wave infrared (MWIR) long-wave infrared (LWIR) detectors are based on GaSb and InAs [19-21]; and HgCdTe IR detectors are grown on CdZnTe, CdTe, GaAs, Si, and sapphire [22-25]. The substrates commonly used for various optoelectronic and electronic devices are summarized in Table 1.1.

Table 1.1. Conventional substrates used for optoelectronic/electronic devices.

Substrates / Devices	Sapphire/ Si	GaAs	InP	InAs	GaSb	CdZnTe/ InSb
HEMTs	X	X	X			
HBTs		X	X			
UV-Green LEDs/LDs	X					
NIR LEDs /LDs/PDs		X	X		X	
MWIR LDs			X	X	X	
QC/THz LDs		X	X		X	
VCSELs		X	X		X	
NIR PDs		X	X		X	
MWIR PDs				X	X	X (MCT/InSb)
LWIR PDs		X (QWIP)	X (QWIP)		X (T2SL)	X (MCT)

1.2 The 6.1-Å II-VI and III-V materials platform

Due to the diversity of materials and substrates being used for different devices, it is extremely challenging to integrate devices monolithically, as is the case for Si-based integrated circuits. To address and solve this fundamental problem, the so-called 6.1-Å II-VI and III-V materials system was recently proposed as a new platform containing latticed-matched materials with broad spectral range coverage [26]. This new materials system consists of both II-VI (MgZnCdHg)(SeTe) and III-V (InGaAl)(AsSb) semiconductors which have lattice constants closely matched to 6.1 Å. GaSb and InAs are used as substrates for this materials system. As shown in Figure 1.1, these semiconductor

compounds and their alloys have bandgaps covering the entire energy spectrum from far IR (~0 eV) to UV (~3.4 eV). The vertical line indicates the 6.1 Å lattice constant. It should be also noted that all the semiconductors in this system are direct bandgap materials with Zincblende (ZB) structure.

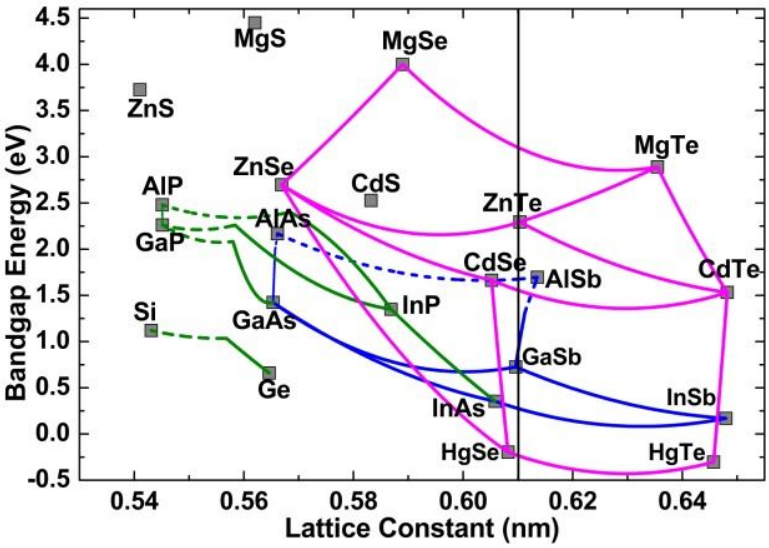

Figure 1.1. Bandgaps of various II-VI and III-V alloys versus lattice constant [27].

Due to the unique material properties as discussed above, the proposed 6.1-Å materials system can provide unlimited degrees of freedom for integrating almost all kinds of optoelectronic devices (such as photovoltaic devices, light emitting devices, and photodetectors), and some electronic devices (such as HEMTs and HBTs) onto a single substrate without generating large amount of misfit dislocations. Such features are lacking with any other latticed-matched semiconductor system/family. Based on the 6.1-Å materials system, a number of optoelectronic and electronic devices are proposed for various applications as listed in Table 1.2 [28].

Table 1.2. Devices and potential applications based on 6.1-Å materials system [28].

Devices	**Applications**
High efficiency multijunction solar cells	Space applications, terrestrial solar power stations
LEDs or LDs from green to MWIR	Bright light display, IR illumination, optical communication, remote chemical sensing
Monolithic integration of UV-green and IR photodetectors	FPAs, multicolor detection, broadband imaging
HEMTs and HBTs	Ultrahigh-speed electronics and circuits, low-noise preamplifiers

1.3 ZnTe and GaSb semiconductors

As discussed previously, the proposed devices based on the 6.1-Å materials system often contain one or more heterojunctions consisting of II-VI and III-V materials. For example, a four-junction solar cell designed for both space and terrestrial applications shows achievable efficiencies as high as 46% under 1 sun and 55% under 1000 sun [27]. The device structures are composed of two II-VI subcells and two III-V subcells, which are made by II-VI and III-V compounds and alloyed materials. The main design parameters, such as material compositions, bandgap energies, and junction thicknesses are shown in Table 1.3 [27].

Table 1.3. Main parameters for four different AM0 four-junction solar cell designs ranging from the most practical Design I to optimal Design IV [27].

Design I			Design II		
Material	E_g (eV)	d (μm)	Material	E_g (eV)	d (μm)
ZnTe	2.27	1.20	ZnTe	2.27	1.20
$Zn_{0.27}Cd_{0.73}Se_{0.66}Te_{0.34}$	1.71	1.20	$Zn_{0.27}Cd_{0.73}Se_{0.66}Te_{0.34}$	1.71	1.20
$Al_{0.41}Ga_{0.59}As_{0.03}Sb_{0.97}$	1.33	1.70	$Al_{0.41}Ga_{0.59}As_{0.03}Sb_{0.97}$	1.33	1.70
GaSb	0.72	2.10	$Al_{0.20}Ga_{0.80}As_{0.02}Sb_{0.98}$	1.04	2.30
Design III			Design IV		
Material	E_g (eV)	d (μm)	Material	E_g (eV)	d (μm)
$Zn_{0.92}Cd_{0.08}Se_{0.09}Te_{0.91}$	2.20	1.20	$Zn_{0.86}Cd_{0.14}Se_{0.14}Te_{0.86}$	2.14	1.20
$Zn_{0.10}Cd_{0.90}Se_{0.81}Te_{0.19}$	1.63	1.20	$CdSe_{0.90}Te_{0.10}$	1.56	1.30
$Al_{0.35}Ga_{0.65}As_{0.03}Sb_{0.97}$	1.25	1.75	$Al_{0.30}Ga_{0.70}As_{0.03}Sb_{0.97}$	1.18	2.10
$Al_{0.13}Ga_{0.87}As_{0.01}Sb_{0.99}$	0.94	2.40	$Al_{0.08}Ga_{0.82}As_{0.01}Sb_{0.99}$	0.86	2.50

To realize a solar cell with the above designed structures, it is important to study epitaxial growth of the II-VI/III-V heterostructure. Among all the semiconductors in the 6.1-Å materials system, the II-VI compound ZnTe and the III-V compound GaSb are almost perfectly lattice-matched to each other with a very small lattice mismatch of ~ 0.13%. Therefore, studies on the heterostructure formed by ZnTe and GaSb are necessary to be carried out as a first step which also instruct and help further studies on other 6.1-Å II-VI/III-V heterostructures of more complexity.

The growth of ZnTe/GaSb heterostructures has been studied for several decades [29]. Different growth techniques including RF sputtering [30], metalorganic chemical vapor deposition (MOCVD) [31], and metalorganic vapor phase epitaxy (MOVPE) [32] have been employed to grow ZnTe on GaSb. Molecular beam epitaxy (MBE) has also been used to grow these material systems, such as ZnTe grown with GaSb buffers on GaAs or GaSb substrates [33,34], and ZnTe with AlSb buffer on GaSb substrates [35]. To obtain high-quality materials for device applications such as solar cells, the study of ZnTe and

ZnCdTe/ZnTe quantum well structures grown on GaSb using MBE was also reported recently [36].

In this thesis work, several different heterostructures consisting of ZnTe and GaSb are proposed for various device applications. Comprehensive studies on their MBE growth and material properties are carried out. In Chapter 3, thick ZnTe grown on GaAs, InP, InAs and GaSb substrates as a virtual substrate is proposed to enable growth on large area substrates and reduce material cost. The MBE growth details and material properties are reported. In chapter 4, GaSb grown on ZnTe is studied for potential use in various electronic and optoelectronic devices. Successful growth of GaSb on ZnTe is achieved using a temperature ramp during the MBE growth. In Chapter 5, GaSb/ZnTe double-heterostructure (DH) is found to have unique properties suitable for light emitting devices. High quality GaSb/ZnTe DHs grown by MBE are experimentally demonstrated for the first time. In Chapter 6, a novel ZnTe/GaSb distributed Bragg reflector (DBR) is proposed for being used in vertical-cavity surface-emitting lasers (VCSELs) for mid-wave infrared (MWIR) optoelectronic applications. Excellent structural and optical properties of the ZnTe/GaSb DBRs are achieved and presented.

Chapter 2

FUNDAMENTAL PRINCIPLES OF X-RAY DIFFRACTION AND PHOTOLUMINESCENCE TECHNIQUES

X-ray diffraction (XRD) and photoluminescence (PL) are two commonly used techniques to study materials structural and optical properties. Both techniques are non-destructive and can be quickly and easily performed. It is necessary to discuss the fundamental principles of XRD and PL techniques before more detailed experimental results are present in the following chapters. In this chapter, the basic theory and physics of XRD and PL techniques, such as generation of X-ray, scattering processes of X-ray, configuration of X-ray diffraction, radiative/non-radiative recombination, and principles of a PL system are reviewed and discussed.

2.1 X-ray diffraction

2.1.1 Introduction of X-ray diffraction

X-ray diffraction (XRD) is a non-destructive characterization technique that can be used to acquire detailed information about chemical composition and crystallographic structure of natural/manufactured materials. Historically, X-ray was firstly discovered by Wilhelm Conrad Röntgen, which won him the Nobel Prize in 1895. The theoretical foundation for XRD was laid between 1895 and 1917 by several scientists, including Bragg [37], von Laue [38], Darwin [39] and Ewald [40]. In 1915, the Nobel Prize was given to William Henry Bragg and William Lawrence Bragg for their important theoretical achievements. In their

work, they proposed a famous equation to describe the crystal diffraction, which is denominated by their name --- "Bragg's law". The equation for Bragg's law is given by Equation (2.1)

$$2d\sin(\theta) = n\lambda, \tag{2.1}$$

where n is an integer, representing the order of diffraction; λ is the wavelength of X-ray; d is the interplanar spacing of the diffracting plane; θ is the glancing angle at which the X-ray is diffracted. Figure 2.1 schematically shows how the diffraction happens in a crystal. It can be easily seen that strong diffraction happens when Equation (2.1) is satisfied. To understand XRD from a physics point of view, it can be simply described as the followings: the X-ray beam strikes a three-dimensional atomic lattice and induces the emission of scattering waves at each atom. The summation of the amplitudes of all the scattering waves in all the space results in almost zero intensities in most directions but strong intensities in certain specific directions, where XRD happens.

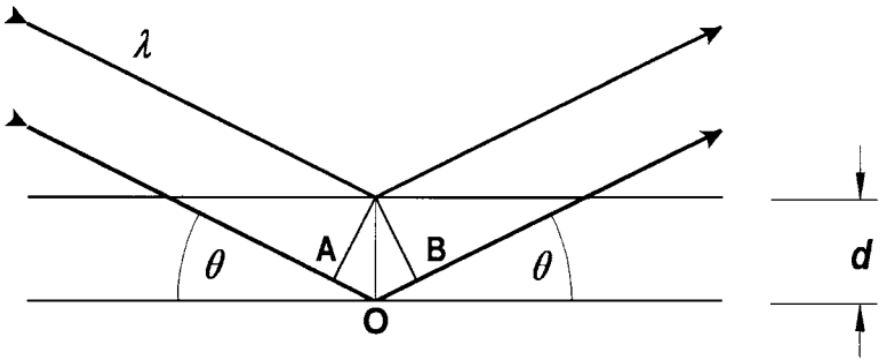

Figure 2.1. Diffraction of an electromagnetic plane wave by crystal planes.

2.1.2 Generation of X-rays

X-ray is one kind of electromagnetic radiation with wavelength in the range of 0.01 to 10 nm, shorter than ultraviolet (UV) ray and longer than Gamma ray. To generate electromagnetic radiation, one needs to accelerate or decelerate charged particles, leading to the emission of an electromagnetic wave with energy reaching X-ray region. In a laboratory generator, electrons are accelerated by a high voltage (~ 30 kV) towards a solid target. The emitted X-ray contains the line spectrum superimposed upon a continuous spectrum. The continuous spectrum is also called *Bremsstrahlung*, a German expression that means for "braking radiation". The line spectrum comes from the transitions of electrons between different energy levels in atoms. These lines are regarded as characteristics of one element and often used in X-ray fluorescence to identify elements present in a sample.

The characteristic lines are labeled with letter K, L, M, etc., which correspond to the labels of the electron shells to which transitions happen. The labels for these characteristic lines also consist of certain subscripts, such as α, β, etc., which indicate where transitions start. For example, one of the most popularly used radiations for XRD is the $K_{\alpha 1}$ line of copper. K_{α} means that the transition happens from L to K electron shell. Furthermore, the K_{α} line of copper is a doublet with separation about 4×10^{-3} Å. Thus, subscripts 1 and 2 are often included in the label ($K_{\alpha 1}$=1.54056 Å, $K_{\alpha 2}$=1.54439 Å) [41,42]. Since the intensity of $K_{\alpha 1}$ line is as twice as the intensity of $K_{\alpha 2}$ line, $K_{\alpha 1}$ line is chosen for XRD

measurement while $K_{\alpha 2}$ line is very often removed using a beam conditioner. Figure 2.2 shows a typical spectrum of X-ray emitted from copper.

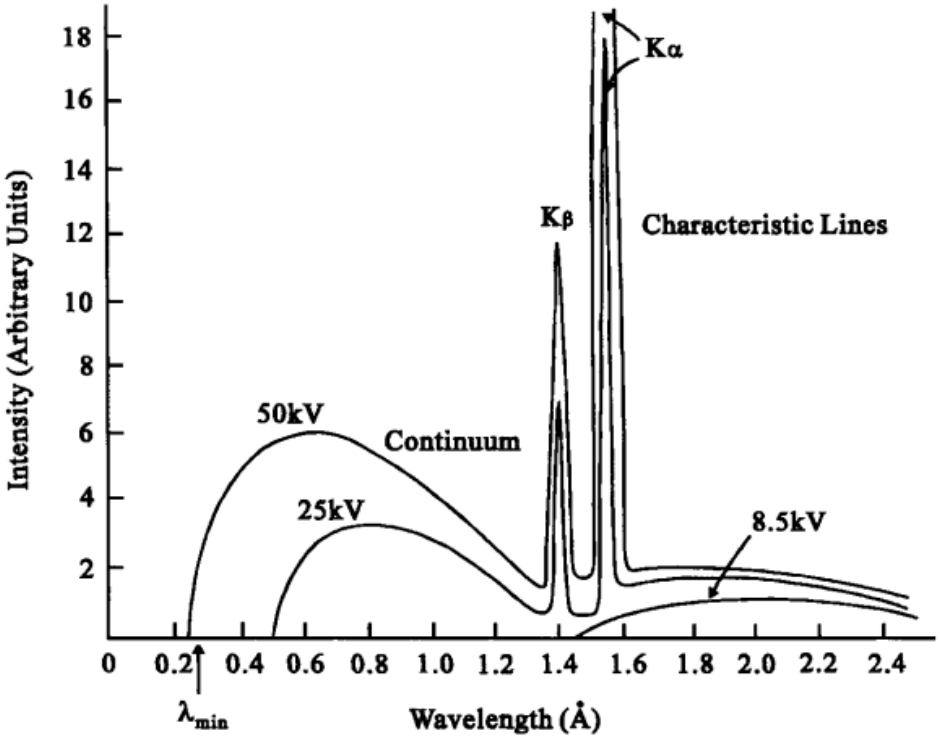

Figure 2.2. X-ray spectrum of copper at different accelerating voltages [43].

2.1.3 Scattering of X-rays by electrons, atoms, and unit cells

2.1.3.1 Scattering by electrons

As an electromagnetic wave, X-rays can be described by their electric field, of which the intensity is sinusoidally varying as a function of time at a given position. Therefore, after an X-ray beam is generated and encounters electrons, the X-ray beam could interact with electrons and make them oscillate. As a result, the oscillating electrons will emit another electromagnetic wave. This scattering process is also known as a "coherent scattering" process, which has two important properties: 1) the scattering beam has the same wavelength (or frequency) as the

incident beam; 2) there is a fixed phase shift between scattered beam and incident beam.

Compared with "coherent scattering", there is another different process how electrons can scatter X-rays, defined as "Compton Effect", which was discovered by Arthur Holly Compton in 1923. This effect occurs when the X-ray beam encounters loosely bound or free electrons. During the scattering process, some of the energy of the incident X-ray photon is transferred to the electron as kinetic energy so that the energy of the photon after impact ($h\nu_2$) is less than the energy before impact ($h\nu_1$, $h\nu_2 > h\nu_1$). Furthermore, there is no fixed relationship of phase change between incident beam and scattered beam. For this reason, it is also regarded as "incoherent scattering" process. Such a scattering cannot contribute to diffraction at all, because the phase is randomly related to the incident beam and does not make any contribution to the interference.

2.1.3.2 Scattering by atoms

When an X-ray beam encounters an atom, it will interact with each electron of the atom and its nucleus. Since the nucleus has much larger mass compared with that of an electron, the motion of nucleus can be ignored. Furthermore, the intensity of coherent scattering is inversely proportional to the square of the mass of scattering particles, as discovered by J. J. Thomson [44]. Therefore, the scattering of X-ray beam by an atom is only due to the electrons contained in that atom. For an atom which contains Z electrons, the total scattering amplitude by Z electrons cannot be simply added up at arbitrary angle,

because different electrons of an atom have different wave functions which introduce phase differences among the scattering waves. To describe the scattering of X-ray beam by an atom, atomic scattering factor is defined as Equation (2.2):

$$f = \frac{\text{amplitude of the wave scattered by an atom}}{\text{amplitude of the wave scattered by one electron}}. \qquad (2.2)$$

The atomic scattering factors can be calculated and have been reported for many elements [45,46].

2.1.3.3 Scattering by unit cells

For any material that has a Bravais lattice structure, unit cell is regarded as the basic unit which can be periodically repeated to produce the whole set of lattice points. Thus, how the atoms in a unit cell interact with the incident X-ray beam determines the final diffraction pattern. To describe the scattering of X-ray by a unit cell, structure factor is defined by adding all the waves scattered by individual atom in a unit cell. For a unit cell containing atoms, 1, 2, …, N, the structure factor (denoted as F) can be expressed by Equation (2.3):

$$F_{hkl} = \sum_{1}^{N} f_n e^{2\pi i(hu_n + kv_n + lw_n)}, \qquad (2.3)$$

where the summation is over all the N atoms of the unit cell; h, k, and l are Miller indices of diffracting lattice plane; u_n, v_n, and w_n are the coordinates of each atom in the unit cell. Generally, the structure factor F is a complex number whose amplitude represents the amplitude of the scattered wave while its non-zero phase representing the phase difference between the incident and diffracted waves.

Similar to atomic factor *f*, the absolute value of structure factor |*F*| can be expressed as Equation (2.4):

$$|F| = \frac{\text{amplitude of the wave scattered by all the atoms of a unit cell}}{\text{amplitude of the wave scattered by one electron}}. \quad (2.4)$$

2.1.3.4 Examples for structure factor calculation

a) The simplest unit cell which contains only one atom at origin (0 0 0)

The structure factor is

$$F = fe^{2\pi i(0)} = f, \quad (2.5)$$

which is independent of *h*, *k*, and *l*.

b) Base-centered unit cell which contains two atoms positioned at (0 0 0) and (1/2 1/2 0)

The structure factor is

$$F = fe^{2\pi i(0)} + fe^{2\pi i(h/2+k/2)} = f(1+e^{\pi i(h+k)}). \quad (2.6)$$

Since (*h*+*k*) is always an integer, the structure factor *F* can be simplified to:

$F = 2f$, when *h* and *k* are unmixed (if *h* and *k* are both even or both odd);

$F = 0$, when *h* and *k* and mixed (if *h* and *k* are one even and one odd).

c) Body-centered unit cell which contains two atoms positioned at (0 0 0) and (1/2 1/2 1/2)

The structure factor is

$$F = fe^{2\pi i(0)} + fe^{2\pi i(h/2+k/2+l/2)} = f(1+e^{\pi i(h+k+l)}). \quad (2.7)$$

Similarly, structure factor can be simplified to:

$F = 2f$, when (*h*+*k*+*l*) is even;

$F = 0,$ when (h+k+l) is odd.

d) Face-centered unit cell which contains four atoms positioned at (0 0 0), (1/2 1/2 0), (1/2 0 1/2), and (0 1/2 1/2)

The structure factor is

$$\begin{aligned} F &= fe^{2\pi i(0)} + fe^{2\pi i(h/2+k/2)} + fe^{2\pi i(h/2+l/2)} + fe^{2\pi i(k/2+l/2)} \\ &= f(1+e^{\pi i(h+k)} + e^{\pi i(h+l)} + e^{\pi i(k+l)}). \end{aligned} \tag{2.8}$$

The structure factor can be simplified to:

$F = 4f,$ when h, k, and l are unmixed indices;

$F = 0,$ when h, k, and l are mixed indices.

e) Unit cell of Zincblende lattice which contains eight atoms positioned at (0 0 0), (1/2 1/2 0), (1/2 0 1/2), (0 1/2 1/2), (1/4 1/4 1/4), (3/4 3/4 1/4), (3/4 1/4 3/4), and (1/4 3/4 3/4)

It has to be noted that many commonly used semiconductors in group IV, III-V, and II-VI have Zincblende structure, such as Si, Ge, GaAs, GaSb, ZnSe, ZnTe, etc. For general discussion, it is assumed that the unit cell is formed by two kinds of atom, A and B. Then the structure factor is

$$\begin{aligned} F &= f_A e^{2\pi i(0)} + f_A e^{2\pi i(h/2+k/2)} + f_A e^{2\pi i(h/2+l/2)} + \\ &f_A e^{2\pi i(k/2+l/2)} + f_B e^{2\pi i(h/4+k/4+l/4)} + f_B e^{2\pi i(3h/4+3k/4+l/4)} \\ &+ f_B e^{2\pi i(3h/4+k/4+3l/4)} + f_B e^{2\pi i(h/4+3k/4+3l/4)} \\ &= [1+e^{\pi i(h+k)} + e^{\pi i(h+l)} + e^{\pi i(k+l)}][f_A + f_B(e^{\pi i(h/2+k/2+l/2)})]. \end{aligned} \tag{2.9}$$

The structure factor can be simplified to:

$F = 0$, when h, k, and l are mixed indices;

$F = 4[f_A + f_B(e^{\pi i(h/2+k/2+l/2)})]$, when h, k, and l are unmixed indices.

$$I \propto |F|^2 = F^* \cdot F = 16[f_A^2 + f_B^2 + 2 f_A f_B \cos\frac{\pi}{2}(h+k+l)].$$

This result can be further simplified as below:

$|F|^2 = 16(f_A^2 + f_B^2)$, if ($h$+$k$+$l$) is odd ($h$, k, and l are unmixed indices);

$|F|^2 = 16(f_A^2 - f_B^2)$, if ($h$+$k$+$l$) is 2 × odd ($h$, k, and l are unmixed indices);

$|F|^2 = 16(f_A + f_B)^2$, if (h+k+l) is 2 × even (h, k, and l are unmixed indices).

Based on the results derived on the unit cells of face-centered and Zincblende structures, it can be seen that all the diffraction from lattice planes of mixed indices will be forbidden, which is often used as an important fact to identify a face-centered or Zincblende lattice structures. In addition, for Zincblende structure if A and B are the same atom, such as Si or Ge, f_A will be equal to f_B. Then diffraction from certain lattice planes will be also forbidden when (h+k+l) is 2 × odd, such as (002), (222), and (024), etc.

2.1.4 Comparison of different diffractions

Besides X-ray diffraction, a few other diffractions, such as electron diffraction, neutron diffraction, and atom diffraction, are also used to study structural properties. Since the characteristics of these probes are different with respect to their elastic and inelastic interaction with solid material, their areas of application are also different. Table 2.1 shows the comparison of the characteristics of X-ray, electron, and neutron diffractions.

Table 2.1. Comparison among X-ray, electron, neutron diffractions.

Characteristics	**X-rays**	**Electrons**	**Neutrons**
Absorption	Low	High	Very low
Penetration depth	~ mm	< 1 μm	~ cm
Resolution	arc seconds	10^{-3} rad	< arc second
Strain sensitivity	10^{-6}	10^{-4}	10^{-7}
Spatial resolution	1 μm	0.1 nm	30 μm
Destructive	No	Yes	No

2.1.5 High resolution X-ray diffraction system

Figure 2.3 shows the basic elements of a high-resolution X-ray diffractometer. After X-ray beam is generated, a beam conditioner is used to control the angle spread and energy divergence of the X-ray beam. The specimen is held in a plate which is adjusted with proper angles, including incident angle (ω), tilted angle (ψ) and rotation angle (φ), so that the normal to the diffracting lattice plane lies accurately in the diffraction plane. Finally, a detector integrates all the diffraction intensity over its acceptance angle.

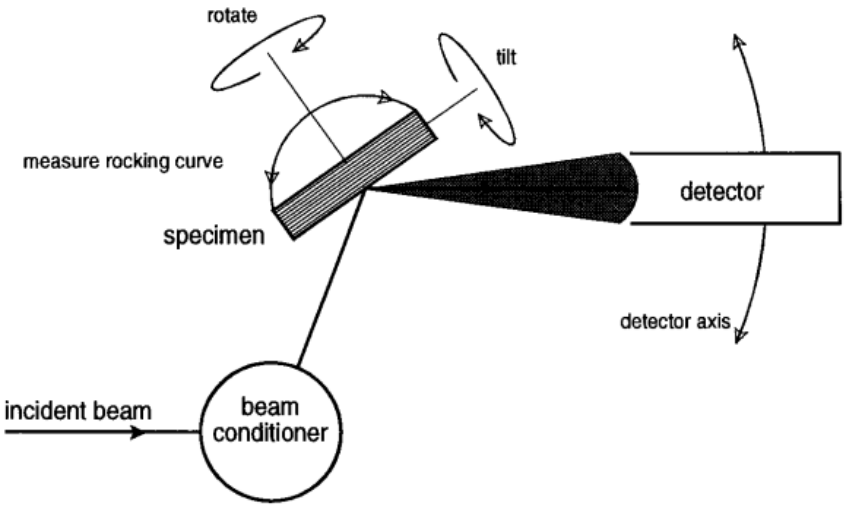

Figure 2.3. Schematic diagram for double-axis diffractometry [43].

The configuration of a XRD system, as shown in Figure 2.3, is often called “double-axis”. The first axis is the beam conditioner which adjusts and collimates the X-ray beam. The second axis is the scan of the specimen through Bragg angle. Since the double-axis diffractometry are quite rapid, easy, and very sensitive to strains, it has become a dominant technique for material study [47,48].

Triple-axis diffractometry can be considered as an extension of double-axis diffractometry in which an analyzer crystal is placed before the detector. The analyzer is also regarded as the third axis. Compared with a double-axis system, which has an open detector to collect the intensity over all the accepted angles, the analyzer in triple-axis system can significantly narrow the angular acceptance to the diffracted beam so that the information of strains and tilts in specimen can be acquired and distinguished [49]. By using triple-axis diffractometry, complete two-dimensional reciprocal-space maps can be obtained, which can provide detailed information for studies on strain distribution, mosaic spread, and lattice tilt, etc [50]. Figure 2.4 shows the configuration of triple-axis diffractometry system.

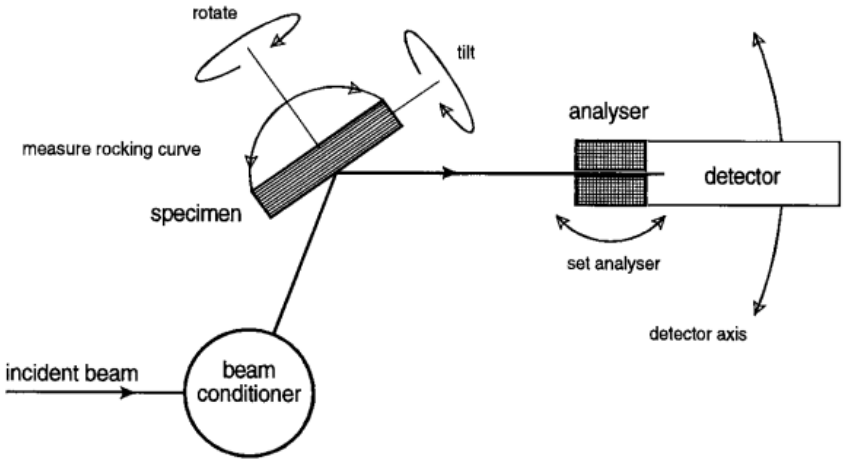

Figure 2.4. Schematic diagram for triple-axis diffractometry [43].

2.2 Photoluminescence

2.2.1 Introduction of photoluminescence

Photoluminescence (PL) is a non-destructive technique to characterize optical properties of materials. For semiconductors, PL measurement has been widely applied to extract various material parameters, such as bandgap, ionization energy of dopant atoms, shallow/deep impurity energy levels, band edge offset, strain, internal quantum efficiency, etc. From quantum physics point of view, the PL process can be simply described as two steps: 1) an upward energy transition excited by an incoming photon; 2) then a downward energy transition accompanied with emission of a photon. Figure 2.5 shows a schematic diagram for the absorption and emission of a photon through an energy transition between two states.

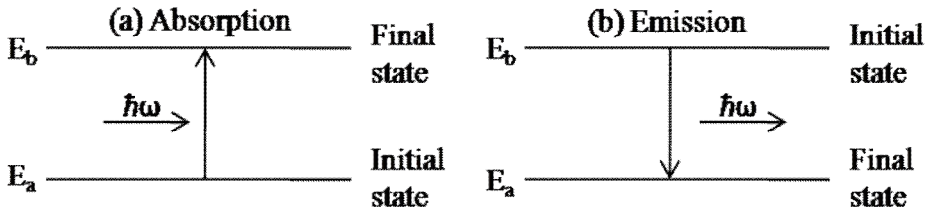

Figure 2.5. (a) The absorption of a photon with upward energy transition. (b) The emission of a photon with downward energy transition.

2.2.2 Radiative, Shockley-Read-Hall, and Auger recombinations

For a typical PL measurement, a laser which is often used as the excitation source emits monochromatic light with photon energy $hv > E_G$, generating electron-hole pairs within semiconductors. The electron-hole pairs recombine via radiative and non-radiative processes.

For radiative recombination, electrons and holes recombine directly from the conduction band to the valence band with emission of photons, as shown in Figure 2.6.

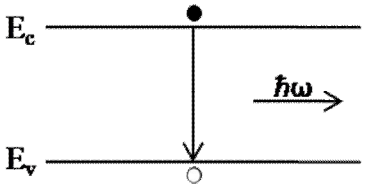

Figure 2.6. Recombination of electron-hole pair.

Since the radiative recombination involves both electrons and holes, the recombination rate is proportional to the product of the electron and hole concentrations, as shown in Equation (2.10) [51]

$$R_{rad} = c(np - n_0 p_0), \tag{2.10}$$

where c is capture coefficient; n_0 and p_0 are the electron and hole concentration generated at thermal equilibrium status, satisfying $n_0 p_0 = n_i^2$. Under light

irradiation, excess electrons (Δn) and holes (Δp) are generated equally, resulting in $n = n_0 + \Delta n$, $p = p_0 + \Delta p$, $\Delta n = \Delta p$. Based on Equation (2.10), the radiative recombination rate is simplified to Equation (2.11)

$$R_{rad} = B[(n_0 + p_0)\Delta n + \Delta n \Delta p] = \Delta n / \tau_{rad} , \tag{2.11}$$

where $\tau_{rad} = 1/[B(n_0 + p_0 + \Delta n)]$, representing the lifetime of radiative recombination. It can be seen that the radiative recombination lifetime is inversely proportional to the carrier density. For low-level injection, Δn and Δp are far less than n_0 and p_0. Then the radiative recombination rate can be approximately expressed by Equation (2.12):

$$R_{rad} \cong B(n_0 + p_0)\Delta n = \Delta n / \tau_{rad} , \tag{2.12}$$

where $\tau_{rad} \cong 1/[B(n_0 + p_0)]$.

For high-level injection, similarly the radiative recombination rate can be expressed by Equation (2.13):

$$R_{rad} \cong B(\Delta n \Delta p) = \Delta n / \tau_{rad} , \tag{2.13}$$

where $\tau_{rad} \cong 1/(B \cdot \Delta n)$.

For non-radiative recombination, two main recombination mechanisms are Shockley-Read-Hall (SRH) and Auger processes. In 1952, the SRH model was first introduced to describe the recombination of electron-hole pairs through the mechanism of trapping [52]. The SRH recombination process is illustrated in Figure 2.7.

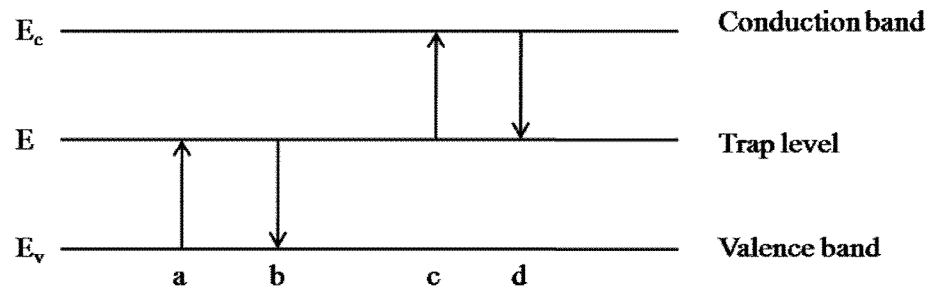

Figure 2.7. Four basic transitions of SRH process: (a) hole capture, (b) hole emission, (c) electron emission, and (d) electron capture.

In the SRH model, the recombination rates for each transition from (a) to (d) are given as following [52]:

$$R_a = c_p p N_t f_t, \tag{2.14}$$

$$R_b = -e_p N_t (1 - f_t), \tag{2.15}$$

$$R_c = -e_n N_t f_t, \tag{2.16}$$

$$R_d = c_n n N_t (1 - f_t), \tag{2.17}$$

where c_n and c_p are the capture coefficients for electrons and holes, respectively; N_t is the concentration of the trap states; f_t is the occupation probability of the trap states. Since the transition (b) and (c) generate holes and electrons, there is a minus sign ("-") in each mathematical expression. Based on Equation (2.14) – (2.17), the net recombination rates for holes and electrons are:

$$R_a + R_b = -e_p N_t (1 - f_t) + c_p p N_t f_t, \tag{2.18}$$

$$R_c + R_d = -e_n N_t f_t + c_n n N_t (1 - f_t). \tag{2.19}$$

For an intrinsic semiconductor under equilibrium status, both of the net recombination rates for electrons and holes are equal to zero. Therefore, we have

$$R_a + R_b = R_c + R_d = 0, \tag{2.20}$$

and Fermi-Dirac distribution holds

$$f_t = \frac{1}{1+\exp(\frac{E_t - E_i}{kT})}. \tag{2.21}$$

By solving Equation (2.20), f_t can be expressed by

$$f_t = \frac{c_n n + c_p p}{c_n(n+n_1) + c_p(p+p_1)}, \tag{2.22}$$

where $n_1 = n_i \cdot \frac{1-f_t}{f_t} = n_i \cdot \exp(\frac{E_t - E_i}{kT})$, $p_1 = n_i \cdot \frac{f_t}{1-f_t} = n_i \cdot \exp(-\frac{E_t - E_i}{kT})$.

Finally, the net recombination rate is given by Equation (2.23):

$$R_a + R_b = R_c + R_d = \frac{np - n_i^2}{\tau_p(n+n_1) + \tau_n(p+p_1)}, \tag{2.23}$$

where $\tau_p = \frac{1}{c_p N_t}$ and $\tau_n = \frac{1}{c_n N_t}$, representing lifetimes for holes and electrons, respectively.

Similar to the discussion on radiation recombination, excess electrons (*Δn*) and holes (*Δp*) are generated equally under light irradiation ($n = n_0 + \Delta n,\ p = p_0 + \Delta n$). Therefore, based on Equation (2.23) the SRH recombination rate can be expressed as

$$R_{SRH} = \frac{(n_0 + p_0 + \Delta n)\cdot \Delta n}{\tau_p(n_0 + n_1 + \Delta n) + \tau_n(p_0 + p_1 + \Delta n)} = \frac{\Delta n}{\tau_{SRH}}, \tag{2.24}$$

where $\tau_{SRH} = \dfrac{\tau_p(n_0 + n_1 + \Delta n) + \tau_n(p_0 + p_1 + \Delta n)}{n_0 + p_0 + \Delta n}$, representing the lifetime of SRH recombination. For low-level injection, the SRH recombination rate can be approximately determined by Equation (2.25):

$$R_{SRH} \cong \frac{(n_0 + p_0)\cdot \Delta n}{\tau_p(n_0 + n_1) + \tau_n(p_0 + p_1)} = \frac{\Delta n}{\tau_{SRH}}, \tag{2.25}$$

where $\tau_{SRH} \cong \dfrac{\tau_p(n_0 + n_1) + \tau_n(p_0 + p_1)}{n_0 + p_0}$. For high-level injection, the SRH recombination rate can be approximately expressed by Equation (2.26):

$$R_{SRH} \cong \frac{\Delta n}{\tau_p + \tau_n} = \frac{\Delta n}{\tau_{SRH}}, \tag{2.26}$$

where $\tau_{SRH} \cong \tau_p + \tau_n$.

During the recombination of an electron-hole pair, the recombination energy can be absorbed by another carrier so that the third carrier is excited to a higher energy state. This process is called Auger recombination. Since Auger process involves three carriers, its recombination rate can be expressed by Equation (2.27) [53]

$$R_{Auger} = (C_p p + C_n n)\cdot(np - n_i^2), \tag{2.27}$$

where C_p and C_n are the Auger recombination coefficients for holes and electrons, respectively. As one of the most important non-radiative recombination mechanism in semiconductors, Auger recombination was confirmed both experimentally [54-56] and theoretically [57,58]. Its effect is only significant when the carrier concentration is very high, which can be achieved by high

doping densities or high excess carriers. Under high-level injection, the Auger recombination rate can be simplified to Equation (2.28):

$$R_{Auger} \cong (C_p + C_n) \cdot (\Delta n)^3 = \frac{\Delta n}{\tau_{Auger}}, \qquad (2.28)$$

where $\tau_{Auger} \cong \frac{1}{(C_p + C_n) \cdot (\Delta n)^2}$, representing the lifetime of Auger recombination. It can be seen that the lifetime of Auger recombination has $1/n^2$ dependence.

2.2.3 Photoluminescence system

As shown in Figure 2.8, a PL system typically consists of an optical source, a collection system and a detection system. Based on different research purposes, a PL system can consist of different types of optics, optical/electrical instruments with varied configuration. The commonly used excitation source is a laser which can emit photons with energy (hv) greater than the required transition energy. The collection system may consist of various optical components to collect PL emission, such as lenses, mirrors, filters, beam-splitter, monochromator, spectrometer, interferometer, etc. The detection system can contain photodetectors, computer controls and some electronic instruments such as lock-in amplifier, photon counter, boxcar, etc.

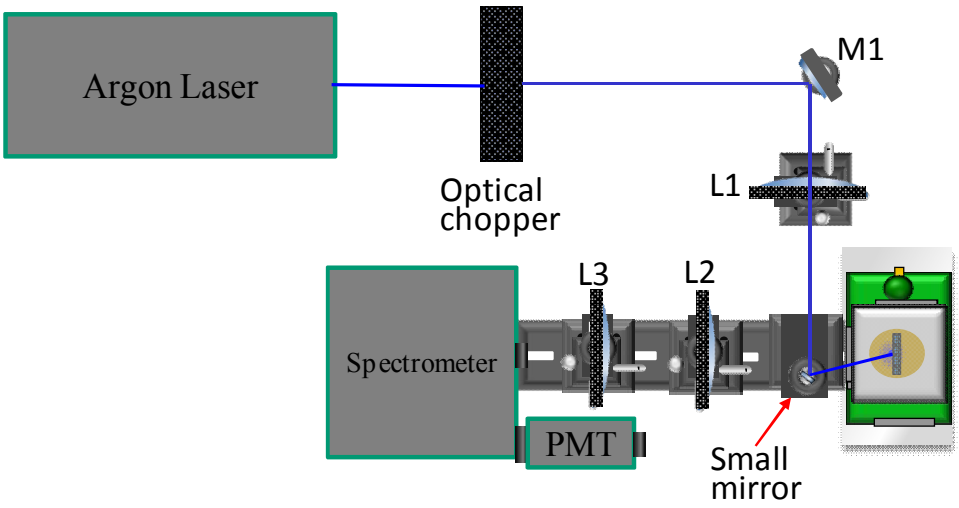

Figure 2.8. Schematic diagram for a PL system.

During PL measurement, the excitation density is an important parameter which can directly affect PL spectrum. It is defined as "excitation density = total power of laser irradiation / total irradiation area". Although the diameter of a laser beam is on the order of millimeter, the irradiation area on the sample can be very small after the beam is focused by lenses or mirrors. To determine the diameter of the focused laser beam, the laser intensity is measured while the beam is partially blocked by a moveable blade. The transmitted laser intensities are recorded as the blade moves. The measured data for a blue laser diode emitting at 410 nm is plotted in Figure 2.9. Cumulative distribution, shown in Equation (2.29), is used for curve fitting

$$I(x) = \frac{1}{2}[1 + erf(\frac{x-\mu}{\sigma\sqrt{2\pi}})]. \qquad (2.29)$$

The best fit is obtained with σ = 87.267 ± 0.559 μm. It can be inferred that 95% power is inside the area with diameter of 5σ, which is about 431.3 μm.

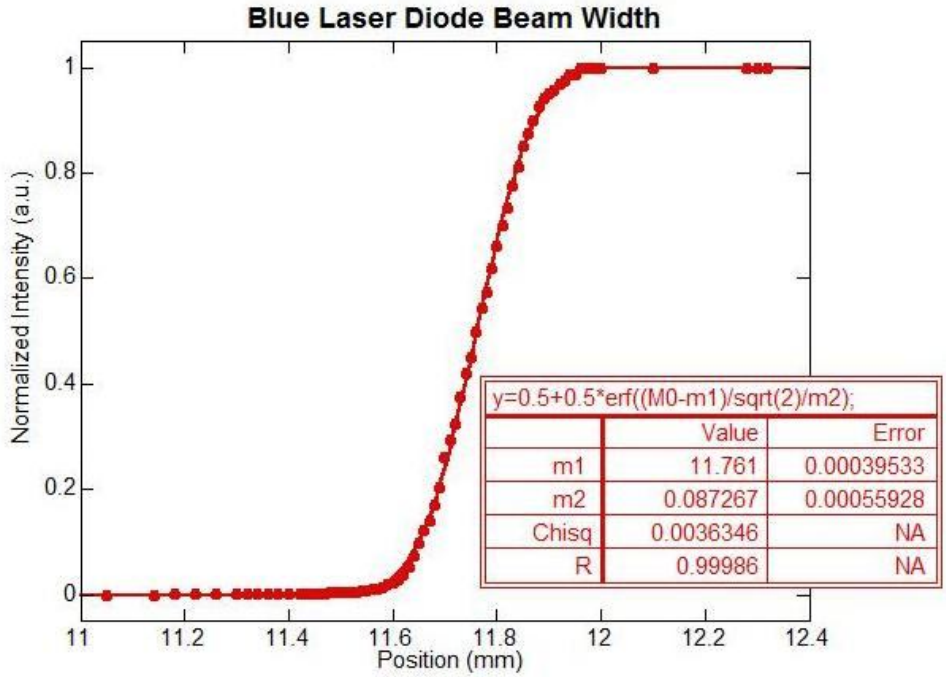

Figure 2.9. Experimental and fitting results of beam diameter measurement. The dots represent experimental data while the line represents the fitted curve.

In a PL system, many of the optical components such as gratings, mirrors, lenses, detectors, etc., have spectrally varying response. Therefore, it is necessary to calibrate the spectral responsivity of the whole PL system, which is defined as "throughput". By measuring a calibrated tungsten-halogen lamp whose spectrum is known, the throughput can be determined by Equation (2.30)

$$\text{Throughput} = \frac{I_{\exp}(\lambda)}{I_{lamp}(\lambda)}, \tag{2.30}$$

where $I_{exp}(\lambda)$ represents the measured spectrum of the tungsten-halogen lamp, $I_{lamp}(\lambda)$ represents the calibrated spectrum of the tungsten-halogen lamp. The spectral irradiance of the tungsten-halogen lamp is provided by the manufacturer, as shown in Figure 2.10.

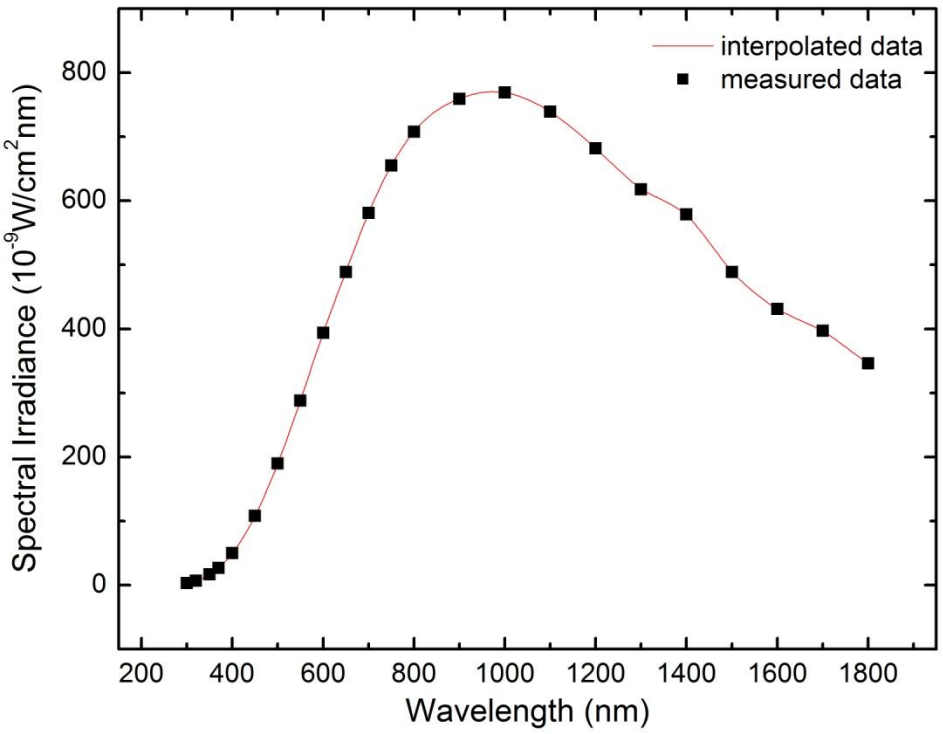

Figure 2.10. The spectral irradiance of the standard tungsten-halogen lamp is measured when operated at 6.50 amperes DC. The spline curve is used to fit the experimental data.

The PL system used in this study is equipped with a photomultiplier tube (PMT) and a Ge photodetector. The normalized throughputs for the whole PL system working with PMT and Ge detectors are shown in Figure 2.11 and Figure 2.12, respectively. It can be seen that the effective spectral range of the PL system is 500 - 900 nm with the PMT detector, and 600 - 1700 nm with the Ge detector.

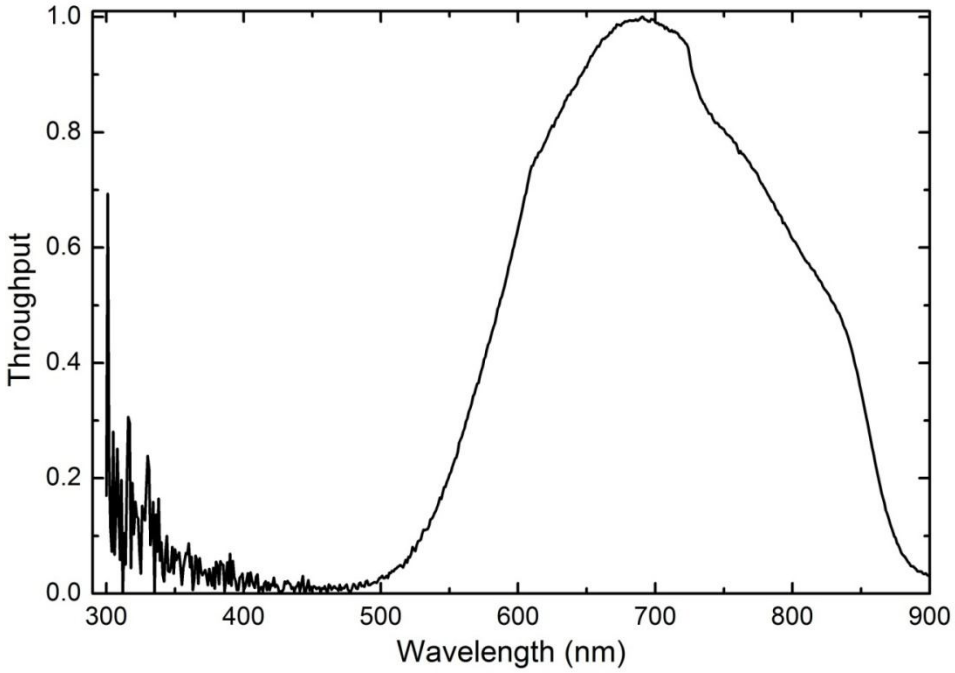

Figure 2.11. Normalized throughput for the PL system with PMT detector from 300 nm to 900 nm.

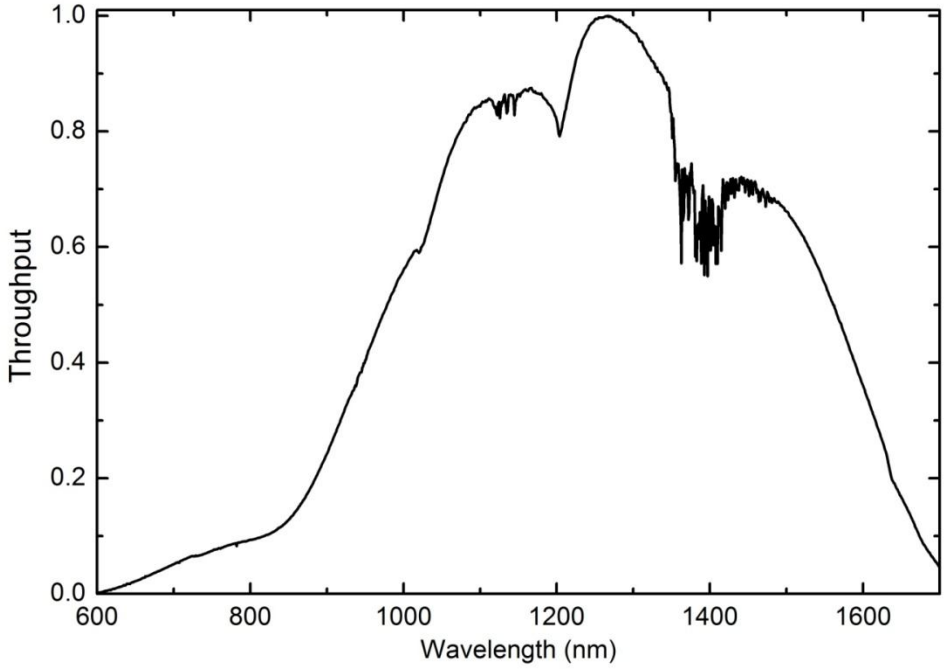

Figure 2.12. Normalized throughput for the PL system with Ge detector from 600 nm to 1700 nm.

Chapter 3

GROWTH AND MATERIAL PROPERTIES OF ZnTe ON GaAs, InP, InAs, AND GaSb (001) SUBSTRATES

3.1 ZnTe virtual substrates

ZnTe is a direct-band semiconductor with a bandgap of 2.26 eV (549 nm), which is considered to be suitable for various optoelectronic devices such as pure-green light-emitting diodes, green laser diodes, UV-green photodetectors, and multijunction solar cells [26,36]. Although pure-green ZnTe LEDs have been successfully demonstrated on ZnTe substrates [59,60], one of the big obstacles to making them commercially applicable is the high cost and small size of current ZnTe bulk substrates. It is therefore highly desirable to have larger wafer size ZnTe virtual substrates. Since ZnTe has a lattice constant of 6.1037 Å which is nearly lattice-matched to 6.1 Å III-V substrates, such as GaSb, with a mismatch of only 0.13%, and InAs with a mismatch of 0.75%, ZnTe grown on these substrates is expected to have a low density of misfit dislocations. Moreover, GaAs and InP are good substrate candidates for electronic devices and infrared (IR) photodetectors due to their semi-insulating properties and transparency in the IR range [61]. Thus, the ability to achieve high quality ZnTe epitaxial growth on these different substrates, and the possibility to reduce the overall material cost, are very important considerations not only for ZnTe related devices, but also for electronic and optoelectronic device applications based on these 6.1 Å compound semiconductors that can be grown lattice matched to ZnTe virtual substrates.

In this chapter, thick ZnTe epilayers grown on III-V substrates as low-cost virtual substrates are comprehensively studied and discussed. A set of ZnTe samples are grown on GaAs, InP, InAs and GaSb (001) substrates using molecular beam epitaxy (MBE), and the material properties of the ZnTe films are investigated. During MBE growth, *in situ* reflection high energy electron diffraction (RHEED) is used for growth monitoring and optimization. High-resolution X-ray diffraction (XRD) measurements are performed to analyze the strain of the ZnTe epilayers and high-resolution transmission electron microscopy (TEM) is used to study the structural properties of the ZnTe epilayers, especially misfit dislocations at the interface. Photoluminescence (PL) and spectroscopic ellipsometry (SE) are also applied to characterize the optical properties of the ZnTe epilayers. Growths of high-quality ZnTe samples are successfully demonstrated on all four substrates. Some of the results reported in this chapter have been published [62].

3.2 MBE Growth of ZnTe virtual substrates

All the samples studied in this chapter are grown by MBE, which is one of the most commonly used growth techniques for high quality compound semiconductors. Since the ZnTe samples are grown on III-V substrates which involve both II-VI and III-V materials, the growth is carried out using a unique MBE system consisting of II-VI and III-V chambers. The II-VI chamber is equipped with Cd, Zn, Mg, Se, and Te effusion cells, an Al effusion and a N plasma doping source cells, while the III-V chamber is equipped with Ga, In, and

Al effusions cells, and Sb and As valved cracker cells. The source materials are installed in individual cells, which provide atomic or molecular beams under thermal evaporation. A schematic diagram of the whole MBE system is shown in Figure 3.1, provided by courtesy of Dr. Ding Ding.

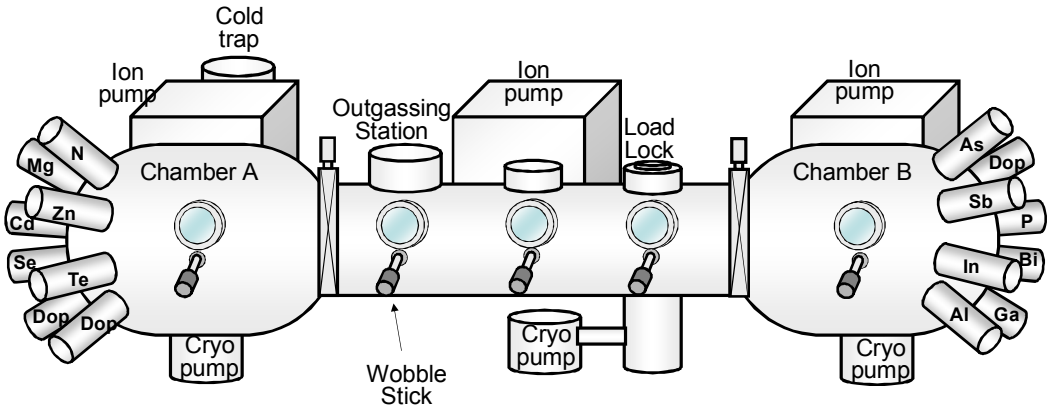

Figure 3.1. Dual-chamber MBE system (provided by courtesy of Dr. Ding Ding).

The growth is carried out by Dr. Xinyu Liu in Prof. Jacek Furdyna's group at University of Notre Dame. During growth, substrate is held on a wafer holder which is heated to the desired temperature and continuously rotated to improve the uniformity of epilayer. The substrate temperature is measured with a thermocouple on the back of the substrate holder, which is also calibrated by a pyrometer facing the holder surface. Shutters are used to adjust the flux of the evaporated source materials. The dual chambers are connected using an ultrahigh-vacuum transfer module, in which the vacuum is typically maintained at about 5×10^{-9} Torr to prevent any significant contamination during sample transfer.

For growth of the samples, the substrates were firstly deoxidized in the III-V chamber, followed by the growth of III-V semiconductor buffer layers. The growth orientation for all samples was (001). After the samples were cooled down

to room temperature, they were transferred to the II-VI chamber where the ZnTe layers were grown. The growth of ZnTe was initialized under a Zn flux for several seconds prior to opening the Te shutter so that the formation of Ga_2Te_3 phase can be minimized. The substrate temperature during ZnTe growth was 330˚C.

During growth, the beam equivalent pressure (BEP) ratios of Zn to Te were adjusted to optimize the growth conditions by monitoring the surface reconstructions using RHEED. RHEED is a commonly used tool to monitor MBE growth, which utilizes a high energy electron beam incident at a small angle (<5°) to the surface of sample during growth. For RHEED measurements, only atoms at the top surface (a few atomic layers) contribute to the RHEED pattern, which provides the information of surface morphology and surface reconstruction. For the ZnTe samples in this study, the RHEED patterns appeared to be similar regardless of the specific III-V substrate used for the growths. As an example, RHEED patterns for ZnTe grown on InAs (001) substrate are shown in Figure 3.2. Patterns in upper and lower rows are referred to [110] and $[1\bar{1}0]$ axes, respectively.

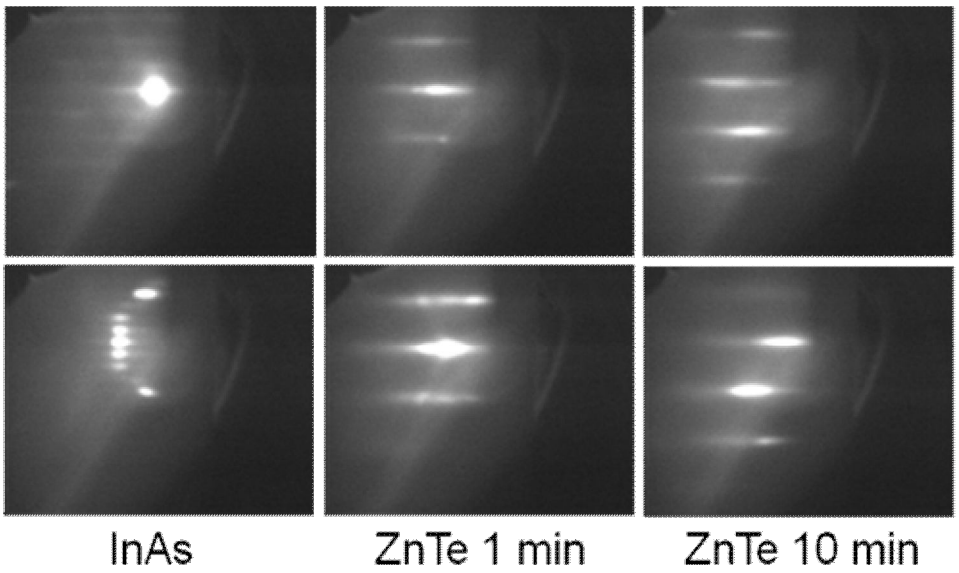

Figure 3.2. RHEED patterns for the growth of ZnTe/InAs (001) sample [62].

It can be seen that a (2×4) reconstruction of the InAs surface is visible before growth of the ZnTe layer was commenced. At the beginning of ZnTe growth, the RHEED pattern showed a spotty and weakly defined pattern, indicating a transition from the (2×4) to the (2×1) surface reconstruction. The transition time was in the range of 10 s to 1 min. After the transition of the surface reconstruction, the typical ZnTe (2×1) pattern appeared and stayed bright and streaky throughout the rest of the ZnTe growth. The growth parameters for the samples described in this chapter are summarized in Table 3.1.

Table 3.1. Growth parameters for ZnTe samples [62].

Sample No.	**Substrate**	**Zn:Te BEP ratio**	**Growth rate (nm/s)**	**Lattice mismatch**	**ZnTe layer thickness (µm)**
1	GaAs	1.2:1	0.30	7.30%	2.5
2	InP	1.2:1	0.28	3.85%	2.3
3	InAs	1.2:1	0.30	0.75%	2.4
4	GaSb	1.2:1	0.31	0.13%	2.5

3.3 Characterization results and discussion

3.3.1 XRD measurements and results

After completion of growth, high-resolution XRD measurements are performed using a PANalytical X'Pert PRO MRD X-ray diffractometer with multi-crystal monochromator. The copper $K_{\alpha 1}$ line (1.54 Å) is used as the incident beam. For all the samples in this study, XRD measurements are carried out in the vicinity of the (004) and (113) diffraction peaks of the substrates. Figure 3.3 - Figure 3.6 show the XRD patterns of ZnTe epilayers grown on the various substrates. The measured XRD patterns show two clear diffraction peaks coming from both the ZnTe epilayer and the particular substrate material. The full-width at half-maximum (FWHM) of the ZnTe epilayers are in the range of 33 - 60 arcsec, indicating that the thick ZnTe layers grown on all four substrates are of high quality.

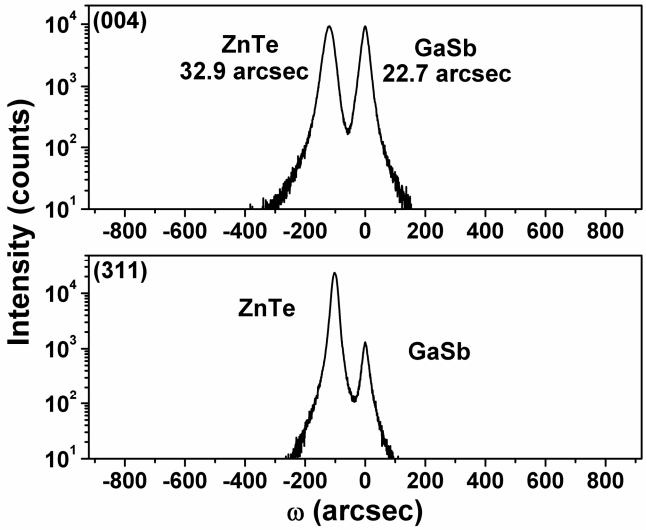

Figure 3.3. XRD pattern measured in the vicinity of the (004) and (311) diffraction peaks for ZnTe/GaSb (001) sample. The FWHMs of ZnTe and GaSb (004) diffraction peaks are 32.9 and 22.7 arcsec, respectively [62].

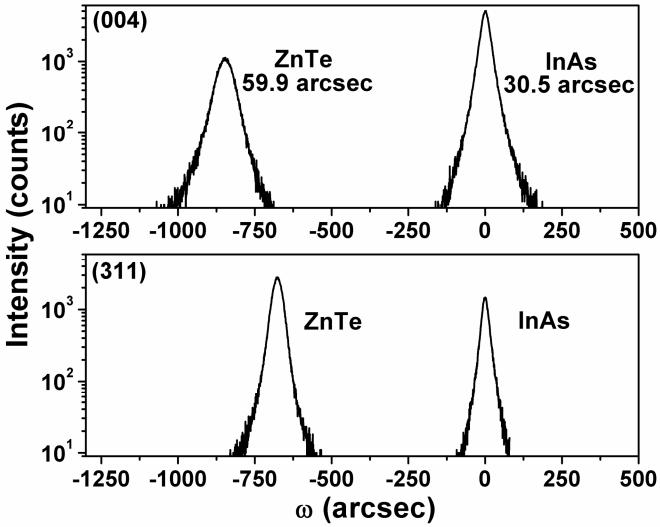

Figure 3.4. XRD pattern measured in the vicinity of the (004) and (311) diffraction peaks for ZnTe/InAs (001) sample. The FWHMs of ZnTe and InAs (004) diffraction peaks are 59.9 and 30.5 arcsec, respectively [62].

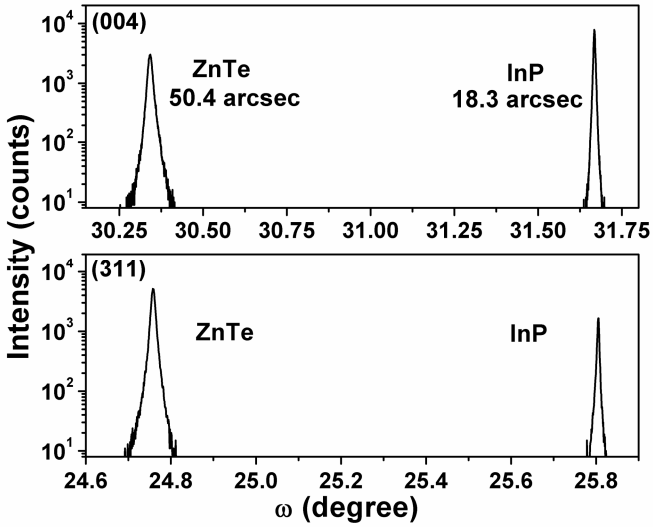

Figure 3.5. XRD pattern measured in the vicinity of the (004) and (311) diffraction peaks for ZnTe/InP (001) sample. The FWHMs of ZnTe and InP (004) diffraction peaks are 50.4 and 18.3 arcsec, respectively [62].

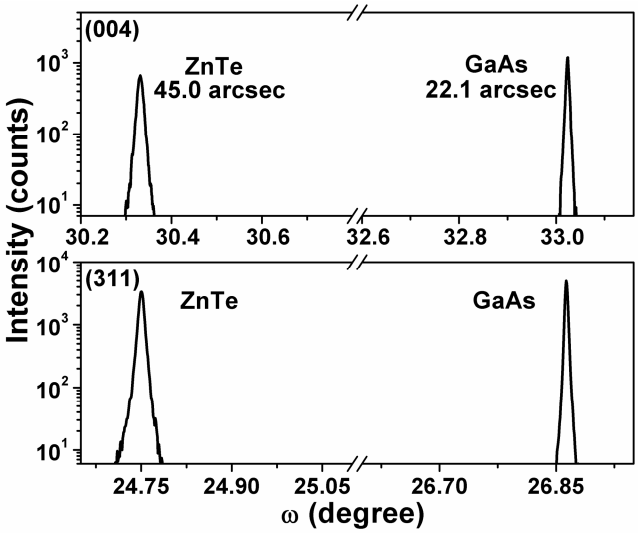

Figure 3.6. XRD pattern measured in the vicinity of the (004) and (311) diffraction peaks for ZnTe/GaAs (001) sample. The FWHMs of ZnTe and GaAs (004) diffraction peaks are 45.0 and 22.1 arcsec, respectively [62].

Due to the different lattice constants between ZnTe and the various III-V substrates, strain occurs in the ZnTe epilayers during growth, making the lattice constants of the ZnTe epilayers different from that of bulk ZnTe. The room temperature lattice constants of the ZnTe epilayers along the growth direction ($a_{\perp}$) and in the layer plane ($a_{\parallel}$) can be determined from the XRD results obtained on the (004) and (113) reflections. The lattice constant $a_{\perp}$ is directly calculated by applying Bragg's law on (004) XRD pattern, shown as Equations (3.1) and (3.2):

$$2d^{l}_{004}\sin\theta^{l}_{004} = \lambda, \tag{3.1}$$

$$2d^{s}_{004}\sin\theta^{s}_{004} = \lambda, \tag{3.2}$$

where d^{l}_{004} and d^{s}_{004} are the interplanar spacings of (004) lattice plane for epilayer layer and substrate, respectively; θ^{l}_{004} and θ^{s}_{004} are the diffraction angles of (004) lattice plane for epilayer layer and substrate, respectively. Since the vertical lattice

constant is four times interplanar spacing of (004) plane, the vertical lattice constant ($a_\perp$) can be expressed by Equation (3.3):

$$a_\perp = (\sin\theta_{004}^{s} / \sin\theta_{004}^{l}) \cdot a_s \,, \tag{3.3}$$

where a_s is the lattice constant of the substrate material.

To determine lattice constant $a_{\parallel}$, XRD measurements of both symmetric and asymmetric reflections are necessary. In the following analysis, calculation is given for materials with a cubic/Zincblende structure, which can be applied to many semiconductors. As known, the lattice parameter of an epilayer can be affected by several factors such as lattice mismatch, misfit dislocation, tetragonal distortion, etc., so that the real lattice structure might not be a perfect cubic anymore. For a general situation, the lattice constants along (100), (010), and (001) directions can be different and defined as *a*, *b*, and *c*, respectively. For any given lattice plane with Miller indices (*h k l*), the lattice plane (*h k l*) can be expressed by Equation (3.4):

$$\frac{x}{a/h} + \frac{y}{b/k} + \frac{z}{c/l} = 1, \tag{3.4}$$

where x, y, and z correspond to the coordinates of any point on the (*h k l*) lattice plane. x, y, and z axes are along (100), (010), and (001) direction, respectively. From Equation (3.4), it is known that the normal to (*h k l*) lattice plane is along the direction (*h/a k/b l/c*). Now define d_{hkl} as the interplanar spacing for (*h k l*) plane, which is also equal to the distance between origin (000) and (*h k l*) plane. Based on Equation (3.4), d_{hkl} can be expressed by Equation (3.5):

$$d_{hkl} = \frac{1}{\sqrt{(h/a)^2 + (k/b)^2 + (l/c)^2}}. \quad (3.5)$$

By further simplifying Equation (3.5), we have Equation (3.6) and (3.7):

$$(\frac{1}{d_{hkl}})^2 = (\frac{h}{a})^2 + (\frac{k}{b})^2 + (\frac{l}{c})^2, \quad (3.6)$$

$$(\frac{2\sin\theta_{hkl}}{\lambda})^2 = (\frac{h}{a})^2 + (\frac{k}{b})^2 + (\frac{l}{c})^2. \quad (3.7)$$

Since the epilayer is subjected to biaxial strain, the lattice constants a and b are equal to each other, representing the in-plane lattice constant ($a_{\parallel}$). Therefore, the finalized equation to calculate the lattice constant $a_{\parallel}$ is given by Equation (3.8):

$$(\frac{2\sin\theta^{l}_{hkl}}{\lambda})^2 = (\frac{h}{a_{//}})^2 + (\frac{k}{a_{//}})^2 + (\frac{l}{a_{\perp}})^2. \quad (3.8)$$

Based on Equations (3.3) and (3.8), the lattice constants ($a_{\perp}$ and $a_{\parallel}$) for ZnTe epilayers grown on various substrates are determined and summarized in Table 3.2.

Table 3.2 Lattice parameters of ZnTe epilayers grown on different substrates [62].

Sample No.	$a_{\perp}$ **(Å)**	$a_{\parallel}$ **(Å)**
1 (ZnTe/GaAs)	6.1014	6.1046
2 (ZnTe/InP)	6.0995	6.1052
3 (ZnTe/InAs)	6.1016	6.1045
4 (ZnTe/GaSb)	6.1014	6.1042

Compared with the reported lattice constant of bulk ZnTe at room temperature (6.1037 Å) [63], the vertical lattice parameters ($a_{\perp}$) of all ZnTe epilayers are smaller, which indicates residual tensile strain (parallel to the surface). The major

factors related to this residual tensile strain are the lattice constants, thermal expansion coefficients, and growth temperatures. The lattice constants and thermal expansion coefficients for bulk GaAs, InP, InAs, GaSb and ZnTe are listed in Table 3.3 [62].

Table 3.3 Lattice constants and thermal expansion coefficients of GaAs, InP, InAs, GaSb and ZnTe bulk materials [62].

Bulk material	**Lattice constant (Å)**	**Thermal expansion coefficient (1×10^{-6} K^{-1})**
GaAs	5.654	5.75
InP	5.869	4.56
InAs	6.059	5.00
GaSb	6.096	6.35
ZnTe	6.104	8.33

As shown in Table 3.2, ZnTe has a larger bulk lattice constant than all of the substrate materials (GaAs, InP, InAs and GaSb) used in this study. Therefore, compressive strain due to this lattice mismatch is induced during the initial ZnTe growth at the growth temperature. Such compressive strain can be easily measured when the ZnTe layer is thin (~ 110 nm), as reported in the previous study [36]. However, when the ZnTe layers are grown beyond a certain critical thickness, the strain due to the lattice mismatch between ZnTe and the specific substrate becomes fully relaxed at the growth temperature. For example, it has been reported that the critical thickness for ZnTe grown on GaAs (001) substrate by MBE is about 15 nm, compared with 180 nm for ZnTe grown on GaSb substrate using organometallic vapor phase epitaxy (OMVPE) [64,65]. Therefore, for ZnTe thicknesses in the range of 2.3 - 2.5 μm, it is reasonable to assume that

the compressive strain due to lattice mismatch is fully relaxed in the ZnTe epilayers at the growth temperature. Moreover, ZnTe has a larger thermal expansion coefficient (8.33×10^{-6} K^{-1}) than that of all of the substrate materials. Thus, when the samples are cooled down to room temperature after the growth, the thermal shrinkage of the ZnTe epilayers is greater than that of the substrates. Accordingly, tensile strain occurs in the ZnTe epilayer.

3.3.2 TEM measurements and results

Transmission electron microscope (TEM) is one of the most widely used instruments for studying microstructure. A schematic diagram of TEM is shown in Figure 3.7. Electrons from an electron gun are accelerated under a high voltage, typically from 100 to 400 kV, and focused by condenser lenses onto the specimen. The specimen thickness must be very thin (≤ 50 nm) so that the electrons can be transmitted through the specimen.

One of the biggest advantages of TEM is the extremely high resolution, which can approach sub-atomic scale. For an optical microscope, the resolution as limited by diffraction can be estimated by Equation (3.9):

$$d = 0.61\lambda / NA, \tag{3.9}$$

where d is the resolution, λ is the wavelength, and NA is numerical aperture. For example, the resolution of an optical microscope, which typically has a numerical aperture around 1 (NA ~ 1) working in the visible range (λ ~ 500 nm), is determined to be about 300 nm using Equation (3.9). However, for the TEM, unavoidable spherical aberration restricts the maximum usable aperture angle.

Thus, despite the picometer-scale wavelengths for 100 - 400 keV electrons, a compromise must be made between diffraction and spherical aberration. The resolution limit is then given by Equation (3.10):

$$d = A \cdot C_s^{1/4} \cdot \lambda^{1/4}, \tag{3.10}$$

where C_s is the spherical aberration coefficient of the objective lens, λ is the electron wavelength, and A is a constant close to unity depending on the coherent or incoherent image formation process. Resolution limits improve slightly at higher electron energy (shorter wavelength) and range from ~ 0.35 - 0.10 nm for 100 - 1250 keV imaging.

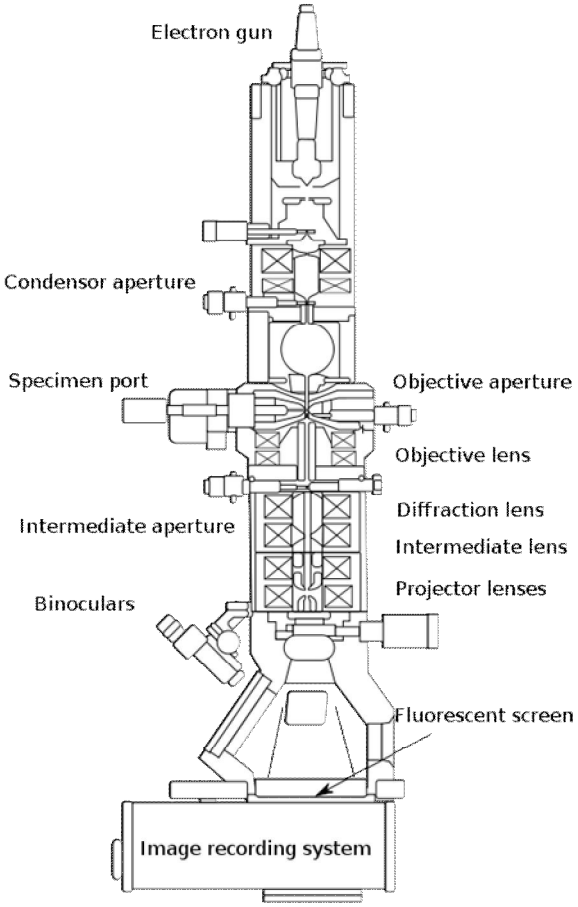

Figure 3.7 Layout of optical components in a TEM [66].

In this study, sample preparation and image recording are carried out by Dr. Lu Ouyang and Prof. David Smith at Arizona State University. The cross-sectional TEM specimens are prepared using mechanical polishing and dimpling followed by ion-beam thinning. Liquid nitrogen and low energy (2.5 - 3 keV) ion beams are used to avoid any thermal damage. Images are recorded using a JEM-4000EX HREM operated at 400 keV with a structural resolution of ~ 1.7 Å. The misfit dislocations present at the various ZnTe/substrate interfaces are studied using both low magnification and high magnification TEM images [67]. As visible in Figure 3.8, low magnification image of the ZnTe/GaAs sample shows a high density of misfit dislocations near the interface, which is attributed to the large lattice mismatch of 7.3% between ZnTe and GaAs. It is also apparent that the dislocation density becomes much less as the ZnTe thickness increases. The high magnification image in Figure 3.9 shows that there are pseudo-periodic dislocations present at the ZnTe/GaAs interface.

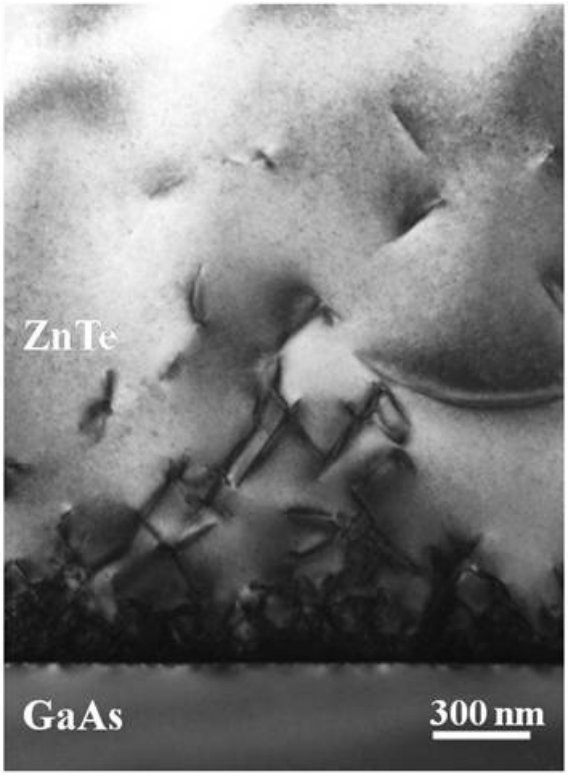

Figure 3.8. Low magnification TEM image of ZnTe/GaAs (001) sample [62].

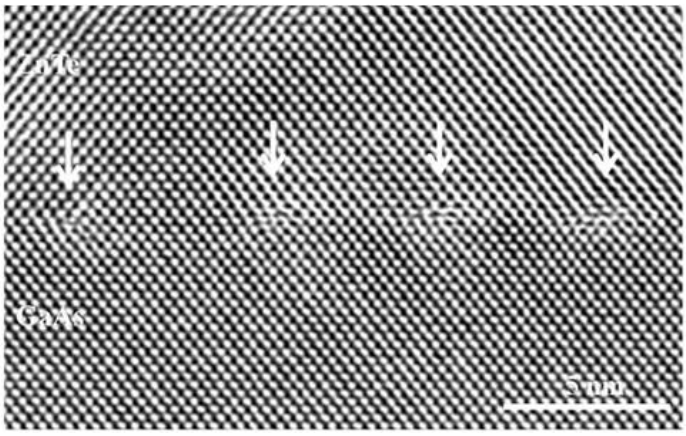
Figure 3.9. High magnification TEM image of ZnTe/GaAs (001) sample with arrows pointing to dislocations [62].

Burgers' circuits drawn directly on high magnification image indicate that ~ 39% of these dislocations are Lomer edge dislocations, with the remainder being 60° partial dislocations. As shown in Figure 3.10, the Burgers vector of the

Lomer dislocation labeled with an arrow corresponds to one-half lattice spacing along the [110] direction, i.e. $a_0/2$ [110].

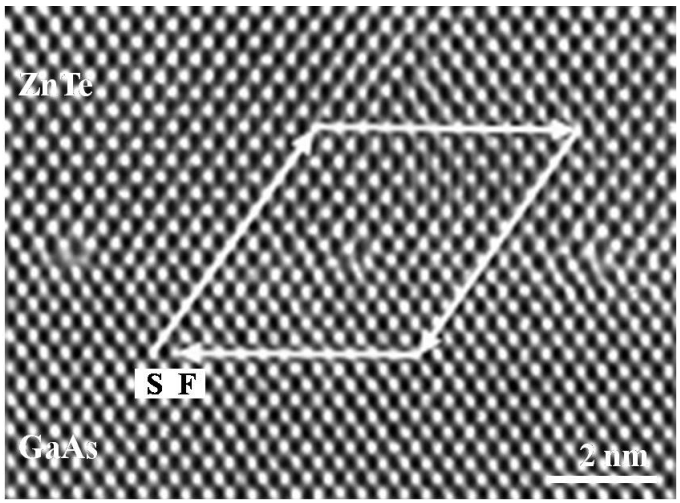

Figure 3.10. High-resolution image showing ZnTe/GaAs interface with Burgers' circuit. S and F indicate the start and finish points for the Burgers' circuit analysis [62].

3.3.3 PL measurements and results

For characterization of optical properties, PL measurements are carried out using the 488 nm line of an Argon ion laser for excitation and a high-resolution grating spectrometer equipped with a photomultiplier for detection. The PL spectra of all the ZnTe samples measured at 300 K are shown in Figure 3.11. Regardless of the substrates, all the PL peaks are at 2.26 eV. The PL emission from ZnTe epilayer grown on GaSb has the strongest intensity, which is attributed to the minimal defect density in the epilayer due to the smallest lattice mismatch of 0.13% between ZnTe and GaSb. Similarly, the sample of ZnTe grown on InAs with a lattice mismatch of 0.75% shows much stronger PL intensity than that of the other two ZnTe samples grown on InP and GaAs substrates, which have larger lattice mismatches of 3.85% and 7.30%, respectively.

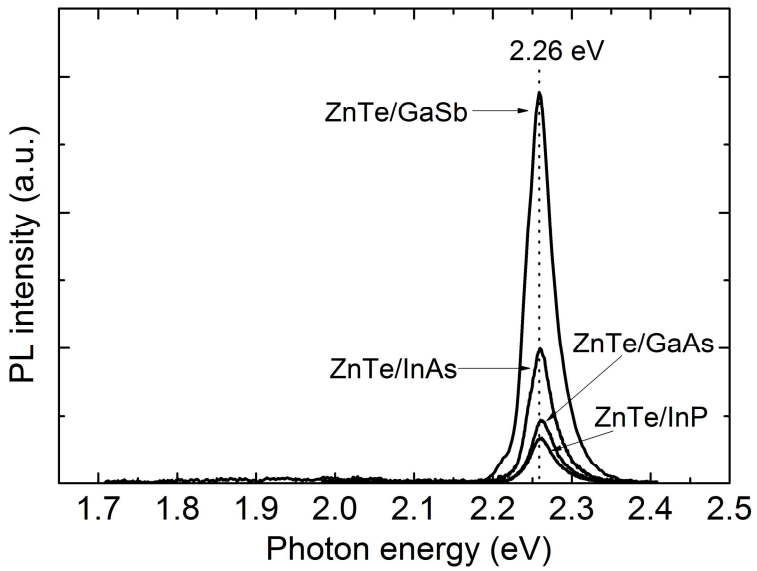

Figure 3.11. PL spectra of all the ZnTe samples measured at 300 K showing all the PL peaks positioned at 2.26 eV [62].

Temperature-dependent PL spectra of ZnTe grown on GaAs are shown in Figure 3.12. As temperature increases, the PL peak shows a red-shift due to decrease in the bandgap energy, and the FWHM of the PL spectrum becomes broader as expected. In addition, a broad PL emission below bandgap energy is observed at 80 K. This emission is attributed to defect-related optical transitions.

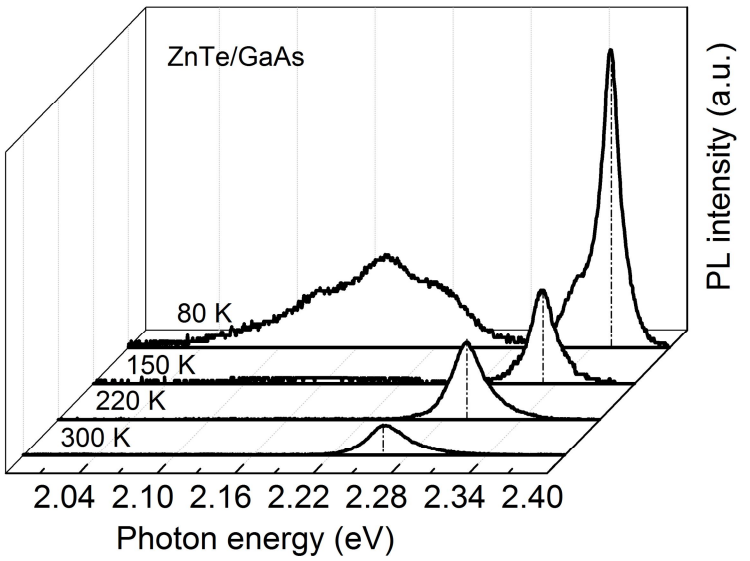

Figure 3.12. Temperature-dependent PL spectra of ZnTe/GaAs sample measured from 80 to 300 K [62].

3.3.4 SE measurements and results

Ellipsometry is a contactless, non-invasive technique that characterizes the optical response of materials. In ellipsometry measurement, p- and s-polarized light waves are irradiated onto a sample at the Brewster angle. Since materials response differently to p- and s-polarized light, the changes in p- and s-polarizations before/after light reflection on a sample are different in amplitude and phase. Experimentally, ellipsometry measures two values (ψ, Δ) which express the amplitude ratio (ψ) and phase difference (Δ) between p- and s-polarized light waves. Figure 3.13 shows the configuration of an ellipsometry measurement system.

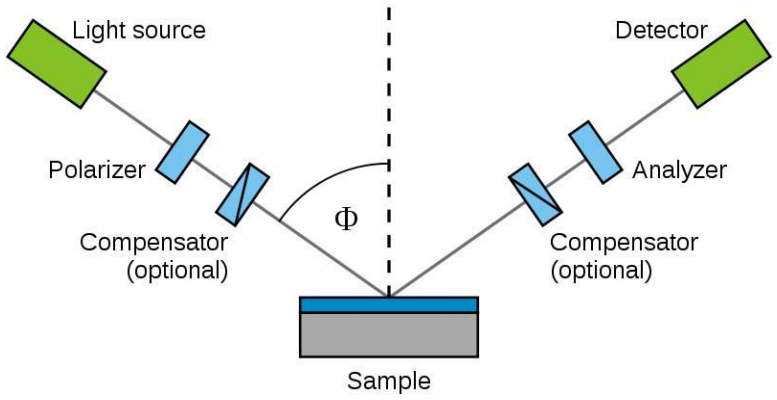

Figure 3.13. Schematic diagram of ellipsometry measurement.

Spectroscopic ellipsometry (SE) measurements can be regarded as an extended ellipsometry by using more than one single wavelength. Furthermore, the incident angle can be varied, providing another degree of freedom. In particular, when a sample structure is simple, the amplitude ratio ψ can be characterized by the refractive index *n* while Δ represents light absorption described by the extinction coefficient *k*.

In this study, the dielectric functions of the ZnTe epilayer grown on the GaAs, InP, InAs and GaSb (001) substrate are studied using an infrared variable-angle spectroscopic ellipsometer (IR-VASE). The ellipsometric angles ψ and Δ are measured at room temperature from 0.04 eV to 0.65 eV with an incident angle of 65º. The ZnTe sample is then modeled as a three-layer system consisting of a substrate, a film layer representing the ZnTe epilayer, and a surface layer. The complex dielectric function of the substrate is then obtained separately and used in tabulated form. The surface layer is modeled as a thin film with 50% ZnO and 50% voids using the Bruggeman approximation [68]. The complex dielectric

function of the ZnTe epilayer is described using an optical dispersion model given by Equation (3.11):

$$\varepsilon(E) = C + \sum_{i=1}^{2} \frac{A_n}{E_n^2 - E^2}, \tag{3.11}$$

where C is a constant that is taken as an adjustable parameter. The remaining term describes the dispersion caused by absorption due to various processes such as phonon vibrational modes, free carrier absorption and interband transitions outside the spectral range. A_n is the magnitude of the pole and E_n represents the pole energy. The pole energies are kept fixed at E_1= 0.022 eV and E_2= 2 eV respectively. The fit parameters, including the thicknesses of the film and surface layer, are then optimized using a proprietary Marquardt–Levenberg algorithm provided by the ellipsometer manufacturer. Figure 3.14 shows the experimental (ψ, Δ) spectra with the modeling results for ZnTe/InP sample. The measurements are carried out at two angles 60˚ and 65˚.

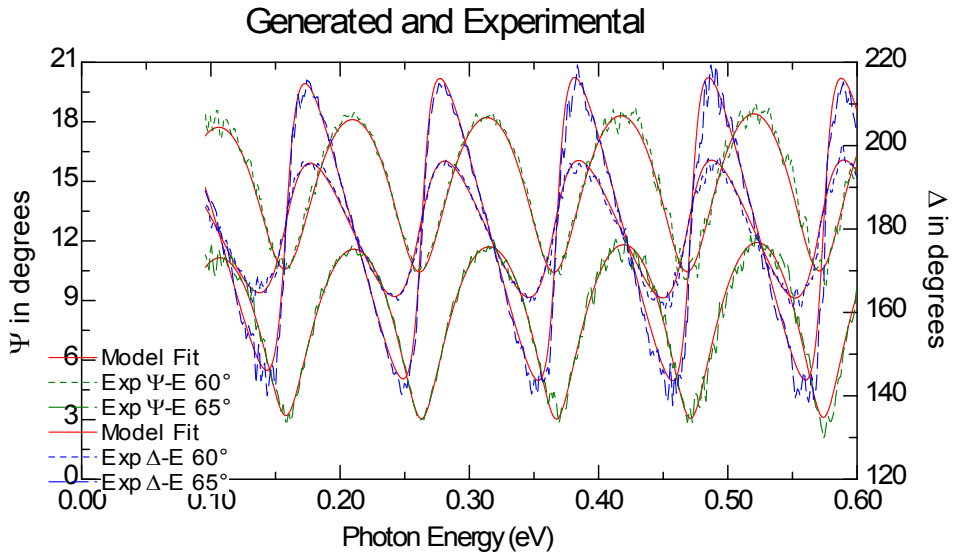

Figure 3.14. Experimental SE data and modeling results for the ZnTe/InP sample.

Clearly, it can be seen that the model fits the raw experimental data quite well. Based on the model, dielectric functions are determined and plotted. Figure 3.15 summarizes the real part of dielectric functions of all the ZnTe epilayers. One thing has to be noted that the optical response of ZnTe layers is described by Equation (3.11) which only contains the real part of the dielectric function. It indicates that the absorption of ZnTe epilayers in the measured IR range (2 - 30 μm) is below the detection limit of SE measurement.

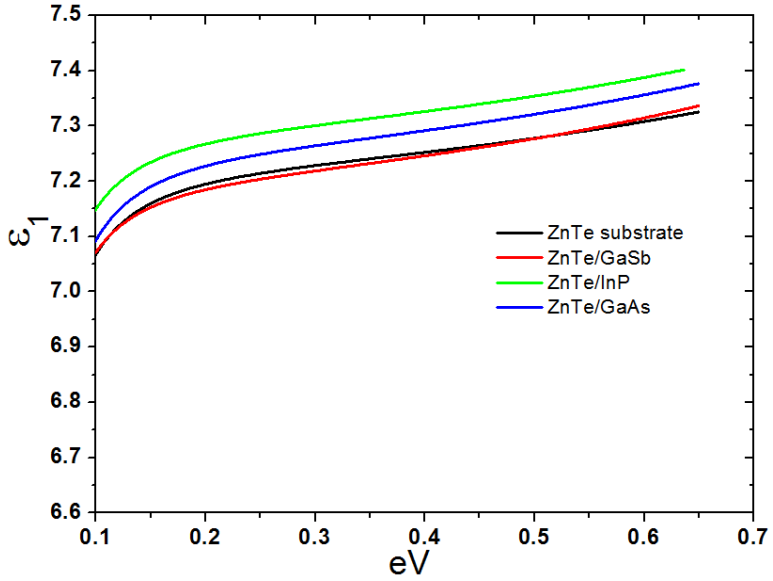

Figure 3.15. The real part of dielectric function (ε_1) for the ZnTe epilayers grown on GaSb, InP, GaAs substrates, and ZnTe bare substrate in the IR range from 2 μm to 30 μm.

3.4 Summary

The use of thick epitaxial grown ZnTe as a low-cost virtual substrate is proposed for various device applications and high-quality thick ZnTe layers are successfully grown on various GaAs, InP, InAs, and GaSb (001) substrates using MBE. High-resolution XRD results show narrow FWHM (33 - 60 arcsec) for the ZnTe epilayers grown on all four different substrates. The lattice parameters for

ZnTe epilayers along the growth direction ($a_{\perp}$) and in the layer plane ($a_{\parallel}$) are measured and show that tensile strains are present in the ZnTe layers due to the difference in thermal expansion coefficients between the epilayers and the substrates. High-resolution TEM images reveal that Lomer edge dislocations and 60° partial dislocations are the predominant defects present at the ZnTe/GaAs and ZnTe/InP interfaces. The defect densities in all films become lower as the ZnTe thickness is increased. Strong PL spectra for all the ZnTe samples are observed from 80 K to 300 K. The PL peak positions of ZnTe epilayers are at 2.26 eV at room temperature. Spectroscopic ellipsometry is used to measure the optical response of the ZnTe film grown on various substrates, and the dielectric functions are determined over the range from 0.04 eV to 0.65 eV.

Chapter 4

GROWTH AND MATERIAL PROPERTIES OF GaSb GROWN ON ZnTe

4.1 Motivation for GaSb grown on ZnTe

As discussed in chapter 3, thick ZnTe grown on low-cost III-V substrates is proposed as virtual substrate for 6.1-Å material platform, and growth of high quality ZnTe samples has been successfully demonstrated. Based on the ZnTe virtual substrate work, it is further noticed that 1) realization of the growth of high-quality GaSb on ZnTe virtual substrates could enable monolithic integration of InAs- and GaSb-based semiconductor devices, such as mid-wavelength infrared (IR) laser diodes and long-wavelength IR photodetectors composed of InAs/InAsSb and InAs/(In)GaSb type-II superlattices [20], on large low-cost GaAs or Si substrates; 2) ZnTe can work as a good insulating material, on which GaSb-based electronic devices with high mobility for both electrons and holes (1.204×10^4 and 1.624×10^3 [$cm^2/(V\cdot s)$], respectively) can be built, making GaSb/ZnTe heterostructure suitable for high electron mobility transistor (HEMTs), also known as heterostructure field effect transistor (HFET), and high speed complimentary MOS devices; 3) ZnTe and GaSb have type-I band edge alignment and large difference in refractive index providing optical and electrical confinement for both carriers. Such properties can be used and suitable for making light emitting diodes (LEDs), laser diodes (LDs), and distributed Bragg reflectors (DBRs), which will be discussed in chapter 5 and chapter 6; 4) more importantly, to demonstrate high quality growth of GaSb on ZnTe can achieve

full integration of 6.1 Å II-VI/III-V semiconductors and enable the use of 6.1 Å II-VI/III-V materials with more degrees of freedom to realize more novel device structures. Although some preliminary studies of the growth of GaSb on ZnTe have been reported [69,70], realization of high-quality crystalline materials of GaSb on ZnTe still remains challenging.

In this chapter, growth and material properties of GaSb on ZnTe using molecular beam epitaxy (MBE) is studied and discussed. A temperature ramp during the growth of GaSb on ZnTe has been used in an effort to achieve better material quality. To investigate the influence of the growth temperature ramp on the structural and optical properties of GaSb on ZnTe, a set of samples are grown on ZnTe/GaSb (001) substrates under different growth conditions. During MBE growth, *in situ* reflection high energy electron diffraction (RHEED) is used for growth monitoring and optimization. High-resolution X-ray diffraction (XRD) measurements are performed to determine the structural quality of the GaSb epilayers, and transmission electron microscopy (TEM) is used to study the surface morphology of the GaSb epilayers and misfit dislocations at GaSb/ZnTe interfaces. Photoluminescence (PL) is also applied to characterize the optical properties of GaSb epilayers. Some of the results reported in this chapter have been published [71].

4.2 MBE Growth of GaSb on ZnTe

Epitaxial growth of GaSb has been well studied and developed using different growth techniques, including liquid phase epitaxy (LPE), vapor phase

epitaxy (VPE), MBE, etc. For LPE, the growth of GaSb in Ga- and Sb-rich conditions has been reported in the temperature range of 330 – 680 ˚C [72-75]. To reach high material quality, Sb-rich conditions are considered important to reduce native acceptor concentration. The native defect concentration is reported to be reduced to a level of 2×10^{-15} cm^{-3} [76]. On the other hand, it is also found that the native defect concentration can be reduced by growth under Ga-rich conditions at low temperatures (below 400 ˚C) [77]. However, it is difficult to achieve a smooth morphology and hence this approach is not suitable for device applications [78]. Compared with LPE, the main difficulty for the growth of GaSb using MBE is the low vapor pressure of Sb. As a result, Sb will have a low surface mobility and tend to form clusters or precipitates during MBE growth. Thus, the antisite defects Ga_{Sb} are generated. To solve this problem, the growth is carried out under Sb-rich conditions and the native defect concentration has been obtained as low as 8×10^{-15} cm^{-3} [79]. Therefore, Sb-rich conditions are preferred for high material quality.

As opposed to the homoepitaxial growth of GaSb mentioned above, GaSb is proposed to be grown on top of ZnTe in this study. The epitaxial growth is carried out using a dual-chamber MBE system by Dr. Xinyu Liu at University of Notre Dame. Before GaSb was deposited on ZnTe, thin ZnTe epilayers were first grown on GaSb (001) substrates, as described previously in chapter 3. After growth of ZnTe in the II-VI chamber, the wafers were transferred to the III-V chamber for the GaSb growth. Since the commonly used temperature for growth

of GaSb (T_g = 470 ˚C) is considerably higher than that used for ZnTe (T_g = 320 ˚C), the surface of ZnTe layer is likely to be severely degraded if the growth of GaSb on ZnTe is initiated at such high temperature.

To find solution to this problem, GaSb epilayers are grown under different conditions. The sample structures can be simply categorized into two groups A and B by growth temperature conditions, as shown in Figure 4.1. For group A, GaSb epilayer is grown under low temperature (T_g = 380 ˚C). For group B, GaSb epilayer is firstly grown under a temperature ramp before the remaining GaSb epilayer is deposited at the normal growth temperature.

Layer material	Temperature (˚C)
GaSb	380
ZnTe	320
GaSb	470
GaSb (001)	Substrate

Layer material	Temperature (˚C)
GaSb	470
GaSb	T ramp
ZnTe	320
GaSb	470
GaSb (001)	Substrate

Figure 4.1. GaSb sample structures grown under two different growth temperatures conditions, group A (left) and group B (right).

To further investigate the influence of different temperature ramps on the material quality, three temperature ramps which consist of different ramping ranges and ramping rates are applied on separate samples for comparison. The growth parameters used in this study are summarized in Table 4.1 [71].

Table 4.1. Growth parameters for GaSb samples [71].

Growth condition	Growth temperature (˚C)	Temperature ramp (˚C)	Ramping rate (˚C/min)	Ga/Sb BEP ratio	Growth rate (μm/hr)
#1	380	NA	NA	1:5	0.8
#2	470	380 – 470	27	1:5	0.8
#3	470	360 – 470	33	1:5	0.8
#4	470	320 – 470	45	1:5	0.8

During growth, the beam equivalent pressure (BEP) ratios of Ga to Sb were adjusted by monitoring the surface reconstructions observed using RHEED. As an example, RHEED patterns for a sample grown under growth condition #3 are shown in Figure 4.2. The RHEED patterns showed the typical (2×1) reconstruction for the ZnTe surface before growth of the GaSb transition layer. At the initial stages of GaSb growth, the RHEED measurements showed spotty and unclear patterns. The typical (1×3) GaSb surface reconstruction started to appear after ~ 10 sec. A bright and streaky RHEED pattern with clear (1×3) surface reconstruction became clearly visible after ~ 60 sec, indicating a smooth transition from the ZnTe surface reconstruction to the GaSb surface reconstruction.

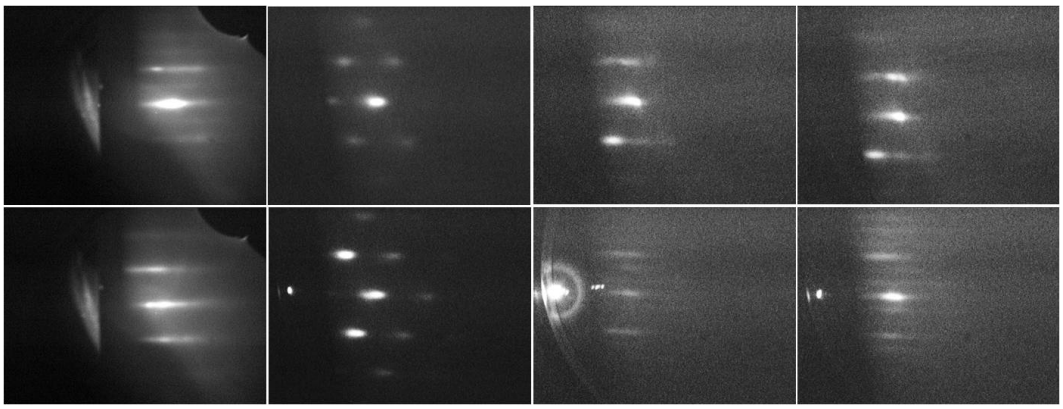

Figure 4.2. RHEED patterns for growth of GaSb on top of ZnTe. Patterns in upper and lower rows are referred to [110] and [$1\bar{1}0$] axes, respectively [71].

4.3 Characterization results and discussion

4.3.1 XRD measurements and results

After completion of growth, high-resolution XRD measurements are performed on all samples in the vicinity of the (004) diffraction peak of the GaSb substrate. In the following discussions, the XRD results of GaSb samples in group A and group B are summarized and analyzed.

4.3.1.1 Low-temperature grown GaSb epilayers at 380 ˚C

Three samples (#91118A, #91118B and #91222D) containing GaSb epilayers grown under 380 ˚C are studied in this section. Figure 4.3 shows the detailed sample structures with nominal thickness of each layer.

GaSb (490 nm)	GaSb (490 nm)	GaSb (490 nm)
ZnTe (40 nm)	ZnTe (133 nm)	ZnTe (500 nm)
GaSb (100 nm)	GaSb (100 nm)	GaSb (100 nm)
GaSb Substrate (001)	GaSb Substrate (001)	GaSb Substrate (001)

Figure 4.3. Structures of sample #91118A, #91118B, and #91222D from left to right.

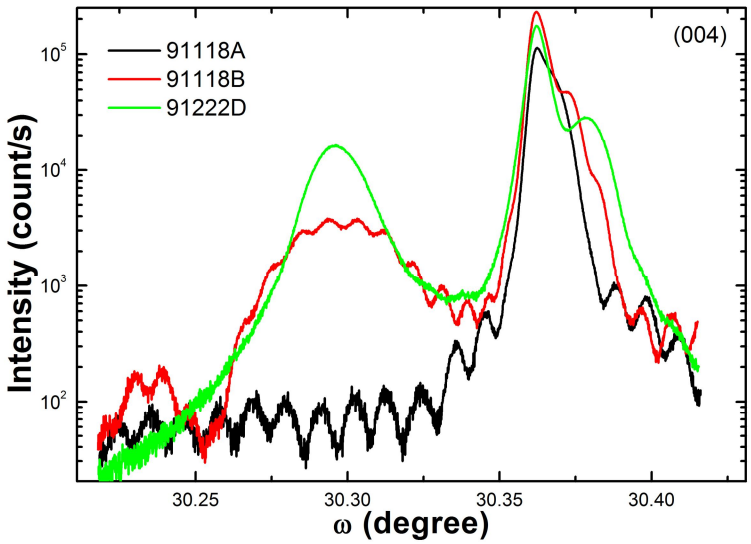

Figure 4.4. XRD (004) patterns for sample #91118A, #91118B, and #91222D.

The measured XRD (004) patterns for the samples in group A are shown in Figure 4.4. From the XRD (004) patterns, it can be noticed that: 1) For sample #91118A and #91118B, clear Pendellösung thickness fringes from GaSb epilayers are observed. It is reported that the critical thickness of ZnTe epilayer grown on GaSb substrate is about 180 nm using MOVPE [64,65]. Thus, it is reasonable to assume that the 500 nm thick ZnTe epilayer is largely relaxed during the growth so that the crystal quality of top GaSb layer is degraded to some extent. Correspondingly, the XRD pattern of sample #91222D shows very weakly defined thickness fringes. 2) The intensity of ZnTe diffraction peak increases as the thickness of ZnTe increases. For example, sample #91118A which contains only 40 nm thick ZnTe epilayer shows almost zero ZnTe peak intensity, while sample #91222D with 500 nm thick ZnTe shows the strongest ZnTe peak intensity. 3) By using the angle separation of Pendellösung fringes, the thickness can be determined by Equation (4.1):

$$T = \frac{\lambda}{2(\Delta\theta_P)\cos\theta}, \tag{4.1}$$

where T is the layer thickness, $\Delta\theta_P$ is the angle separation of Pendellösung fringes. Based on Equation (4.1), the GaSb layer thicknesses for sample #91118A and #91118B are determined to be 460 and 490 nm, respectively.

XRD ω-2θ curve is also simulated using X'Pert Epitaxy software. For comparison, the simulated ω-2θ curve for sample #91118B is plotted in Figure 4.5, which shows good agreement with the experimental data. Simulation result shows that the thicknesses for ZnTe and GaSb layers are about 120 and 490 nm, respectively.

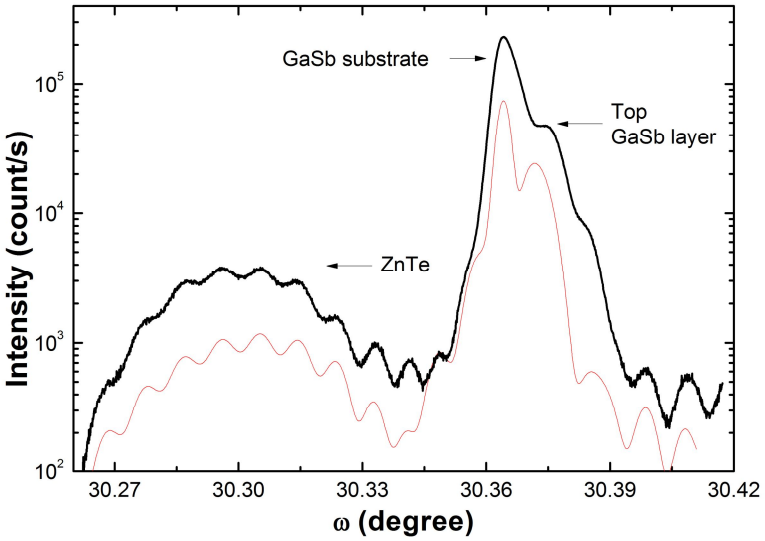

Figure 4.5. XRD experimental data (in black) and simulated curve (in red) for sample #91118B [71].

4.3.1.2 GaSb epilayers grown under temperature ramp

Another three samples (#110131A, #110408B and #110523A) that have GaSb epilayers grown under temperature ramps are studied in this section. Figure 4.6 shows the sample structures.

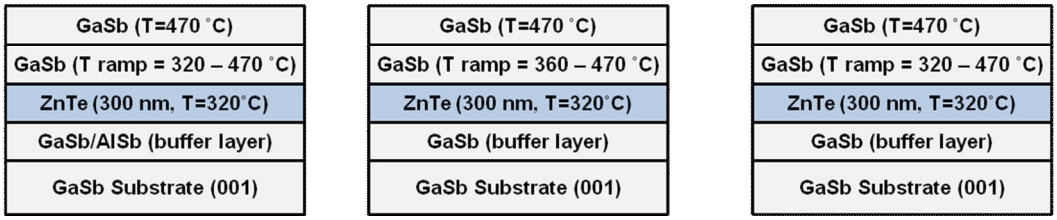

Figure 4.6. Structures of sample #110131A, # 110408B, and #110523A from left to right.

The measured XRD (004) patterns for the samples in group B and corresponding simulated curves are plotted in Figure 4.7, 4.8 and 4.9.

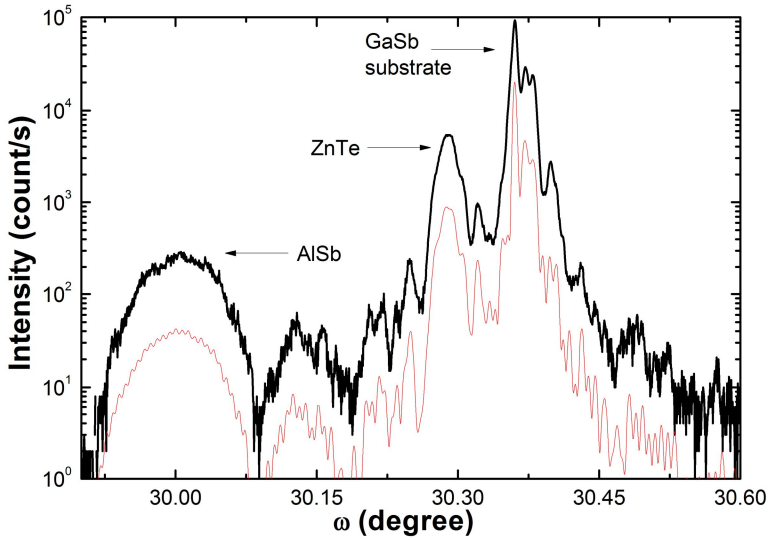

Figure 4.7. Experimental data (in black) and simulated curve (in red) of XRD (004) pattern for sample #110131A. Simulation result shows that the thicknesses for AlSb, ZnTe and GaSb layers are about 55, 325 and 410 nm, respectively.

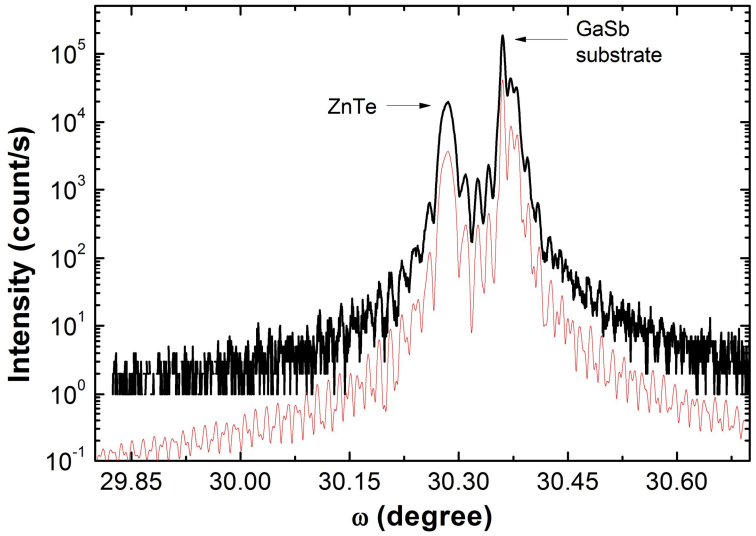

Figure 4.8. Experimental data (in black) and simulated curve (in red) of XRD (004) pattern for sample #110408B. Simulation result shows that the thicknesses for ZnTe and GaSb layers are about 300 and 380 nm, respectively [71].

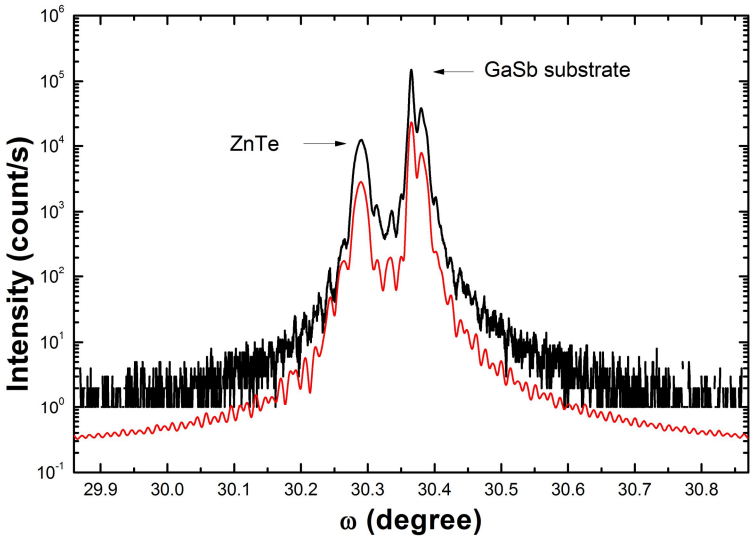

Figure 4.9. Experimental data (in black) and simulated curve (in red) of XRD (004) pattern for sample #110523A. Simulation result shows that the thicknesses for ZnTe and GaSb layers are about 280 and 380 nm, respectively.

It can be seen that the measured XRD patterns show clear diffraction peaks from the ZnTe epilayer, the GaSb epilayer and the GaSb substrate. Pendellösung thickness fringes are observed for all the samples. The simulated ω-2θ curves show that the diffraction fringes are a combination of Pendellösung

thickness fringes from both GaSb and ZnTe epilayers, indicating high-quality of GaSb and ZnTe single-crystal epitaxial layers with smooth interfaces, uniform thicknesses, and low defect densities. Based on the XRD simulation, the thicknesses of GaSb and ZnTe epilayers for each sample are determined and summarized in Table 4.2.

Table 4.2. Simulation results of thicknesses for ZnTe and GaSb epilayers.

Sample #	**thickness of ZnTe layer**	**thickness of GaSb layer**
110131A	325 nm	410 nm
110408B	300 nm	380 nm
110523A	280 nm	380 nm

By comparing the XRD patterns acquired on all the six samples in group A and group B (#91118A, #91118B, #91222D, #110131A, #110408B, and #110523A), it is observed that the diffraction peak of GaSb epilayer for each sample is on the right side of the GaSb substrate peak, which indicates that the vertical lattice parameter ($a_{\perp}$) of the GaSb epilayer is smaller than that of the GaSb substrate. The simulation results indicate that the ZnTe epilayer is partially relaxed. As a result, the GaSb epilayer is subjected to a tensile strain when it is grown on the partially relaxed ZnTe layer, leading to the smaller vertical lattice constant.

4.3.2 TEM measurements and results

Cross-sectional TEM is used in this study to investigate the ZnTe/GaSb and GaSb/ZnTe interface morphology, especially interfacial misfit dislocations.

The TEM samples are prepared by Dr. Lu Ouyang at Arizona State University using the same way as described in chapter 3.

As visible in Figure 4.10 and 4.11, low-magnification TEM images of samples #110408B and #110523A demonstrate excellent crystallinity as well as smooth morphology for both ZnTe/GaSb and GaSb/ZnTe interfaces. This observation clearly establishes that use of the GaSb transition layer grown with a temperature ramp prior to normal growth effectively prevents the GaSb/ZnTe interface from being damaged.

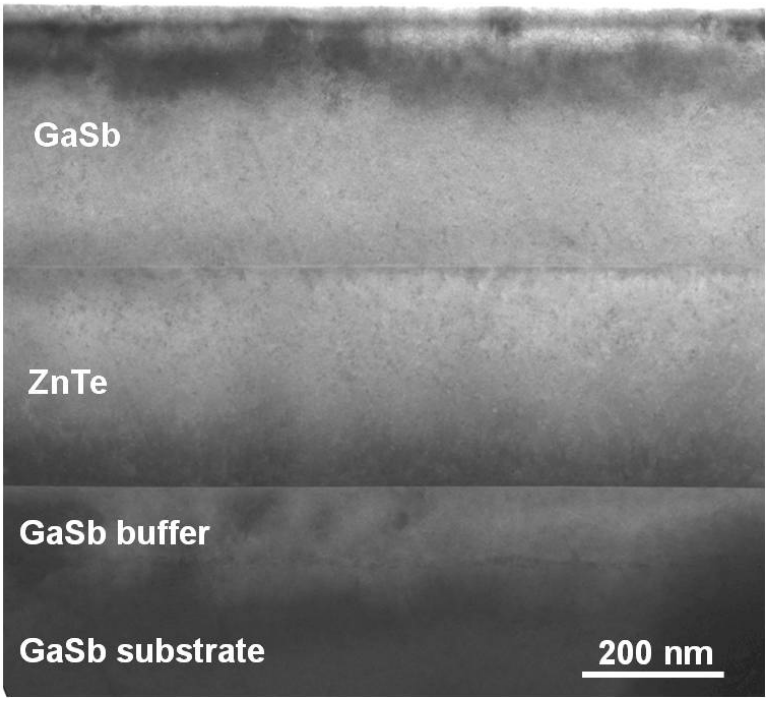

Figure 4.10. Low-magnification TEM image of sample #110408B [71].

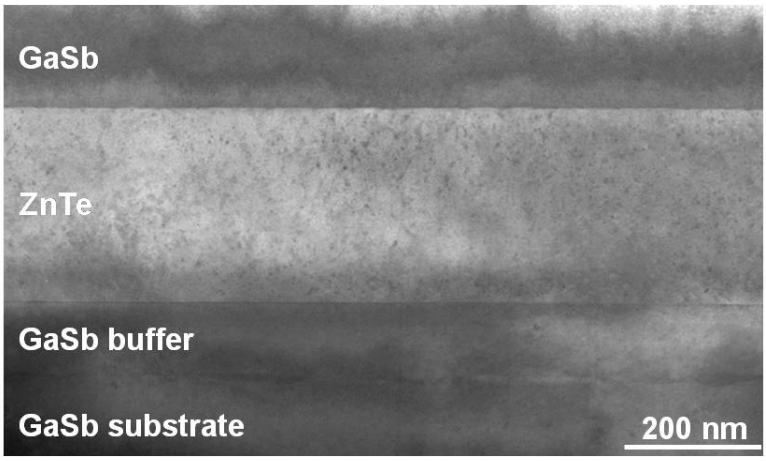

Figure 4.11. Low-magnification TEM image of sample #110523A [71].

Furthermore, the images reveal no misfit dislocations or stacking faults at either of the ZnTe/GaSb or GaSb/ZnTe interfaces, indicating that they are highly coherent with very low defect density, as expected due to the very small lattice mismatch between ZnTe and GaSb (~ 0.13%). In addition, the thicknesses of GaSb and ZnTe layers are also directly measured from the TEM images. For sample #110408B, Figure 4.10 shows that the GaSb and ZnTe layers are 380 nm and 300 nm thick, respectively, which confirms the XRD simulation results shown in Table 4.2.

4.3.3 PL measurements and results

PL measurements are carried out to investigate the optical properties of the GaSb epilayers. Since GaSb has the bandgap of 0.726 eV (~ 1708 nm) in the IR region, the 780 nm line of a laser diode is used for excitation and a Fourier transform infrared (FTIR) spectrometer configured with a quartz beam-splitter and liquid-nitrogen-cooled InSb detector is used for detection. To understand how the growth temperature condition affects the optical properties of GaSb epilayer,

sample #91118B, #110131A, #110408B and #110523A are studied and compared in this section.

It is known that low-temperature PL of GaSb has been well studied by many authors [73,79-83], and there are about 20 reported transitions in the range of 680 – 810 meV [73,79,80,83]. Among these transitions, three main PL lines are often observed and these have been discussed in optical characterization measurements: i) A PL line with maximum at 796 meV, denoted as "BE" or "BE4", which is considered as an emission of an exciton bound to a non-specified neutral acceptor [81]. ii) A PL line with maximum at 777 meV, denoted as the "A" line, which is ascribed to recombination at a native acceptor level (A) via Band-Acceptor (BA) or Donor-Acceptor Pair (DAP) transitions [80,82]. iii) A PL line with maximum around 758 meV, denoted as the "B" line, which is interpreted as a transition from another acceptor level (B) [80,82].

The PL spectra of four samples, as measured at 13 K, are shown in Figure 4.12(a) – 4.12(d).

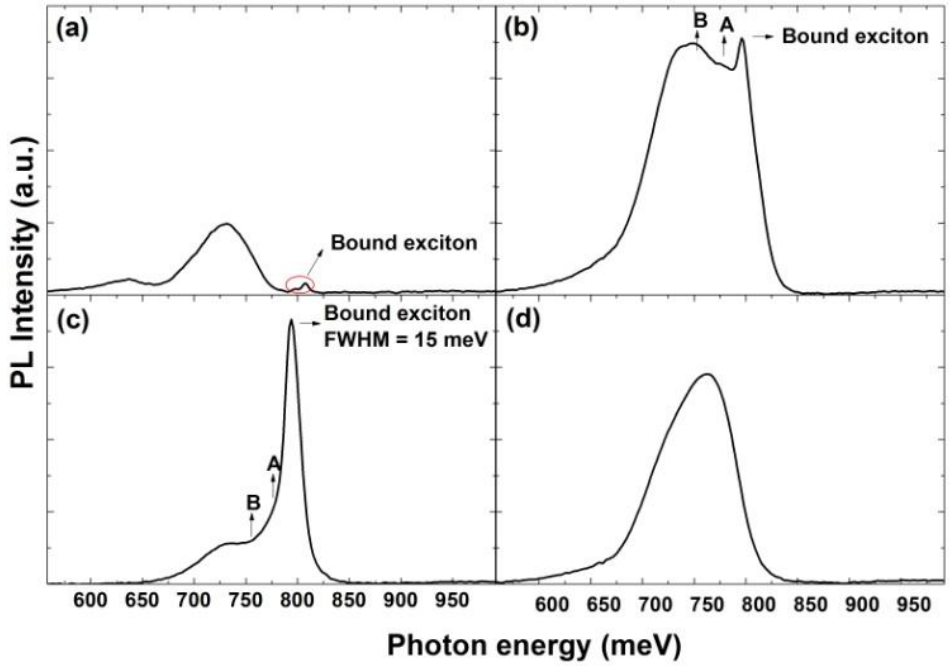

Figure 4.12. PL spectra measured at 13 K with excitation density of 16 W/cm^2 for: (a) sample #91118B, (b) sample #110131A, (c) sample #110408B, and (d) sample #110523A [71].

As shown in Figure 4.12(a), sample #91118B has very weak emissions from 793 meV to 807 meV, which are ascribed to the transitions from bound excitons [73,81-83]. The dominant PL feature is the emission in the range of 570 - 780 meV with peaks positioned around 637 meV and 728 meV. Since the growth of GaSb for sample #91118B is carried out at lower temperature (T_g = 380 ˚C), rather than the normal temperature (T_g = 470 ˚C), this broad emission is therefore attributed to optical transitions related to defects generated during the low-temperature growth. For sample #110131A, the intensity of emission from the bound exciton is increased by about 20 times relative to that of sample #91118B. A broad emission is observed in the range of 570 - 780 meV. Within this range, emission peaks are found around 777 and 758 meV, with intensities as strong as

that from the bound exciton. Thus, this broad emission is attributed to optical transitions from acceptor "A" and "B", and other growth-related defects. For sample #110408B, which contains the GaSb transition layer grown under T_{ramp} = 360 - 470 ˚C, the PL spectrum shows a narrow peak at 793 meV from the bound exciton with full width at half maximum (FWHM) of 15 meV. Similarly, a broad emission is observed between 650 meV and the bound exciton peak, which is attributed to emissions with the same origins as sample #110131A. Meanwhile, it is also noticed that this emission is greatly depressed in intensity and energy range (650 - 780 meV), which suggests a large decrease in the density of impurities and defects. For sample #4, the main PL feature is in the range of 570 - 850 meV. The emissions from acceptor "A", "B" and bound exciton are not well resolved in this case. Since the GaSb epilayers in this study were subjected to tensile strain when they were being grown on ZnTe layers, the change in bandgap of the strained GaSb can be estimated using the Luttinger-Kohn model and unitary transformation method [84-86]. The calculations show that the bandgaps of the GaSb epilayers are decreased due to tensile strain by 2.8 meV for sample #91118B and by 3.4 meV for samples #110131A, #110408B and #110523A. The experimental result shows the bound exciton peak energy of sample #110408B (793 meV) is 3 meV smaller than that of bulk GaSb (796 meV), which is in a good agreement with the calculation (3.4 meV). For sample #91118B, however, the PL spectrum does not show the expected shift in emission energy, which will be further investigated.

By comparing the PL spectra between sample #91118B and samples #110131A - #110523A, the latter show highly increased PL intensities, which indicates that use of the GaSb transition layer grown with a temperature ramp significantly improves the overall optical properties of GaSb. From closer comparison among samples #110131A, #110408B, and #110523A, it is also apparent that different temperature ramps affect optical properties differently. When the starting point of the temperature ramp is close to the growth temperature of ZnTe, the GaSb/ZnTe interface is expected to be less damaged while the optical properties of GaSb will be more deteriorated due to defects generated during the low-temperature growth. On the other hand, when the starting point of the temperature range is close to the growth temperature of GaSb, the ZnTe surface is more damaged during the initial GaSb growth so that the optical properties of GaSb are adversely affected due to the interfacial defects. Thus, it can be concluded that a temperature ramp starting from a reasonable compromise temperature, which is neither too close to the ZnTe growth temperature nor to the GaSb growth temperature, will shield the GaSb/ZnTe interface from severe damage while getting the temperature close enough to the normal GaSb growth temperature. As a result, excellent optical properties of GaSb can be achieved.

Temperature-dependent PL spectra of sample #110408B are shown in Figure 4.13. As the temperature is increased, the band-edge-related PL peak from GaSb shows a red-shift due to the decrease in the bandgap energy, while the

FWHM of the PL peak becomes broader as expected. In addition, the intensity of emission from defects and impurities gradually decreases and disappears above 140 K, which suggests that the non-radiative recombination mechanism is activated.

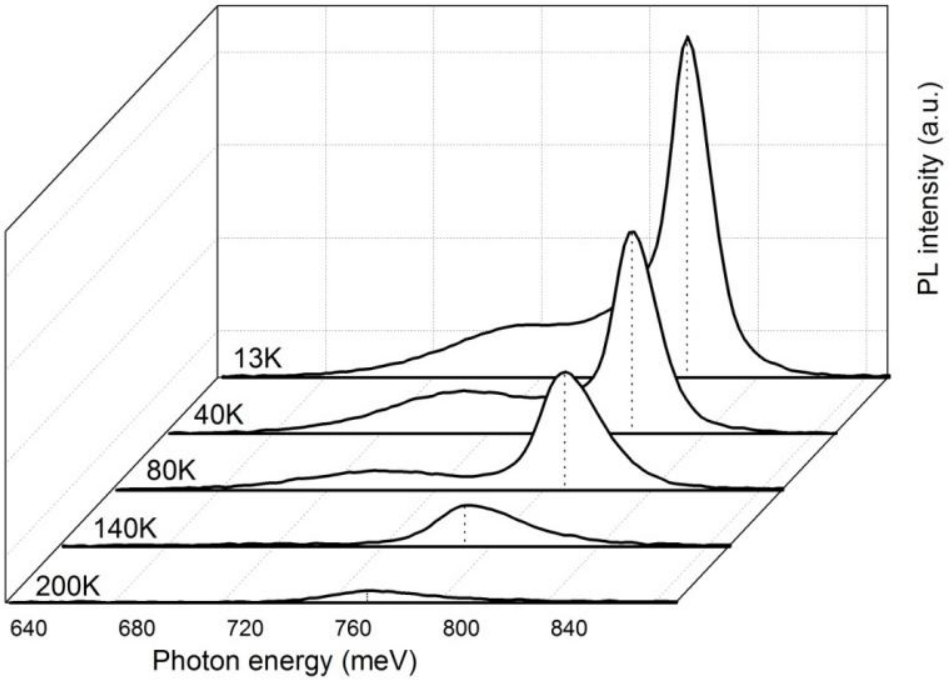

Figure 4.13. Temperature-dependent PL spectra measured from 13 - 200 K with excitation density of 16 W/cm^2 for sample #110408B [71].

4.4 Summary

The MBE growth of high quality GaSb layers on ZnTe/GaSb (001) composite substrates has been demonstrated. High-resolution XRD results show clear Pendellösung thickness fringes from both GaSb and ZnTe epilayers, and simulations fit the experimental data very well. TEM images show excellent crystallinity and smooth morphology for both ZnTe/GaSb and GaSb/ZnTe interfaces. No misfit dislocations or stacking faults are observed at the interfaces.

Strong PL emission from GaSb is observed from 13 to 200 K. The PL spectra show that the proposed GaSb transition layer grown on ZnTe while using a temperature ramp significantly improves the overall optical properties of GaSb.

Chapter 5

GaSb/ZnTe DOUBLE-HETEROSTRUCTURES

5.1 History of double-heterostructure

Double-heterostructures (DH) based on III-V or II-VI semiconductors have been widely used to provide strong electrical and optical confinement for both electronic and optoelectronic device applications, such as high-electron-mobility transistors (HEMTs), light-emitting diodes (LEDs), and laser diodes (LDs) [87,88]. Nowadays, DH structure LDs can be found in almost every home as part of a compact-disc (CD) player. The idea of using DH structure already emerged when Shockley proposed the application of a wide-gap emitter to achieve one-way injection in 1951 [89]. Later in 1957, some of the most important theoretical explorations at early stage of heterostructure were carried out by Herbert Kroemer, who introduced the concept of quasi-electric and quasi-magnetic fields in a graded heterojunction [90,91]. The next important step was taken several years until 1963, when Herbert Kroemer and Zhores Alferov independently proposed the concept of DH structure lasers [92,93] to achieve continuous-wave (CW) operation under room temperature. The biggest advantages of such DH structures over the existing homojunctions were predicted as the followings: 1) super-injection of carriers, 2) optical confinement, and 3) electron confinement. However, this concept was viewed skeptically by the research community at that time. It was believed to be impossible to find any couple of such “ideal” materials and fabricate those heterojunctions, since a lot of

conditions had to be satisfied such as compatibility of various properties in thermal, electrical, structural aspects. At that time, GaAs was found to have certain properties that were suitable for making optoelectronic devices. For example, GaAs has a small effective mass, wide direct bandgap, sharp optical absorption, high mobility and effective radiative recombination. To find materials compatible with GaAs, AlGaAs was chosen since it could be well lattice-matched with GaAs and was chemically stable and suitable for preparation of durable heterostructures. Therefore, GaAs-AlGaAs system was then extensively studied and believed to be a promising candidate for DH structure. In 1969, a laser composed of AlGaAs DH structure operated at room temperature was experimentally demonstrated for the first time [94]. Later in 1970, the DH structure laser operating continuously at room temperature was also realized [95]. This achievement was regarded as a milestone for semiconductor laser, leading to the birth of fiber-optical communication systems. Inspired by the electron confinement in DH structure, a new idea arose that a DH structure consisting of a ultra-thin middle layer, also known as quantum well structure, could have splitting energy levels as a result of quantum effect. In the 1970s, two important epitaxial growth techniques known as molecular beam epitaxy (MBE) and metal organic vapor phase epitaxy (MOVPE) appeared, which provided precise control of thickness, composition, planarity, etc. With significant development of these two growth techniques, various device structures composed of different DH material systems have been investigated using II-VI and III-V materials such as

ZnSe system [96-98], GaAs system [99-101], GaN system [3,7,102], and GaSb system [103-105].

5.2 GaSb/ZnTe double-heterostructure

GaSb-based structures have shown advantages and potentiality for applications in laser diodes [106,107], LWIR photodetectors [108], high frequency devices [109,110], high efficiency photovoltaic cells [111]. For heterostructures based on GaSb substrates, however, there is a lack of lattice-matched III-V semiconductors that can provide both strong electron and hole confinement for HEMTs, mid-wave infrared (MIR) LEDs, LDs and photodetectors. In the previous chapters, the lattice-matched 6.1-Å II-VI/III-V semiconductor platform has been introduced and proposed for various optoelectronic devices. Among all the compound materials in the 6.1-Å material platform, ZnTe and GaSb present the following properties which make them suitable for DH structures: 1) Both ZnTe and GaSb have lattice constants close to 6.1 Å with a very small mismatch of only 0.13%. Very low densities of misfit dislocations are generated during their epitaxial growth, as discussed in previous chapters. 2) ZnTe/GaSb heterojunction has a type-I band-edge alignment providing good carrier confinement for both electrons and holes, which is critical to the performance of high-efficiency light emitting devices. 3) There is a large difference in refractive index between ZnTe and GaSb [61], leading to an improved optical confinement for the guided optical modes in semiconductor lasers. Although all these properties are very attractive to optoelectronics

applications, to the best of our knowledge, there is no report in the literature on the experimental demonstration of such DH structures composed of III-V and II-VI semiconductors. Therefore, studies on the GaSb/ZnTe DH structure is of great interest for light-emitting devices and other potential applications. In this following sections, ZnTe/GaSb band offset, critical thickness of ZnTe on GaSb, MBE growth, and materials properties are discussed. A manuscript that reports the MBE growth and material characterization results has been submitted for publication [112].

5.3 ZnTe/GaSb band offset

The electronic structure of semiconductor heterostructures, especially the magnitude of the valence band discontinuity ΔE_v, is of great interest from a fundamental as well as application-oriented point of view. On one hand, research on the band offset helps the fundamental understanding of the nature of band discontinuity which is a prerequisite for the complete understanding of the physics of heterostructures. On the other hand, developing techniques to identify and control band offsets (ΔE_c and ΔE_v) has practical significance towards device engineering.

So far, a large number of experimental investigations have been carried out during the last several decades and shown that X-ray photoelectron spectroscopy (XPS) is one of the techniques that can yield a precise determination of band discontinuity. XPS can be regarded as the high-energy version of the photoelectric effect discovered by Hertz in 1887 which was later explained by

Albert Einstein (Nobel Prize in Physics 1921). X-ray photoemission spectroscopy is also known as electron spectroscopy for chemical analysis (ESCA), which is a quantitative spectroscopic technique measuring the elemental composition, chemical state and electronic states of the elements existing in a material. By using XPS, a lot of experimental data has been available for the band offsets of heterojunctions composed of materials in group III-V and IV [113-115]. Some results have been also acquired for the II-VI heterojunctions, such as ZnSe/ZnTe, ZnTe/CdSe, ZnTe/CdTe, CdSe/CdTe, etc [116-119]. In the following paragraphs of this session, the basic principle of XPS and experimental results on ZnTe/GaSb band offset are reviewed and summarized.

The working principle of XPS to determine valence band offset can be briefly explained and shown in the Figure 5.1, where E_{CL}^{X} is the energy of a core level in semiconductor X, E_{V}^{X} is the valence band maximum, and E_{C}^{X} is the conduction band minimum, E_{F} is semiconductor Fermi level, E_{G}^{X} is the bandgap of semiconductor X, and V_{BB}^{X} is the band bending potential at a surface or interface.

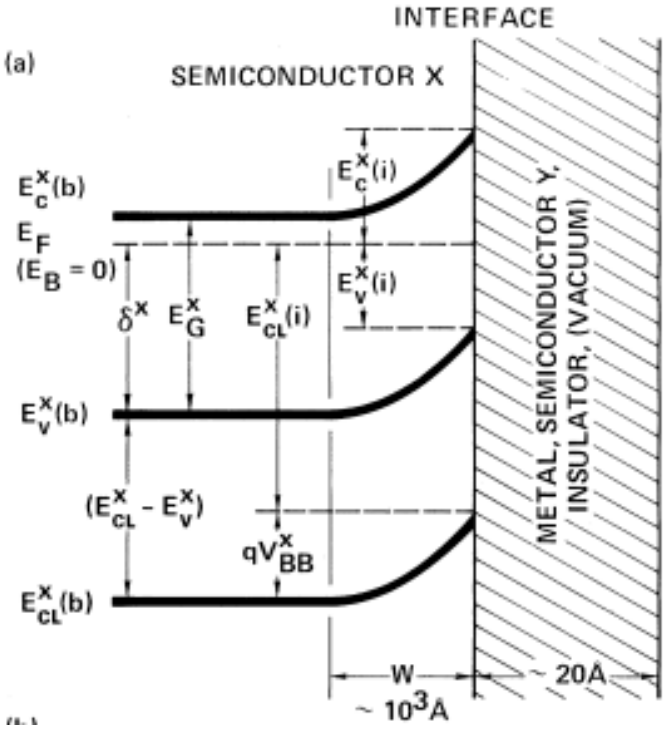

Figure 5.1. Energy band diagram at an abrupt interface (i) between a semiconductor and vacuum, metal, insulator, or a different semiconductor [113].

From Figure 5.1, the position of conduction band minimum at the interface (i) is given by

$$E_C^X(i) = (E_{CL}^X - E_V^X) + E_G^X - E_{CL}^X(i), \tag{5.1}$$

and therefore the position of valence band maximum at the interface (i) is given by

$$E_V^X(i) = E_{CL}^X(i) - (E_{CL}^X - E_V^X). \tag{5.2}$$

Similarly, for a heterojunction interface between semiconductor X and Y, the band edge diagram is shown as Figure 5.2. Then, the valence band offset ΔE_V at the heterojunction interface is given by

$$\Delta E_V = (E_{CL}^Y - E_V^Y) - (E_{CL}^X - E_V^X) - \Delta E_{CL}, \tag{5.3}$$

where $\Delta E_{CL} = E_{CL}^{Y}(i) - E_{CL}^{X}(i)$.

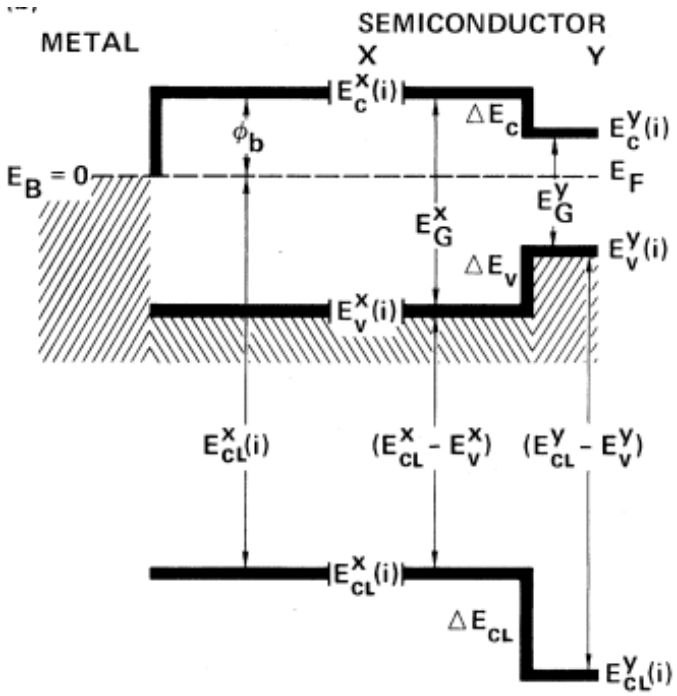

Figure 5.2. Energy band diagram at an abrupt interface between two semiconductors, X and Y [113].

In addition, $(E_{CL} - E_V)$ is the binding energy difference between the core level and the top of valence band for each semiconductor, which can be determined independently on the bulk semiconductors. As a result, all the information related to the interface are clearly contained in the term $\Delta E_{CL} = E_{CL}^{Y}(i) - E_{CL}^{X}(i)$. Therefore, the valence band offset for the heterostructure consisting of ZnTe and GaSb can be expressed as

$$\Delta E_V = (E_{Ga3d}^{GaSb} - E_V^{GaSb}) - (E_{Zn3d}^{ZnTe} - E_V^{ZnTe}) - (E_{Ga3d}^{GaSb} - E_{Zn3d}^{ZnTe}). \qquad (5.4)$$

Using XPS technique, band offset studies of ZnTe/GaSb heterostructure were primarily done by Wilke and Yu [120,121]. To measure the Ga 3*d* to Zn 3*d* core-level energy separation, a heterostructure sample consisting of 25 Å ZnTe on

GaSb substrate was grown using MBE. The XPS measurement results showed that the Zn 3*d* core-level to valence band edge binding energy was 9.42±0.04 eV, the Ga 3*d* core-level to valence band edge binding energy was 18.86±0.04 eV, and the Ga 3*d* to Zn 3*d* core-level energy separation was 8.84±0.03 eV. Based on Equation (5.4), the ZnTe/GaSb valence band offset is determined to be $\Delta E_V(ZnTe/GaSb) = 0.60 \pm 0.07\, eV$. The band edge diagram is shown as Figure 5.3 [121].

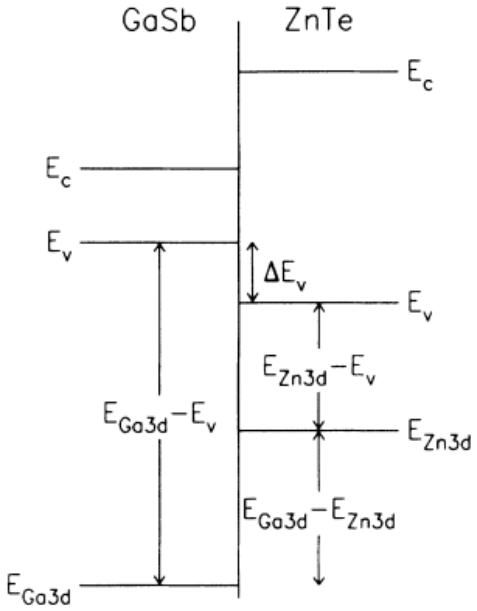

Figure 5.3. Energy band diagram for ZnTe/GaSb (001) heterostructure [121].

It has been reported by several authors that initial exposure of GaSb substrate to Zn flux leads to high structural quality at the interface [36,122,123]. And the effect of the Zn flux exposure on the band offset value for ZnTe/GaSb heterojunctions was studied by Yu [123]. In the study, a ZnTe/GaSb sample was grown with GaSb surface exposed to Zn flux for 60 seconds before ZnTe growth.

Then the XPS measurements were carried out. The results showed a different Ga 3*d* to Zn 3*d* core-level energy separation of 8.89±0.03 eV, compared to 8.84±0.03 eV for ZnTe/GaSb heterostructure without initial exposure to Zn flux. The valence band offset was then determined to be 0.55±0.07 eV, which was different from previous value (0.60±07 eV). This discrepancy shows that the interfacial growth condition has direct influence on band offset in ZnTe/GaSb heterostructures.

5.4 Critical thickness of ZnTe grown on GaSb

For heteroepitaxy growth, critical thickness (h_c) is an important parameter, below which the grown epilayer can be regarded to be pseudomorphic to substrate and no misfit dislocation is generated. If the layer thickness is above h_c, the strain in the epilayer due to lattice mismatch couldn't be held. Correspondingly, misfit dislocations and threading segments are formed to relieve the strain. When the strain gets fully relaxed, the lattice constant of epilayer will be recovered to bulk lattice constant.

To achieve good device performance, it is always desired to have defect free or very few misfit dislocation density generated in a device structure. Therefore, to make the GaSb/ZnTe DH structure suitable for device applications, it is necessary to study the critical thickness of ZnTe grown on GaSb. To estimate the critical thickness in a heteroepitaxy system, three well-known theoretical models including the models of Matthew and Blakeslee [124], Dunstan [125] and Cohen-Solal [126] have been widely used on various mismatched material

systems. In the following paragraphs, critical thickness for ZnTe grown on GaSb is calculated based on these three models. A few experimental reports in the literature are also reviewed.

In Matthew and Blakeslee model [124], it is assumed that the threading dislocations pre-existing in the substrate can elongate to form misfit dislocations in the epilayer and the critical thickness occurs when the misfit strain force matches the tension force in a line dislocation. When the layer thickness is beyond the critical thickness, the misfit strain force is larger than the tension force. As a result, the dislocations are generated at the interface. In this model, the critical thickness is given by

$$h_c = \frac{b(1-\nu\cos^2\alpha)}{8\pi f(1+\nu)\cos\beta}[\ln(\frac{h_c}{b})+1], \tag{5.5}$$

$$b = \frac{1}{2}a_l <110>, \tag{5.6}$$

$$f = \frac{a_l - a_s}{a_s}, \tag{5.7}$$

where h_c is critical thickness, b is Burgers vector, ν is Poisson's ratio, α and β are the angles between dislocation line and Burgers vector, f is the mismatch parameter, a_l is the lattice constant of epilayer, and a_s is the lattice constant of substrate. For ZnTe/GaSb heterostructure, a_l=a_{ZnTe}=6.1037 Å and a_s= a_{GaSb}=6.0959 Å, b=4.316 Å, f=0.13%. Assuming the dominant misfit dislocations are 60˚ type (α=β=60˚), the critical thickness is determined to be about 115 nm.

In Dunstan model [125], it is assumed that no misfit dislocation will be generated when the strain is less than b/md, where d is layer thickness, and m is a constant between 1 and 2. When the critical thickness occurs, we have

$$f = \frac{b}{mh_c}. \tag{5.8}$$

Therefore, the critical thickness is given by

$$h_c = \frac{b}{fm} \cong \left.\frac{b}{f}\right|_{m=1} = 330\,\text{nm}.$$

In Cohen-Solal model [126], it is assumed that the lattice mismatch at the interface is accommodated by a combination of strain and misfit dislocations. Using Keating's valence force approximation, the critical thickness is determined by a semi-empirical expression:

$$h_c = A^* \cdot f^{-3/2} \cdot a_l / 4, \tag{5.9}$$

where A^* is a constant. In the Cohen-Solal model, A is determined to be about 0.15 for semiconductors of Zincblende structure. Therefore, h_c=460 nm.

Regarding to experimental investigation, however, there are currently only two papers reporting h_c of ZnTe grown GaSb (001) substrate. In both two reports, ZnTe layers were deposited on GaSb (001) substrate using metal-organic vapor-phase epitaxy (MOVPE) [32,127]. In Ref. [127] h_c for ZnTe on GaSb were reported to be below 180 nm using XRD, while h_c was determined to be 800 nm using optical reflectivity in Ref. [32]. Recently, there is another paper reporting h_c of MBE grown ZnTe on GaSb (211)B substrate [128]. In this paper, the authors determined h_c value to be in a range of 350 to 375 nm based on a combination of

results from XRD and PL measurements. The theoretical and experimental results are summarized in Table 5.1. It can be seen that there are still some discrepancies among the experimental data and theoretical values.

Table 5.1. Theoretical and experimental h_c results for ZnTe grown on GaSb.

Models	h_c **(theoretical)**	h_c **(experimental)**	**Growth method and orientation**
Matthews-Blakeslee	115 nm	180 nm	MOVPE (001)
Dunstan	330 nm	800 nm	MOVPE (001)
Cohen-Solal	460 nm	350-375 nm	MBE (211)

5.5 MBE growth of GaSb/ZnTe double-heterostructures

The GaSb/ZnTe DH samples were grown using a dual-chamber MBE system at University of Notre Dame, as described in previous chapters. A vacuum level of about 5×10^{-9} Torr was maintained in the transfer chamber to prevent surface contamination during sample transfer. The growth temperatures were determined using a thermocouple positioned on the back of the substrate holder. During growth of the DH structure, a ZnTe epilayer was firstly deposited on a composite GaSb (001) buffer-substrate, as described in the previous chapters. After deposition of ZnTe in the II-VI chamber, the wafer was transferred to the III-V chamber where the GaSb growth was carried out. In Chapter 4, high quality growth of GaSb on ZnTe has been demonstrated using a temperature ramp applied for the region near the GaSb/ZnTe interface to protect the material from damage due to thermal evaporation. The characterization results showed that using a temperature ramp from 360 ˚C to 470 ˚C with a ramping rate of 33 ˚C/min during the GaSb growth was effective in protecting the GaSb/ZnTe interface and

achieving good material quality. After GaSb growth, the samples were transferred back to the II-VI chamber where another thin ZnTe layer was deposited on the GaSb layer to complete the DH structure. The growth parameters used for the samples described in this chapter are summarized in Table 5.2.

Table 5.2. Growth parameters for GaSb/ZnTe DH samples [112].

Layer Material	**Growth Temperature (°C)**	**Temperature Ramp (°C)**	**Ramping Rate (°C/min)**	**BEP Ratio**	**Growth Rate (μm/h)**
ZnTe	320	NA	NA	$\frac{Zn}{Te}=\frac{1.2}{1}$	1.1
GaSb	470	360-470	33	$\frac{Ga}{Sb}=\frac{1}{5}$	0.8
ZnTe	320	NA	NA	$\frac{Zn}{Te}=\frac{1.2}{1}$	1.1
GaSb (buffer)	470	NA	NA	$\frac{Ga}{Sb}=\frac{1}{5}$	0.8

5.6 Characterization results and discussion

After completion of growth, the XRD patterns of the samples were measured in the vicinity of the (004) and (113) diffraction peaks of the GaSb substrate. The high-resolution XRD patterns were recorded using a PANalytical X'Pert PRO MRD X-ray diffractometer with multi-crystal monochromator. The copper $K_{\alpha 1}$ line (1.54 Å) was used for the XRD measurements. In the (004) ω-2θ scan, separate diffraction peaks from the top and the bottom ZnTe epilayers, the

GaSb epilayer, and the GaSb substrate are clearly observed, as shown in Figure 5.4.

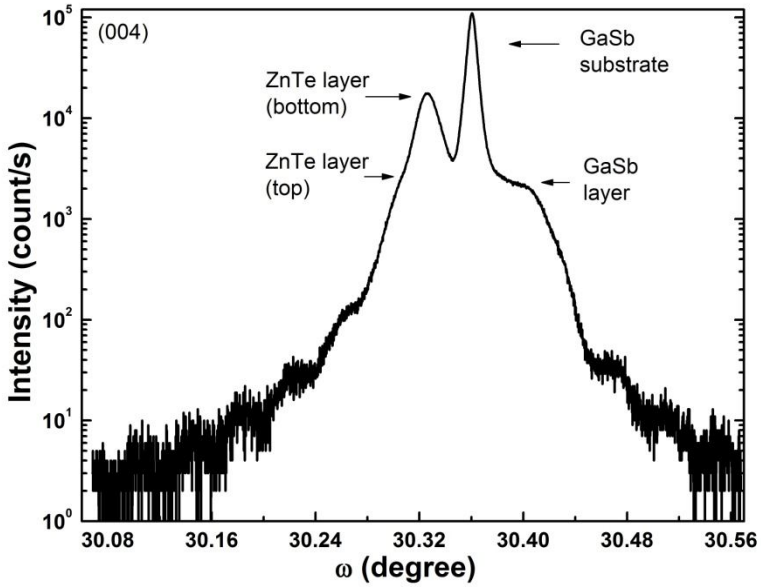

Figure 5.4. XRD (004) ω-2θ curve for GaSb/ZnTe DH sample [112].

The nominal thicknesses of the GaSb layer and the two ZnTe layers are 140 nm (GaSb layer), 150 nm (top ZnTe layer), and 950 nm (bottom ZnTe layer), respectively, as determined from the MBE nominal growth rates. To accurately determine the thickness of each layer, SEM images were taken using a XL30 ESEM-FEG system operated at 30 kV with spatial resolution of 3 nm. As shown in Figure 5.5, the layer thicknesses were determined to be 139 nm for GaSb layer, 146 nm for the upper ZnTe layer and 952 nm for the lower ZnTe layer, respectively.

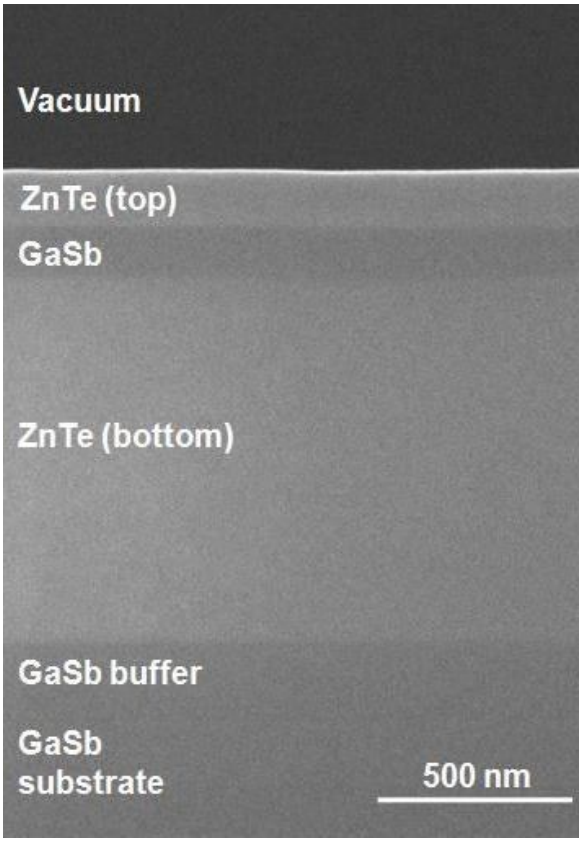

Figure 5.5. SEM image showing cross-section of GaSb/ZnTe DH sample [112].

These values are in close agreement with those determined from the MBE growth rates. From the (004) XRD pattern, it is also noticed that the diffraction peak of the GaSb epilayer has a smaller vertical lattice parameter ($a_{\perp}$) than that of the GaSb substrate. This decrease is attributed to relaxation of the bottom 950-nm-thick ZnTe layer during growth since ZnTe has a mismatch of 0.13% when grown on GaSb (a_{ZnTe}=6.104 Å, a_{GaSb}=6.096 Å). In the previous discussion on critical thickness, theoretical calculations using the models of Matthew and Blakeslee, Dunstan and Cohen-Solal show that the critical thickness for growth of ZnTe on GaSb is in the range of 110 - 460 nm. Consequently, the following thin GaSb epilayer of 140 nm grown on the relaxed ZnTe bottom layer would then be

subject to tensile strain. The lateral lattice constant ($a_{\|}$) of the thin GaSb epilayer is determined from the XRD (004) and (113) diffraction peaks. The calculations indicate that the strained GaSb epilayer is partially relaxed towards the bulk lattice constant by approximately 14%. Similarly, the top ZnTe epilayer is subject to compressive strain when it is grown on the partially relaxed GaSb layer, leading in this case to a larger vertical lattice constant. Thus, the top ZnTe diffraction peak has a smaller diffraction angle than that of the lower ZnTe diffraction peak. Similar behavior has been observed and reported for ZnTe layers grown on GaSb using MOVPE [65].

TEM study was carried out at Arizona State University by Prof. David Smith's group to investigate the ZnTe/GaSb and GaSb/ZnTe interface morphology and the presence of any misfit dislocations. Cross-sectional TEM specimens were prepared using mechanical polishing and dimpling followed by argon ion-milling. Liquid nitrogen temperature and low energy (2.5 - 3 keV) ion beams were used to minimize any thermal or ion-beam damage during milling. Images were recorded using a JEM-4000EX TEM operated at 400 kV with a structural resolution of ~ 1.7 Å. For the samples reported here, three interfaces were studied: the ZnTe/GaSb interface between the top ZnTe epilayer and the GaSb epilayer, denoted as interface A; the GaSb/ZnTe interface between the GaSb epilayer and the bottom ZnTe epilayer, denoted as interface B; and the ZnTe/GaSb interface between the bottom ZnTe epilayer and the GaSb buffer layer, denoted as interface C. As shown in Figure 5.6, the low-magnification TEM

image of the DH sample indicates very good crystallinity and smooth morphology for all three interfaces. There are no visible misfit dislocations or stacking faults present at interfaces A and C, as expected due to the very small lattice mismatch between ZnTe and GaSb (~ 0.13%). The high-magnification TEM image in Figure 5.7 confirms the high quality of the upper ZnTe layer, as grown on the GaSb layer, with a coherent interfacial configuration. The arrow indicates the location of coherent interface between top ZnTe and GaSb layer.

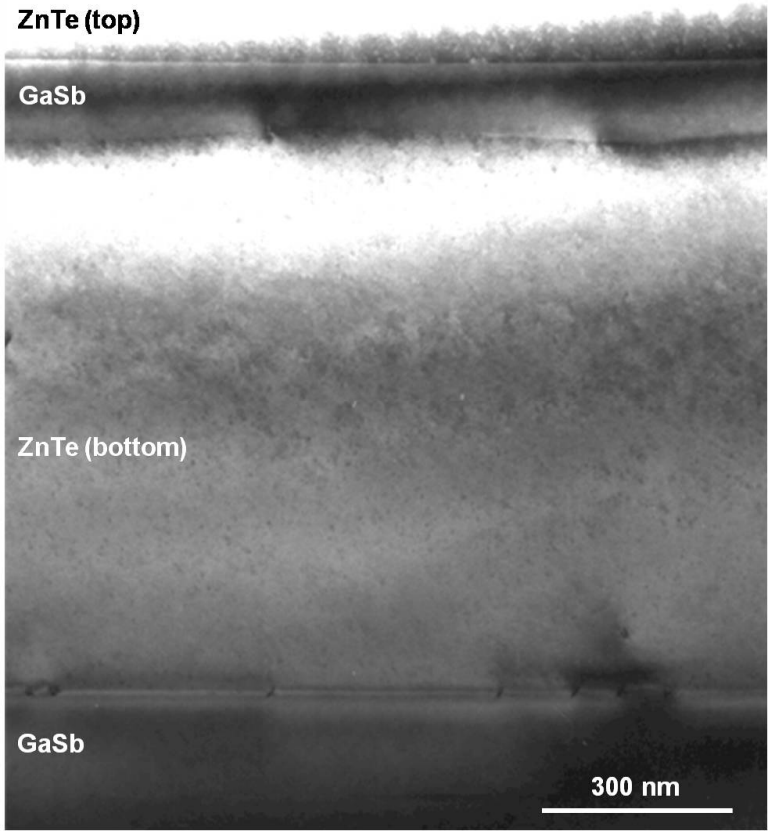

Figure 5.6. Low-magnification TEM image of GaSb/ZnTe DH sample [112].

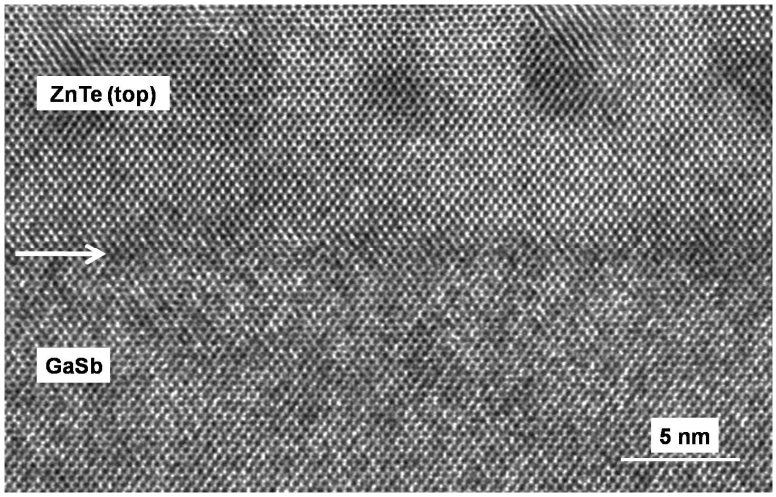

Figure 5.7. High-magnification TEM image of GaSb/ZnTe DH sample [112].

Although some well-separated dislocations are observed at the interface B, which are attributed to relaxation of the ZnTe layer due to its large thickness (~ 950 nm), it was previously reported in Chapter 4 that a nearly defect-free GaSb/ZnTe interface was achieved when GaSb was deposited under the same growth condition on a ZnTe layer of 300-nm thickness. All of these observations indicate that the MBE-grown GaSb/ZnTe DH samples overall have highly coherent interfaces and excellent microstructure. It is also reasonable to expect that a GaSb/ZnTe DH with even better material quality could be achieved if grown with a bottom ZnTe layer below the critical thickness.

To study optical properties, PL measurements were carried out using a 780-nm laser diode for excitation at an intensity of about 10 W/cm^2. PL emission from the samples was measured using a Fourier transform infrared (FTIR) spectrometer equipped with a CaF_2 beam-splitter and liquid-nitrogen-cooled InSb detector. As shown in Figure 5.8, the PL spectrum recorded at 13 K is dominated by two narrow emission peaks at 796 meV with a full-width-at-half-maximum

(FWHM) of 9.5 meV, and at 777 meV with a FWHM of 9 meV. With increase of temperature from 13 to 30 K, the peak position of 796-meV line does not shift but its intensity decreases. This behavior is typical for thermal decay of bound excitons. Therefore, the peak at 796 meV is ascribed to an emission of excitons bound to nonspecific neutral acceptors, as reported by several authors, and denoted as "BE" or "BE4" [73,80,81]. The peak at 777 meV is attributed to recombination processes involving a native acceptor level (A), denoted as "A" line [80,82]. Another broad PL emission is also observed with maximum around 758 meV, which is interpreted as a transition from another acceptor level (B) [80,82].

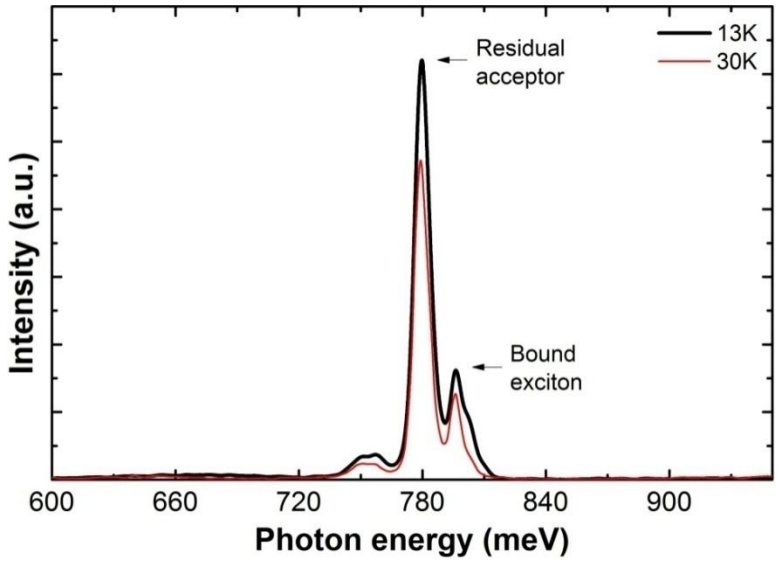

Figure 5.8. PL spectra for GaSb/ZnTe DH sample measured at 13 K and 30 K [112].

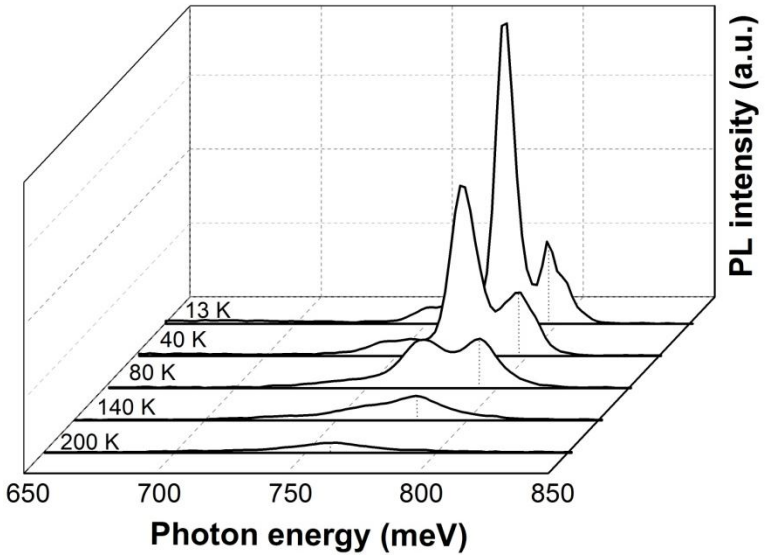

Figure 5.9. Temperature-dependent PL spectra for GaSb/ZnTe DH sample [112].

Temperature-dependent PL spectra are measured up to 200K, as shown in Figure 5.9. As the temperature is increased from 40 to 200 K, the band-edge-related PL peak from GaSb shows a red-shift due to the decrease in the bandgap energy, while the FWHM of the PL peak becomes broader, as expected. In addition, the "A" line becomes thermally quenched off after the temperature is increased beyond 140 K, indicating that the non-radiative recombination mechanism has been activated. The PL spectrum is then dominated by a single peak associated with the recombination between free electrons and free holes.

5.7 Summary

GaSb/ZnTe DH structure is proposed for use in light-emitting devices. Literature review of the reports on ZnTe/GaSb band offset is present. Critical thickness for ZnTe on GaSb is calculated using Matthew and Blakeslee, Dunstan, and Cohen-Solal models. Growth of high quality GaSb/ZnTe DH structures using MBE is successfully demonstrated. High-resolution XRD results show clear

diffraction peaks from each epilayer. SEM images confirm the layer thicknesses in an excellent agreement with estimates of nominal thicknesses based on the MBE growth rate. Electron micrographs demonstrate overall excellent crystallinity and highly coherent interfaces. Strong PL emission from the samples is observed at temperatures from 13 to 200 K. Based on these results, it is concluded that the proposed GaSb/ZnTe double-heterostructure is experimentally demonstrated for the first time with excellent structural and optical properties.

Chapter 6

ZnTe/GaSb DISTRIBUTED BRAGG REFLECTORS

6.1 Vertical-cavity surface-emitting lasers

6.1.1 History of VCSELs

Vertical-cavity surface-emitting laser (VCSEL) is considered as one of the most important devices for high-speed optical local-area networks (LANs) and optical interconnects. So far, they have been widely used in various kinds of equipments and computer systems. The history of VCSELs can be simply summarized by three time periods. In the first time period (1977-1988), the original concept of VCSELs was proposed by Kenichi Iga (at the Tokyo Institute of Technology, Japan) in 1977 [129]. Later in 1979, the first VCSEL device was demonstrated [9]. Then in 1984, the VCSEL in pulsed operation was achieved under room temperature [130]. From 1988 to 1999, VCSELs stepped into its second time period, during which a lot of research effort was made on continuous-wave (CW) operation and device feasibility. The first VCSEL in CW operation at room temperature was demonstrated in 1988 [10]. Studies on GaAs-based VCSELs were extensively carried out in the 1990s [131-134]. VCSEL emitting at 1.3 μm near room temperature was demonstrated on InP substrate [135]. Research on green-blue-UV VCSEL also started during this time period [136,137]. Since 1999, VCSELs have reached its third time period. Optical transmitters based on VCSELs have been introduced in high-speed LANs. A lot of work is made towards production, manufacturing, extension of applications.

6.1.2 Device characteristics of VCSELs

The structure of VCSELs is different from conventional stripe lasers. They contain a vertical cavity formed by the surfaces of epitaxial layers. Thus, light is emitted from surfaces.

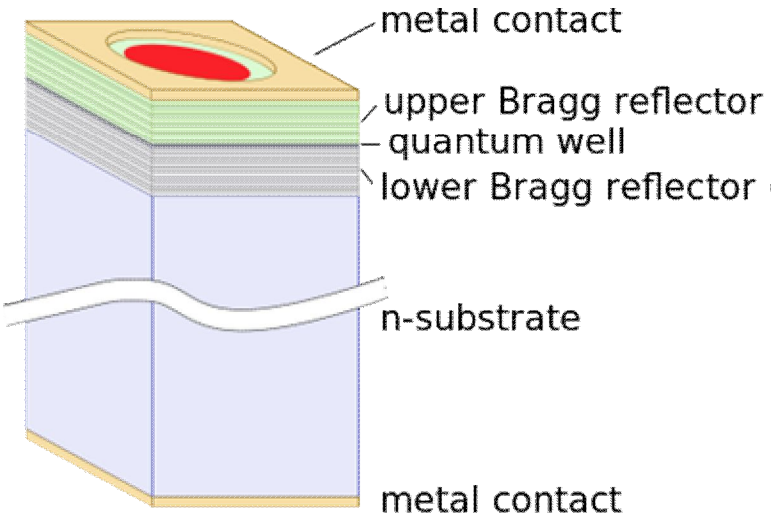

Figure 6.1. Schematic diagram of a typical VCSEL.

As seen in Figure 6.1, the common structure of VCSEL consists of two parallel reflectors which sandwich a thin active layer. The reflectivity has to be high enough (>99%) to reach the lasing threshold. Due to such unique structure, VCSELs show the following advantages and properties [138]:

1) Ultralow threshold operation due to its small cavity volume;

2) Dynamic single-mode operation;

3) Wide and continuous wavelength tuning;

4) High relaxation frequency even at low driving current;

5) Easy coupling to optical fiber;

6) Monolithic fabrication and easy device separation without the need for perfect cleaving.

To compare VCSEL with stripe lasers, some of the key characteristics are shown in Table 6.1 [139].

Table 6.1. Comparison of characteristics between VCSELs and stripe lasers [139].

Parameter	**VCSELs**	**Stripe lasers**
Active layer area	5 ×5 μm^2	3 ×300 μm^2
Active volume	0.07 μm^3	60 μm^3
Cavity length	1 μm	300 μm
Reflectivity	~ 99-99.9%	~ 30%
Optical confinement (transverse)	~ 50-80%	~ 3-5%
Optical confinement (longitudinal)	2 ×1% × 3 (3QWs)	~ 50%
Relaxation frequency	> 10 GHz	< 5 GHz

6.2 Distributed Bragg reflectors

6.2.1 Introduction of distributed Bragg reflectors

Distributed Bragg reflector (DBR) is a structure consisting of an alternating sequence of layers made from two different materials. DBR is very often used as a mirror of high reflectance in various optoelectronic devices, such as VCSELs, resonant cavity LEDs (RCLEDs) and Fabry-Perot modulators.

A typical DBR structure has several pairs of layers. Each pair contains a high refractive index layer adjacent to a low refractive index layer. To achieve high reflectance, each layer should have thickness of $\lambda/(4n)$ to reach constructive interference of the reflected waves from the interfaces. n is refractive index of the respective layers and λ is the reflection wavelength. In general, the DBR reflectance increases with the number of quarter-wavelength ($\lambda/4$) pairs and it is

also proportional to the refractive index difference between the high and low index materials. An important consideration for the choice of DBR materials is based on maximizing refractive index contrast. To reach large difference in refractive index, the DBR layers can be made of dielectric materials (for example, n(ZnSe)-n(CaF_2)=1.2 at 980 nm [140]), so that a small number of λ/4 pairs can be obtained.

Besides dielectric materials, a lot of research has also been made on the development of DBRs using semiconductor materials. With great successes in semiconductor growth techniques (for example, MBE and MOCVD), such DBRs can be epitaxially grown with high material quality and current injection through the DBR mirrors can be realized. However, for commonly used semiconductors in a DBR system, the refractive index contrast is not as high as the one of the DBR made from dielectric materials. For example, compared with n(ZnSe)-n(CaF_2)=1.2 at 980 nm, semiconductors GaAs and AlAs show n(AlAs)-n(GaAs)=0.5 at 980 nm. As a result, the number of λ/4 pairs needs to be larger to achieve high reflectivity.

Sometimes, a few semiconductor systems have very small refractive index contrast. For example, in the InP-based VCSELs, the DBR mirrors are made of InGaAsP/InP or AlInGaAs/AlInAs alloys which are lattice-matched to InP. However, the refractive index contrast of these material systems is quite small (Δn ~0.3 at 1.55 μm). For VCSELs emitting at 1.3 μm, the refractive index contrast has to be further reduced to 0.2 due to the increase in the bandgap of the DBR

layer materials to avoid absorption. As a result, it would need growth of 65 λ/4 pairs to reach 99.9% reflectivity, which also requires longer growth time, higher material cost, and other issues for VCSEL devices. To decrease the number of λ/4 pairs while keeping the same reflectivity, one alternative solution is to grow non-lattice-matched DBRs followed by wafer-bonding to optical cavity. It is reported that DBR mirrors consisting of GaAs-AlAs layers was grown separately and then wafer-bonded to the optical cavity for VCSEL emitting at 1.3 μm [141].

6.2.2 ZnTe/GaSb distributed Bragg reflectors

In order to improve device performance, reliability and manufacturability, it is always highly desirable to develop a DBR system made of materials with lattice-matched constants and large refractive index contrast. As introduced in the previous chapters, 6.1-Å semiconductor material system consists of both II-VI (MgZnCdHg)(SeTe) and III-V (InGaAl)(AsSb) compound semiconductors. In this material system, semiconductors ZnTe and GaSb and their heterostructures have shown unique material properties, which make them naturally suitable for DBRs used in various optoelectronic devices.

As discussed in Chapter 3, Chapter 4 and Chapter 5, ZnTe and GaSb are almost perfectly lattice-matched with a lattice mismatch of only 0.13%. High quality ZnTe/GaSb, GaSb/ZnTe, and ZnTe/GaSb/ZnTe heterostructures have been successfully demonstrated with very low density of misfit dislocations. Therefore, it is reasonable to expect that the ZnTe/GaSb DBRs can be compatible and integrated to GaSb-based devices. Another important fact is that GaSb and

ZnTe have a large refractive index contrast in mid-infrared (MIR) range (for example, Δn=1.18 at 0.6 eV). This refractive index contrast is significantly higher than those of InP- and GaSb-based DBRs, which have been widely used in VCSELs emitting in NIR and MIR spectral range. As a result, the DBR structure consisting of ZnTe and GaSb can provide very high reflectance with fewer pairs of $\lambda/4$ layers. This will also help to reduce the overall DBR thickness as well as the materials cost. To make comparisons, the refractive index contrasts of commonly used DBRs in NIR and MIR range are summarized in Table 6.2 [142-145].

Table 6.2. Comparison of DBRs used in NIR and MIR spectral range [142-145].

DBR materials	**Refractive index contrast (Δn)**	**No. of pairs for 99.9%**	**Lasing wavelength (μm)**
InGaAsP/InP	0.18	65	1.3
AlGaInAs/InP	0.19	63	1.3
AlGaAsSb/AlAsSb	0.49	27	1.3
AlAs/GaAs	0.50	23	1.3
AlGaAsSb/AlAsSb	0.44	31	1.55
AlGaAsSb/InP	0.43	33	1.55
AlGaInAs/InP	0.34	38	1.55
AlGaInAs/AlInAs	0.30	43	1.55
GaInAsP/InP	0.27	51	1.55
InGaAs/InAlAs	0.27	30	2.3
AlAsSb/GaSb	0.6	23	2.5

From a device perspective, it is known that the semiconductor lasers emitting in 2.0 - 3.0 μm are of great interest for gas detection and spectroscopy. Such wavelength range covers several strong absorption lines of atmospheric

pollutants, such as CO, CH_4, NO_2, NH_3, and HF. A lot of research efforts have been made in VCSELs emitting between 2 and 3 μm. While InP-based heterostructures have shown a wavelength limit of emission up to 2.3 μm [144], GaSb-based heterostructure allow coverage of a major part of 2-4 μm. So far, VCSELs emitting at 2.3 μm in CW operation at room temperature have been achieved [146], and laser emission in pulsed operation at 2.63 μm at room temperature has also been demonstrate [145]. To further develop and improve GaSb-based VCSELs for better performance, for example, lower threshold current, less optical losses and longer emitting wavelength, it is worthy of time and effort considering a new monolithically grown DBR that can achieve higher reflectivity with fewer number of λ/4 pairs and less optical losses, such as the ZnTe/GaSb DBR. In the following sections of this chapter, optical modeling, growth and material properties of the ZnTe/GaSb DBRs are discussed. Some of the results have been accepted for publication [147].

6.3 Optical modeling for thin films

One of the most important properties for a DBR mirror is its reflectance spectrum. Therefore, it is necessary to understand how light is interacted with a thin film including reflection and transmission. In this session, an optical model is built to study the reflectance of a thin film. The final goal of this optical modeling is to calculate the reflectance of the ZnTe/GaSb DBR stack.

In the following discussions, the layer structure and material properties are assumed to be homogeneous on the plane perpendicular to the direction of light

propagation. With this assumption, the reflectance calculation is reduced from a three dimensional problem into a one dimensional form. To derive an optical model generally valid for any thin film, three different cases of light reflection are studied and discussed in the followings.

6.3.1 Reflection from a simple boundary

A thin film may consist of several boundaries between materials of different refractive indices. At any boundary (interface) between two different media, reflection occurs. Therefore, it is necessary to discuss the simplest case--the reflection from a simple boundary. As shown in Figure 6.2, the incoming wave is incident on a surface which separates two media of refractive index n_1 and n_2. θ_1 is the incident angle. Based on Snell's law, the reflection angle is equal to the incident angle, and the refraction angle θ_2 is determined by Equation (6.1):

$$n_1 \cdot \sin\theta_1 = n_2 \cdot \sin\theta_2 . \tag{6.1}$$

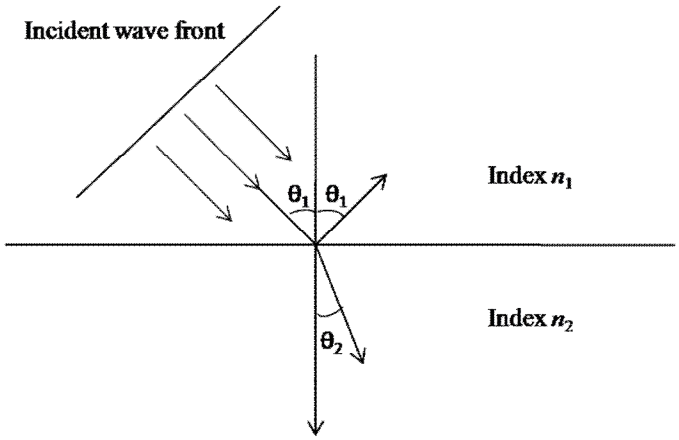

Figure 6.2. Reflection from a simple boundary.

When light is reflected or transmitted at oblique incidence, the light is classified into p- and s-polarized waves depending on the oscillatory direction of

its electric field. A wave with its electric vector in the plane of incidence is known as p-polarized or TM (transverse magnetic) wave, and a wave with electric vector normal to the plane of incidence is known as s-polarized or TE (transverse electric) wave. Figure 6.3 and 6.4 show reflection and transmission for both p- and s-polarized waves. The vectors for electric field and magnetic field are represented by ***E*** and ***B***.

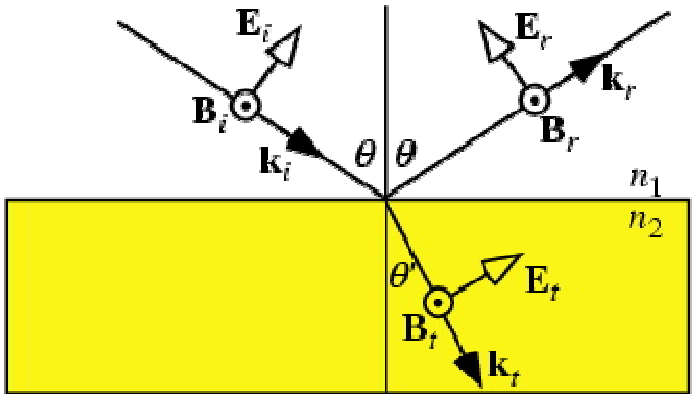

Figure 6.3. Reflection and transmission for light of p-polarization.

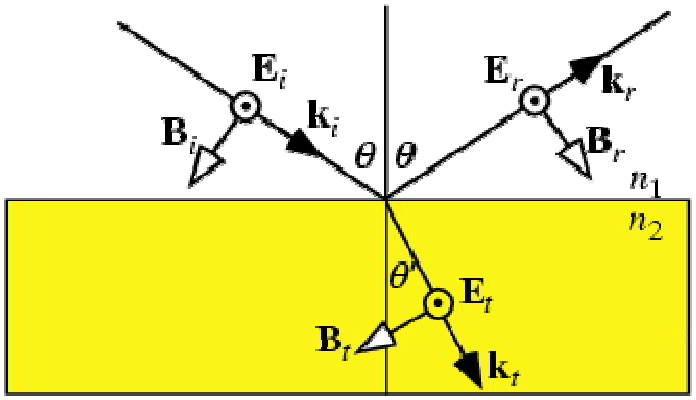

Figure 6.4. Reflection and transmission for light of s-polarization.

Based on Maxwell's equations, the boundary conditions for electromagnetic waves require that the components of ***E*** and ***B*** parallel to an interface should be continuous at the interface. For p-polarized light we then have

$$E_{ip}\cos\theta_i - E_{rp}\cos\theta_r = E_{tp}\cos\theta_t, \tag{6.2}$$

$$B_{ip} + B_{rp} = B_{tp}, \tag{6.3}$$

and for s-polarized light we have

$$E_{is} + E_{rs} = E_{ts}, \tag{6.4}$$

$$-B_{is}\cos\theta_i + B_{rp}\cos\theta_r = -B_{ts}\cos\theta_t, \tag{6.5}$$

where r and t are the amplitude coefficients for reflection and transmission, the letters p and s in the subscript represent p- and s-polarization, and the letters i and t in the subscript represent the media for incident light and transmitted light.

In the following discussions, we only focus on the normal incidence which is the relevant situation for 1D analysis of a DBR system. Under normal incidence (θ_i=θ_r=θ_t=0), p- and s-polarizations cannot be distinguished any more. The boundary conditions for $\boldsymbol{E}$ and $\boldsymbol{B}$ can be simplified and expressed as

$$E_t = E_i + E_r, \tag{6.6}$$

$$B_t = B_i - B_r. \tag{6.7}$$

In a medium with a refractive index of n, it is known that

$$E = (c/n)\cdot B = (c/n)\cdot\mu\cdot H = H/(n\cdot\gamma), \tag{6.8}$$

where $\gamma = \sqrt{\dfrac{\varepsilon_0}{\mu_0}}$. Therefore, Equation (6.7) can be also expressed as

$$H_t = \gamma\cdot n_i\cdot(E_i - E_r). \tag{6.8}$$

Then the amplitude coefficient for reflection under normal incidence can be determined by

$$r \equiv \frac{E_r}{E_i} = \frac{\frac{1}{2}[E_t - H_t/(\gamma \cdot n_i)]}{\frac{1}{2}[E_t + H_t/(\gamma \cdot n_i)]} = \frac{[\gamma \cdot n_i - H_t/E_t]}{[\gamma \cdot n_i + H_t/E_t]} = \frac{n_i - n_t}{n_i + n_t}. \quad (6.9)$$

The amplitude coefficient for transmission is given by

$$t \equiv \frac{E_t}{E_i} = \frac{2n_i}{n_i + n_t}. \quad (6.10)$$

Finally, the reflectance R and transmittance T are determined by $R = r \cdot r^* = |r|^2$ and $T = 1 - R$.

For absorbing materials, the refractive index is a complex number ($N=n-ik$). Equations from (6.1) to (6.10) are still valid with the refractive index n replaced by the complex refractive index N. In the following discussions, the refractive index is always referred as the complex refractive index N.

6.3.2 Reflection from a single layer film

Based on the above analysis for a simple boundary, similar discussion can be extended to the case of a single layer film. For this case, the film structure consists of a single layer deposited on a substrate, as shown in Figure 6.5. Under normal incidence, $\theta_0=\theta_1=0$.

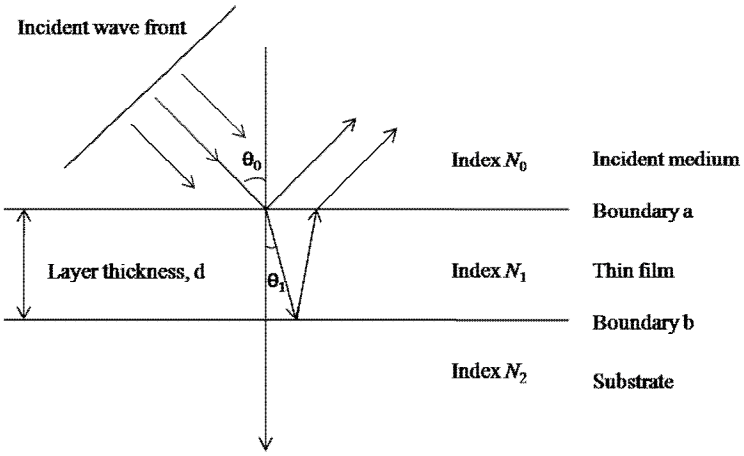

Figure 6.5. Plane wave incident on a single layer film.

If the direction of the incident beam is defined to be positive (denoted by symbol +), and the opposite direction as negative (denoted by symbol -), the tangential components of electric and magnetic fields at the interface b are satisfied with

$$E_b = E_{1b}^{+} + E_{1b}^{-}, \tag{6.11}$$

$$H_b = \gamma \cdot N_1 \cdot (E_{1b}^{+} - E_{1b}^{-}) = \gamma_1 \cdot (E_{1b}^{+} - E_{1b}^{-}), \tag{6.12}$$

where $\gamma_1 = \gamma \cdot N_1$. Therefore, we obtain

$$E_{1b}^{+} = \frac{1}{2}(H_b / \gamma_1 + E_b), \tag{6.13}$$

$$E_{1b}^{-} = \frac{1}{2}(-H_b / \gamma_1 + E_b), \tag{6.14}$$

$$H_{1b}^{+} = \gamma_1 \cdot E_{1b}^{+} = \frac{1}{2}(H_b + \gamma_1 E_b), \tag{6.15}$$

$$H_{1b}^{-} = -\gamma_1 \cdot E_{1b}^{-} = \frac{1}{2}(H_b - \gamma_1 E_b). \tag{6.16}$$

When a wave propagates from interface b to interface a, the wave is expected to have a phase shift determined by the layer thickness d. By multiplying a phase factor $e^{i\Delta}$, the tangential components of electric and magnetic fields at the interface b can be expressed by

$$E_{1a}^{+} = E_{1b}^{+} \cdot e^{i\Delta} = \frac{1}{2}(H_b / \gamma_1 + E_b) \cdot e^{i\Delta}, \tag{6.17}$$

$$E_{1a}^{-} = E_{1b}^{-} \cdot e^{-i\Delta} = \frac{1}{2}(-H_b / \gamma_1 + E_b) \cdot e^{-i\Delta}, \tag{6.18}$$

$$H_{1a}^{+} = H_{1b}^{+} \cdot e^{i\Delta} = \frac{1}{2}(H_b + \gamma_1 E_b) \cdot e^{i\Delta}, \tag{6.19}$$

$$H_{1a}^{-} = H_{1b}^{+} \cdot e^{-i\Delta} = \frac{1}{2}(H_b - \gamma_1 E_b) \cdot e^{-i\Delta}, \tag{6.20}$$

where $\Delta = 2\pi N_1 d / \lambda$.

From Equation (6.17) - (6.20), we obtain

$$E_a = E_{1a}^{+} + E_{1a}^{-} = E_b \cos\Delta + H_b (i \sin\Delta / \gamma_1), \tag{6.21}$$

$$H_a = H_{1a}^{+} + H_{1a}^{-} = E_b (i \sin\Delta)\gamma_1 + H_b \cos\Delta. \tag{6.22}$$

Equation (6.21) and (6.22) can be further simplified into a matrix notation as

$$\begin{bmatrix} E_a \\ H_a \end{bmatrix} = \begin{bmatrix} \cos\Delta & i(\sin\Delta)/\gamma_1 \\ i(\sin\Delta)\gamma_1 & \cos\Delta \end{bmatrix} \begin{bmatrix} E_b \\ H_b \end{bmatrix} = [m] \begin{bmatrix} E_b \\ H_b \end{bmatrix}, \tag{6.23}$$

where

$$[m] = \begin{bmatrix} \cos\Delta & i(\sin\Delta)/(\gamma \cdot N_1) \\ i(\sin\Delta) \cdot (\gamma \cdot N_1) & \cos\Delta \end{bmatrix}. \tag{6.24}$$

It can be seen that the matrix $[m]$ connects the tangential components of electric and magnetic fields at interface *a* and interface *b*.

Based on the Equation (6.9) derived previously for the reflection from a simple boundary, the amplitude coefficient of reflection from a single layer film can be similarly derived and expressed by

$$r \equiv \frac{E_r}{E_i} = \frac{[\gamma \cdot N_i - H_t / E_t]}{[\gamma \cdot N_i + H_t / E_t]} = \frac{[\gamma \cdot N_0 - H_a / E_a]}{[\gamma \cdot N_0 + H_a / E_a]}. \tag{6.25}$$

From Equation (6.23), we have

$$\begin{bmatrix} E_a / E_b \\ H_a / E_b \end{bmatrix} = [m] \begin{bmatrix} 1 \\ \gamma \cdot N_2 \end{bmatrix} = \begin{bmatrix} \cos\Delta & i(\sin\Delta)/(\gamma \cdot N_1) \\ i(\sin\Delta) \cdot (\gamma \cdot N_1) & \cos\Delta \end{bmatrix} \begin{bmatrix} 1 \\ \gamma \cdot N_2 \end{bmatrix}. \tag{6.26}$$

Therefore, H_a / E_a can be calculated by

$$\frac{H_a}{E_a} = \frac{[H_a / E_b]}{[E_a / E_b]} = \frac{[\cos\Delta \cdot (\gamma \cdot N_2) + i(\sin\Delta) \cdot (\gamma \cdot N_1)]}{[\cos\Delta + i(\sin\Delta) \cdot (N_2 / N_1)]}. \tag{6.27}$$

Combining Equation (6.25) and (6.27), the reflection amplitude coefficient can be finally expressed as

$$r \equiv \frac{E_r}{E_i} = \frac{\gamma \cdot N_0 - \dfrac{\cos\Delta \cdot (\gamma \cdot N_2) + i(\sin\Delta) \cdot (\gamma \cdot N_1)}{\cos\Delta + i(\sin\Delta) \cdot (N_2 / N_1)}}{\gamma \cdot N_0 + \dfrac{\cos\Delta \cdot (\gamma \cdot N_2) + i(\sin\Delta) \cdot (\gamma \cdot N_1)}{\cos\Delta + i(\sin\Delta) \cdot (N_2 / N_1)}}. \tag{6.28}$$

6.3.3 Reflection from a multilayer film

Assuming a multilayer film containing total number of w layers grown on substrate, each layer has different refractive index N_i (i=1…, w). Therefore, the matrix equation for the layer next to the substrate (the w^{th} layer) is given by

$$\begin{bmatrix} E_w \\ H_w \end{bmatrix} = \begin{bmatrix} \cos\Delta_w & i(\sin\Delta_w)/(\gamma \cdot N_w) \\ i(\sin\Delta_w) \cdot (\gamma \cdot N_w) & \cos\Delta_w \end{bmatrix} \begin{bmatrix} E_{sub} \\ H_{sub} \end{bmatrix}, \tag{6.29}$$

where $\Delta_w = 2\pi N_w d_w / \lambda$.

Similarly, for the (w-1)th layer and the wth layer, we have

$$\begin{bmatrix} E_{w-1} \\ H_{w-1} \end{bmatrix} = \begin{bmatrix} \cos\Delta_{w-1} & i(\sin\Delta_{w-1})/(\gamma \cdot N_{w-1}) \\ i(\sin\Delta_{w-1}) \cdot (\gamma \cdot N_{w-1}) & \cos\Delta_{w-1} \end{bmatrix} \begin{bmatrix} E_w \\ H_w \end{bmatrix}. \qquad (6.30)$$

It is clearly seen that such a matrix equation can be applied and extended to every layer in a countdown sequence. Therefore, the matrix for the whole film is expressed as

$$\begin{bmatrix} E_1 \\ H_1 \end{bmatrix} = \left\{ \prod_{q=1}^{w} \begin{bmatrix} \cos\Delta_q & i(\sin\Delta_q)/(\gamma \cdot N_q) \\ i(\sin\Delta_q) \cdot (\gamma \cdot N_q) & \cos\Delta_q \end{bmatrix} \right\} \begin{bmatrix} E_{sub} \\ H_{sub} \end{bmatrix} = [M] \begin{bmatrix} E_{sub} \\ H_{sub} \end{bmatrix}, \quad (6.31)$$

where

$$[M] = \prod_{q=1}^{w} \begin{bmatrix} \cos\Delta_q & i(\sin\Delta_q)/(\gamma \cdot N_q) \\ i(\sin\Delta_q) \cdot (\gamma \cdot N_q) & \cos\Delta_q \end{bmatrix} \equiv \begin{bmatrix} M_{11} & M_{12} \\ M_{21} & M_{22} \end{bmatrix}. \quad (6.32)$$

Equation (6.31) can be transformed to

$$\begin{bmatrix} E_1/E_{sub} \\ H_1/E_{sub} \end{bmatrix} = \begin{bmatrix} M_{11} & M_{12} \\ M_{21} & M_{22} \end{bmatrix} \begin{bmatrix} 1 \\ H_{sub}/E_{sub} \end{bmatrix} = \begin{bmatrix} M_{11} & M_{12} \\ M_{21} & M_{22} \end{bmatrix} \begin{bmatrix} 1 \\ \gamma \cdot N_{sub} \end{bmatrix}. \quad (6.33)$$

Thus, the amplitude coefficient of reflection from a multilayer film is determined by

$$r \equiv \frac{E_r}{E_i} = \frac{[\gamma \cdot N_0 - H_1/E_1]}{[\gamma \cdot N_0 + H_1/E_1]} = \frac{\gamma \cdot N_0 - \dfrac{M_{21} + M_{22} \cdot \gamma \cdot N_{sub}}{M_{11} + M_{12} \cdot \gamma \cdot N_{sub}}}{\gamma \cdot N_0 + \dfrac{M_{21} + M_{22} \cdot \gamma \cdot N_{sub}}{M_{11} + M_{12} \cdot \gamma \cdot N_{sub}}}. \qquad (6.34)$$

6.4 ZnTe/GaSb DBR modeling results and discussion

Based on the optical modeling derived in the Session 6.3, reflectance for ZnTe/GaSb DBRs is numerically calculated. The input parameters are refractive indices of layer materials, layer thicknesses, and number of λ/4 pairs. For

refractive index, experimental data measured from bulk ZnTe and GaSb are used in the calculation [148]. Their refractive indices in the spectral range from 0.2 to 0.7 eV are parameterized and extracted using Sellmeier equation [149], as plotted in Figure 6.6. Within this spectral range, the imaginary part of the indices (*k*) are ignored since ZnTe and GaSb are optically transparent.

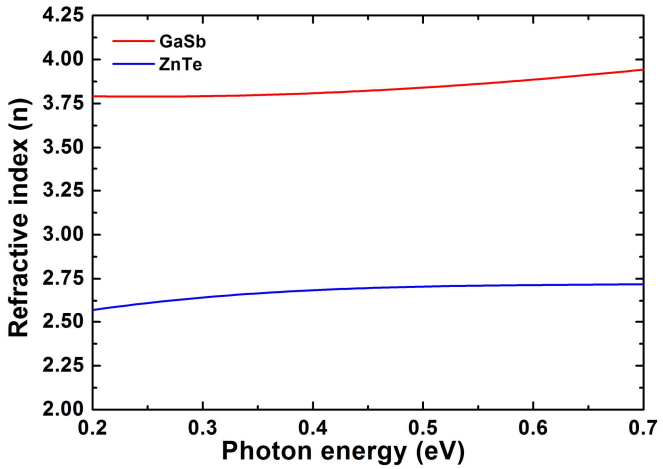

Figure 6.6. Refractive indices (*n*) for bulk ZnTe and GaSb.

The thickness of each DBR layer is equal to λ/4, where λ is the wavelength of peak reflectance. It is also commonly set equal to the lasing wavelength when designing VCSELs. In the following calculations, the wavelength λ is set to 2.3 μm.

To study how the reflectance of the ZnTe/GaSb DBRs varies with number of λ/4 pairs (N), calculations are also carried out with N =1 to 10. The structure configuration of the DBRs used in the calculation is shown as Figure 6.7.

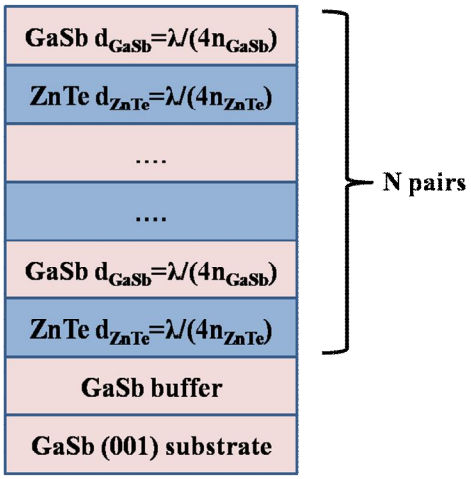

Figure 6.7. Layer structure of the ZnTe/GaSb DBRs used in the calculation.

Refractive indices for ZnTe and GaSb at 2.3 μm are determined from Figure 6.6, as n_{ZnTe}=2.710 and n_{GaSb}=3.857. Therefore, their layer thicknesses are designed as $d_{ZnTe}=\lambda/(4n_{ZnTe})$=212.2 nm and $d_{GaSb}=\lambda/(4n_{GaSb})$=149.1 nm. The calculated reflectivity spectra are plotted in the Figure 6.8. The relationship between peak reflectance and number of λ/4 pairs is also plotted in Figure 6.9.

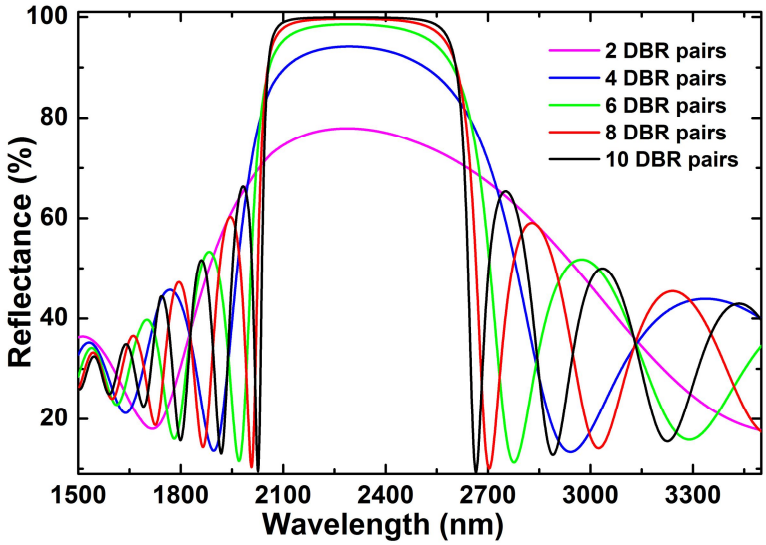

Figure 6.8. Calculated reflectivity spectra for ZnTe/GaSb DBRs [147].

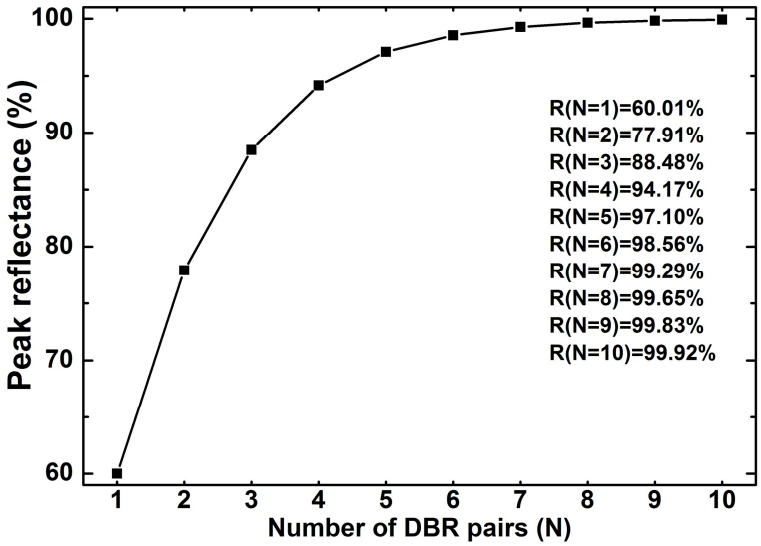

Figure 6.9. Peak reflectance versus number of λ/4 pairs [147].

From the two figures, it can be seen that 1) as the number of λ/4 pairs increases, the peak reflectance monotonously increases. With only one ZnTe/GaSb λ/4 pair, reflectance as high as 60% is already achieved. When the number of λ/4 pairs equals to 7, reflectance higher than 99% is expected. 2) When the number of λ/4 pairs is above 6, the reflection stopband is clearly present. With further increase in the number of pairs, the stopband gets flatter and wider which provide more capabilities for continuous wavelength tuning in VCSELs. In Table 6.3, we summarize the main parameters and modeling results acquired from ZnTe/GaSb DBR structures, and compare them with AlAsSb/GaSb- and InGaAs/InAlAs-DBRs that are commonly used for 2.3-μm VCSELs. It is shown that reflectance as high as 99.9% with only 10 pairs of λ/4 layers can be achieved for ZnTe/GaSb DBRs. To reach similar reflectance, it requires 20 and 30 periods for the other two DBRs with 2 to 3 times film thickness. By using ZnTe/GaSb DBRs, the thickness of overall structure can be reduced to 4 μm or even less.

Table 6.3. Comparison of different DBRs used for VCSELs emitting at 2.3 μm [147].

[DBR materials] /substrate	Refractive Index Contrast (Δn)	Number of $\lambda/4$ Pairs (N)	Calculated Peak Reflectivity	Total Thickness
[ZnTe/GaSb]/GaSb	1.18	10	99.9%	3.6 μm
[AlAsSb/GaSb]/GaSb	0.6	20	99.7%	6.6 μm
[InGaAs/InAlAs]/InP	0.27	30	99.4%	10.5 μm

6.5 MBE growth of ZnTe/GaSb DBRs

The ZnTe/GaSb DBR samples are grown using the same dual-chamber MBE system at University of Notre Dame, described in the previous chapters. The whole DBR structure is grown on GaSb (001) substrate. Since the DBR structure consists of an alternating sequence of ZnTe and GaSb layers, ZnTe and GaSb epilayers are monolithically grown on top of each other. Based on the previous studies in Chapter 3 to Chapter 5, ZnTe epilayers are deposited at 320 ˚C in II-VI chamber and GaSb epilayers are grown in III-V chamber using a temperature ramp method to protect ZnTe layer surfaces and achieve high material quality. During the growth, the wafer is transferred between II-VI and III-V chamber several times to finish the whole structure. The detailed growth conditions, such as growth temperatures, temperature ramping rate, BEP ratios, growth rates, are kept the same as the ones used for GaSb/ZnTe DH samples described in Chapter 5.

In this study, a set of 5 samples consisting of different number of λ/4 pairs and layer thicknesses are grown. The information for the number of DBR periods, nominal thicknesses for ZnTe and GaSb layers are summarized in Table 6.4.

Table 6.4. Number of λ/4 pairs and layer thicknesses for the MBE grown ZnTe/GaSb DBR samples.

Sample number (#)	**λ/4 pairs (N)**	**ZnTe layer thickness (nm)**	**GaSb layer thickness (nm)**
1	1	147	104
2	2	190	135
3	4	190	135
4	7	190	135
5	7	230	164

6.6 Characterization results and discussion

After completion of growth, the XRD patterns of the samples are measured in the vicinity of the (004) diffraction peak of GaSb substrate. The (004) ω-2θ curve for sample #4 is shown in Figure 6.10. Pendellösung fringes are clearly observed, indicating high interface smoothness, excellent composition and thickness uniformities of all the layers. The (004) XRD pattern is also simulated using X'Pert Epitaxy software. The ZnTe and GaSb layer thicknesses are set equal to 190 and 135 nm, respectively, which are estimated from the growth rates. Compared with the experimental data, the simulated results show an excellent agreement with the experimental curve.

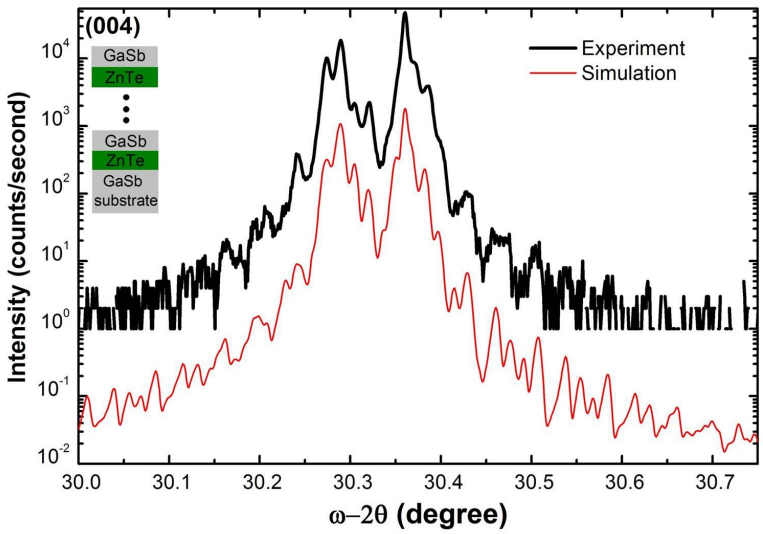

Figure 6.10. Measured and simulated XRD patterns for a ZnTe/GaSb DBR with 4 pairs [147].

To accurately determine the thickness of each layer, cross-section profiles of the ZnTe/GaSb DBR samples are taken using SEM. The SEM image for sample # 5 is shown in Figure 6.11. The white regions represent ZnTe and the dark layers represent GaSb. The SEM image shows well-defined flat ZnTe/GaSb interfaces. The layer thicknesses for ZnTe and GaSb are determined to be d_{ZnTe}=231±10 nm and d_{GaSb}=165±10 nm, which are in close agreement with those determined from the MBE growth rates.

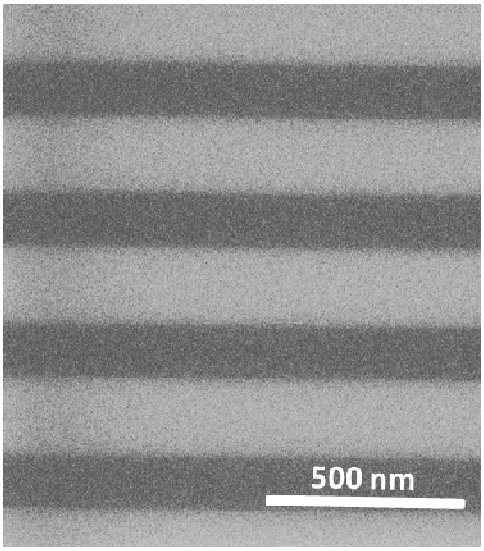

Figure 6.11. Cross-sectional SEM image of a ZnTe/GaSb DBR sample.

To study the surface morphology of the grown DBR samples, atomic force microscopy (AFM) measurements are carried out. The AFM images of the sample # 4 and #5 are shown as Figure 6.12(a) and 6.12(b). A well-defined step-flow growth mode is observed. The root mean square (RMS) surface roughness of sample #4 and sample #5 are found of ~ 0.691 and 0.185 nm, respectively, for a 3 × 3 μm^2 area.

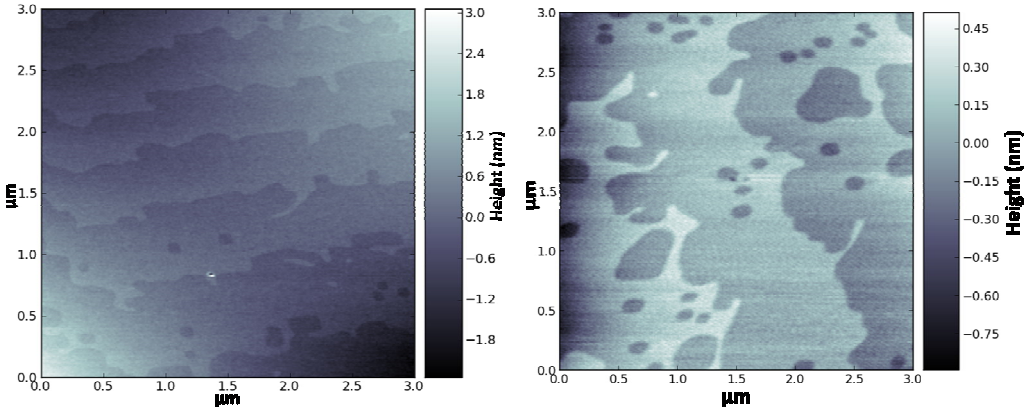

Figure 6.12. (a) AFM image for the surface of sample #4 (left). (b) AFM image for the surface of sample #5 (right).

To investigate interface morphology and misfit dislocations in the grown DBR samples, cross-sectional TEM images are recorded by Prof. David Smith's group at Arizona State University. As shown in Figure 6.13, the low-magnification TEM image of sample #4 indicates overall good crystallinity and smooth morphology for all the ZnTe/GaSb and GaSb/ZnTe interfaces. Very few misfit dislocations and no stacking faults are visible at the interfaces.

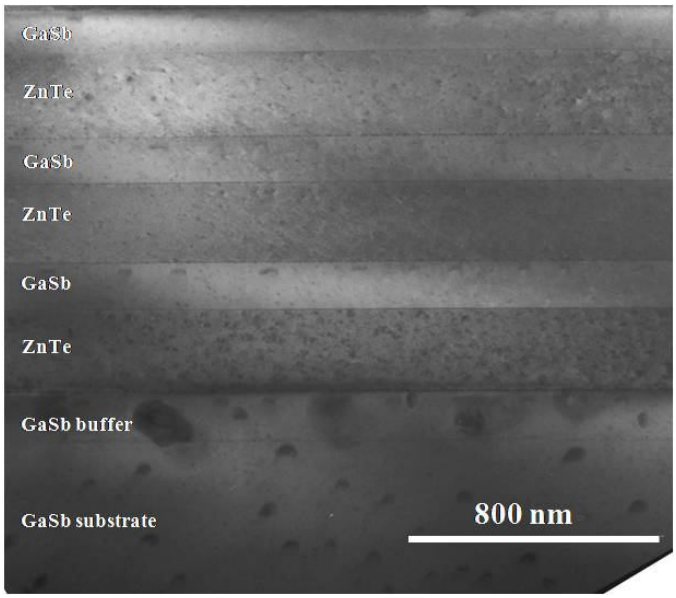

Figure 6.13. Low-magnification TEM image of a DBR sample with 7 pairs.

The reflectance measurements are carried out at normal incidence using a Globar as the light source. The incident light passes through an optical microscope and gets focused on the sample surface. The reflectivity spectra are measured by a FTIR which is equipped with a CaF_2 beam-splitter and a liquid-nitrogen-cooled MCT detector. Since the reflectivity of gold (Au) is well known for high reflectivity in the IR range, a piece of Au film prepared by e-beam

deposition is used as the control sample. The reflectivity of Au under normal incidence is plotted, as shown in Figure 6.14.

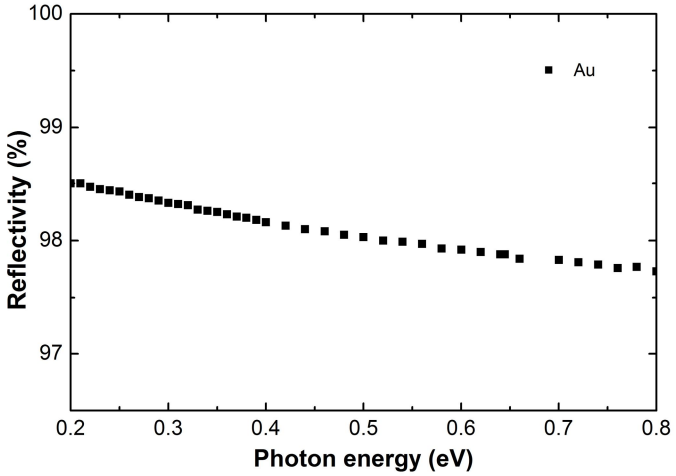

Figure 6.14. Reflectivity of Au in the range from 0.2 - 0.8 eV.

To determine the reflectance of the DBR samples, signals of reflection from Au film and DBR samples have to be both measured. In the measurement on Au film, the information from system background such as absorptions due to atmosphere and optics, electronic noises, and light source fluctuations are also included. The measured reflection signals from the Au film and DBR samples are shown respectively, as Figure 6.15 and Figure 6.16. The noisy signals around 1600 and 3800 cm^{-1} are due to the absorption of water and CO_2 in the atmosphere.

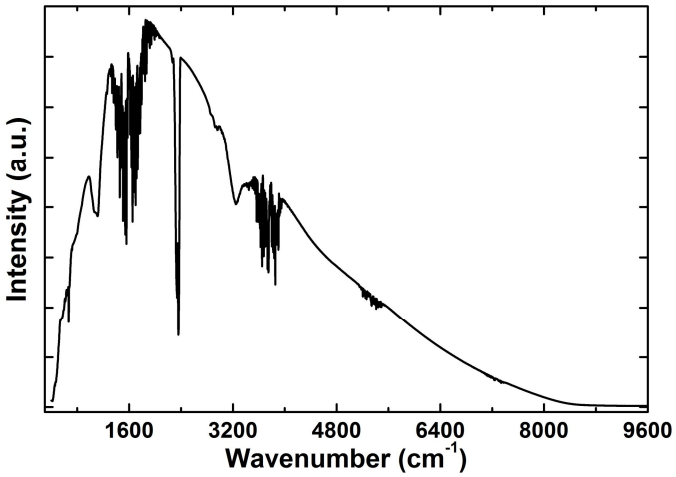

Figure 6.15. Reflection signal measured from the Au film.

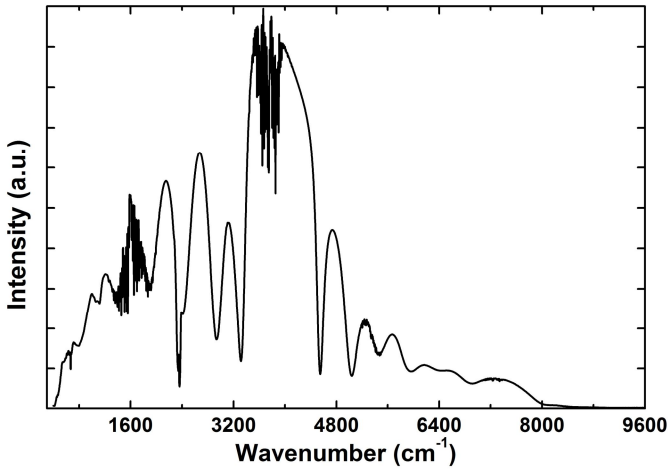

Figure 6.16. Reflection signal measured from a ZnTe/GaSb DBR sample.

Then the reflectance of the DBR samples is given by

$$R(DBR) = \frac{Signal(DBR)}{Signal(Au)} \cdot R(Au), \tag{6.35}$$

where R represents reflectance and Signal(DBR) and Signal(Au) are directly extracted from measurements. Finally, the reflectance of the DBR samples are determined. The reflectance spectrum for a ZnTe/GaSb DBR sample consisting of 7 periods (sample #5) is plotted in Figure 6.17.

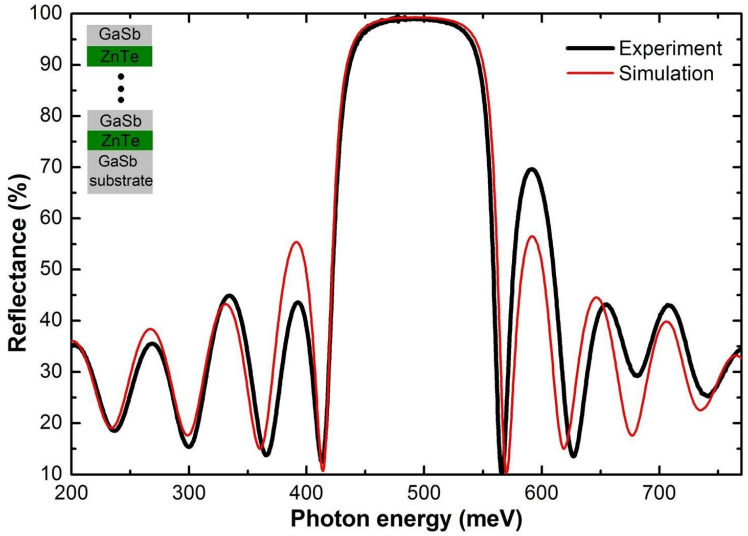

Figure 6.17. Measured and simulated reflectance spectra for sample #5 [147].

As visible in Figure 6.17, the measurement results show a peak reflectance of 99.0% with a wide stopband of 480 nm centered at 2.5 μm. Compared the experimental data with the simulated reflectance spectrum, an excellent agreement is obtained in terms of peak reflectivity (99.3%), bandwidth of photonic stopband (481nm), and sidelobe positions.

6.7 Summary

ZnTe/GaSb DBR structure is proposed for various optoelectronic device applications. An optical model is built to study the reflectance properties for the proposed DBR structure. The modeling results show a reflectance as high as 99.9% can be expected from ZnTe/GaSb DBRs with only 10 periods. Successful growth of high quality ZnTe/GaSb DBRs have been demonstrated on GaSb (001) substrates using MBE. High-resolution XRD patterns show clear Pendellösung fringes from the grown samples. The layer thicknesses measured by SEM are in close agreement with the estimates based on the growth rates. AFM and TEM

images show overall excellent surface morphology, crystallinity and highly coherent interfaces. A peak reflectance of 99% with a wide stopband of 480 nm centered at 2.5 μm is experimentally confirmed from a sample with 7 DBR pairs. Therefore, it is reasonable to conclude that the ZnTe/GaSb DBR structures are suitable for use in VCSELs and other optoelectronic applications.

Chapter 7

CONCLUSION

Optoelectronic materials and devices have been developed with decades of persistent effort by the global physics and engineering communities. It is still extremely challenging to integrate all of them monolithically without scarifying device performance. Up to now, materials grown on different substrates are still commonly used for devices working in different spectral ranges. To achieve integration of all devices and systems on a single substrate, many innovative buffer layers and hybrid integration methods have been proposed and studied. However, there still remains a lack of closely lattice-matched materials and substrates suitable for the grand integration of photonic devices and systems.

In order to address this issue from its root, a new materials system was recently proposed which consists of 6.1 Å II-VI (MgZnCdHg)(SeTe) and III-V (InGaAl)(AsSb) semiconductors on lattice-matched GaSb and InAs substrates. These semiconductor binaries and their alloys have direct bandgaps covering the entire energy spectrum from far IR (~0 eV) to UV (~3.4eV). Among these materials, ZnTe and GaSb are II-VI and III-V compounds which are very well latticed-matched with lattice mismatch of only 0.13%. They form heterostructures which are found of unique properties desirable for various electronic and optoelectronic devices. This thesis work reports experimental studies on material properties of MBE-grown ZnTe and GaSb for 6.1 Å semiconductor integration.

Thick ZnTe layers grown on III-V substrates as low-cost virtual substrates are proposed. ZnTe samples are grown on GaAs, InP, InAs and GaSb (001) substrates using molecular beam epitaxy (MBE). During growth, reflection-high-energy electron diffraction (RHEED) pattern is monitored for growth optimization. After completion of the growth, high-resolution X-ray diffraction (XRD) and transmission electron microscopy (TEM) are used to characterize the structural properties, and photoluminescence (PL) is used to characterize the optical properties. XRD analysis indicates there are residual tensile strains in ZnTe epilayers due to the difference in thermal expansion coefficients between the ZnTe epilayers and the different substrate materials. TEM images reveal the presence of Lomer edge and 60° partial dislocations at the interfaces between ZnTe epilayers and GaAs and InP substrates. Visible photoluminescence from ZnTe epilayers is observed from 80 to 300 K.

Heterostructures consisting of GaSb on ZnTe are proposed for use in various electronic and optoelectronic device applications. By using MBE, high-quality GaSb is grown on ZnTe under a temperature ramp during growth. The influence of the temperature ramp on material properties is investigated. During growth, RHEED pattern shows rapid and smooth transition from ZnTe surface reconstruction to GaSb surface reconstruction. Post-growth structural characterization using XRD and TEM reveals smooth interface morphology and low defect density. Strong photoluminescence emission is observed up to 200 K. The sample grown with a temperature ramp from 360 to 470 °C at a rate of 33

°C/min shows the narrowest bound exciton emission peak with a full width at half maximum of 15 meV.

After high quality of GaSb grown on ZnTe is achieved, the concept of GaSb/ZnTe double-heterostructures (DH) for light emitting devices is proposed. A series of GaSb/ZnTe DH structure samples are successfully grown by MBE on GaSb (001) substrates. During the growth of GaSb on ZnTe, the optimized temperature ramp found previously is applied for the region near the GaSb/ZnTe interface to protect the material from damage due to thermal evaporation. Post-growth characterization using high-resolution XRD and TEM reveals low defect density and coherent interface morphology. Strong photoluminescence emission is observed at temperatures up to 200 K, indicating good optical properties.

Since ZnTe and GaSb show a large refractive index contrast (Δn=1.18 at 0.6 eV), the DBR structure consisting of ZnTe and GaSb can provide very high reflectivity with fewer pairs of quarter-wavelength ($\lambda/4$) layers. Calculations using a transmission matrix optical model show that a reflectivity as high as 99.9% with only 10 pairs of $\lambda/4$ layers can be achieved for ZnTe/GaSb DBRs at 2.3 μm. Meanwhile, the thickness of overall DBR structure can be significantly reduced. After a set of DBR samples are grown, characterization using XRD, SEM, AFM and TEM techniques shows well-defined flat ZnTe/GaSb interfaces, smooth surface and overall excellent interface morphology. The reflectance measurement results show a peak reflectance close to unity (~ 99.0%) is achieved with a wide

stopband of 480 nm centered at 2.5 μm, which are also in an excellent agreement with simulated reflectance spectra.

REFERENCES

[1] H. Amano, N. Sawaki, I. Akasaki and Y. Toyoda, Appl. Phys. Lett. **48**, 353 (1986).

[2] H. Morkoç, S. Strite, G. B. Gao, M. E. Lin, B. Sverdlov, and M. Burns, J. Appl. Phys. **76**, 1363 (1994).

[3] S. Nakamura, T. Mukai, and M. Senoh, Appl. Phys. Lett. **64**, 1687 (1994).

[4] S. Nakamura, M. Senoh, S. Nagahama, N. Iwasa, T. Yamada, T. Matsushita, H. Kiyoku, and Y. Sugimoto, Jpn. J. Appl. Phys. **35**, L74 (1996).

[5] A. Osinsky, S. Gangopadhyay, R. Gaska, B. Williams, M. A. Khan, D. Kuksenkov, and H. Temkin, Appl. Phys. Lett. **71**, 2334 (1997).

[6] G. Parish, S. Keller, P. Kozodoy, J. P. Ibbetson, H. Marchand, P. T. Fini, S. B. Fleischer, S. P. DenBaars, U. K. Mishra, and E. J. Tarsa, Appl. Phys. Lett. **75**, 247 (1999).

[7] S. Strite and H. Morkoç, J. Vac. Sci. Technol. **10,** 1237 (1992).

[8] K. Iga, F. Koyama, and S. Kinoshita, IEEE J. Quantum Electron. **24**, 1845 (1988).

[9] H. Soda, K. Iga, C. Kitahara, and Y. Suematsu, Jpn. J. Appl. Phys. **18**, 2329 (1979).

[10] F. Koyama, S. Kinoshita, and K. Iga, Appl. Phys. Lett. **55**, 221 (1989).

[11] A. Ibaraki, K. Kawashima, K. Furusawa, T. Ishikawa, T. Yamagushi, and T. Niina, Jpn. J. Appl. Phys. **28**, L667 (1989).

[12] J. L. Jewell, J. P. Harbison, A. Scherer, Y. H. Lee, and L. T. Florez, IEEE J. Quantum Electron. **27**, 1332 (1991).

[13] Y. Sakakibara, H. Higuchi, E. Oomura, Y. Nakajima, Y. Yamamoto, K. Goto, H. Namizaki, K. Ikeda, and W. Susaki, J. Lightwave Technol. **LT-3**, 978 (1985).

[14] K. Imanaka, H. Horikawa, A. Matoba, Y. Kawai, and M. Sakuta, Appl. Phys. Lett. **45**, 282 (1984).

[15] H. Horikawa, S. Oshiba, A. Matoba, and Y. Kawai, Appl. Phys. Lett. **50**, 374 (1987).

[16] B. F. Levine, C. G. Bethea, G. Hasnain, V. O. Shen, E. Pelve, R. R. Abbott, and S. J. Hseih, Appl. Phys. Lett. **56**, 851 (1990).

[17] S. D. Gunapala, B. F. Levine, D. Ritter, R. A. Hamm, and M. B. Panish, J. Appl. Phys. **71**, 2458 (1992).

[18] B. F. Levine, A. Zussman, S. D. Gunapala, M. T. Asom, J. M. Kuo, and W. S. Hobson, J. Appl. Phys. **72**, 4429 (1992).

[19] L. Esaki and R. Tsu, IBM J. Res. Dev. **14**, 61 (1970).

[20] G. A. Sai-Halasz, R. Tsu, and L. Esaki, Appl. Phys. Lett. **30**, 651 (1977).

[21] H. Sakaki, L. L. Chang, G. Sai-Halasz, C. A. Chang, and L. Esaki, Solid State Commun. **26**, 589 (1978).

[22] E. R. Gertner, W. E. Tennant, J. D. Blackwell, and J. P. Rode, J. Cryst. Growth **72,** 462 (1985).

[23] A. Million, N. K. Dhar, J. H. Dinan, J. Cryst. Growth **159**, 76 (1996).

[24] J. M. Arias, R. E. DeWames, S. H. Shin, J. G. Pasko, J. S. Chen, and E. R. Gertner, Appl. Phys. Lett. **54**, 1025 (1989).

[25] J. M. Arias, S. H. Shin, J. G. Pasko, R. E. DeWames, and E. R. Gertner, J. Appl. Phys. **65**, 1747 (1989).

[26] Y.-H. Zhang, S.-N. Wu, D. Ding, S.-Q. Yu, and S. R. Johnson, Proceedings of 33rd IEEE PVSC, p.20 (2008).

[27] S.-N. Wu, D. Ding, S. R. Johnson, S.-Q. Yu, and Y.-H. Zhang, Prog. Photovoltaics **18**, 328 (2010).

[28] Y.-H. Zhang, "6.1 Å II-VI and III-V materials: A platform for photovoltaic and IR device applications", The 15th International Conference on II-VI Compounds, Mexico, 2011.

[29] S. Kamuro, C. Hamaguchi, M. Fukushima, J. Nakai, Solid State Electron. **14**, 1183 (1971).

[30] Y. Tokumitsu, A. Kawabuchi, H. Kitayama, T. Imura, Y. Osaka, F. Nishiyama, J. Appl. Phys. **66**, 896 (1989).

[31] H. Dumont, J.-E. Bourée, A. Marbeuf, O. Gorochov, J. Crystal Growth **130,** 600 (1993).

[32] H. Leiderer, G. Jahn, M. Silberbauer, W. Kuhn, H. P. Wagner, W. Limmer, W. Gebhardt, J. Appl. Phys. **70,** 398 (1991).

[33] Y. Rajakarunanayake, B. H. Cole, J. O. McCaldin, D. H. Chow, J. R. Söderström, T. C. McGill, C. M. Jones, Appl. Phys. Lett. **55,** 1217 (1989).

[34] C. T. Chou, J. L. Hutchison, D. Cherns, M.-J. Casanove, J. W. Steeds, R. Vincent, B. Lunn, D. A. Ashenford, J. Appl. Phys. **74,** 6566 (1993).

[35] D. L. Mathine, S. M. Durbin, R. L. Gunshor, M. Kobayashi, D. R. Menke, Z. Pei, J. Gonsalves, N. Otsuka, Q. Fu, M. Hagerott, A. V. Nurmikko, Appl. Phys. Lett. **55,** 268 (1989).

[36] S. Wang, D. Ding, X. Liu, X.-B. Zhang, D. J. Smith, J. K. Furdyna, and Y.-H. Zhang, J. Cryst. Growth **311**, 2116 (2009).

[37] W. L. Bragg, Proc. R. Soc. London A **89**, 248 (1913).

[38] M. von Laue, Ann. der Physik **56**, 497 (1918).

[39] C. G. Darwin, Philos. Mag. **27**, 315 (1914).

[40] P. P. Ewald, Ann. der Physik **54**, 519 (1917).

[41] M. Deutsch and M. Hart, Phys. Rev. B **26**, 5558 (1982).

[42] N. Maskil and M. Deutsch, Phys. Rev. A **37**, 2947 (1988).

[43] D. Keith Bowen and Brian K. Tanner, High Resolution X-ray Diffractometry and Topography (Taylor & Francis, London, 1998).

[44] J. J. Thomson, Conductivity of Electricity through Gases (Cambridge Univeristy Press, Cambridge, 1906).

[45] J. M. Cowley, International Tables for X-ray Crystallography, edited by A. J. C. Wilson, (Kluwer, Dordrecht/Bosten/London, 1992).

[46] C. T. Chantler, J. Phys. Chem. Ref. Data **24**, 71 (1995).

[47] M. Fatemi, J. Cryst. Growth **96**, 316 (1989).

[48] D. K. Bowen and B. K. Tanner, J. Appl. Cryst. **28**, 753 (1995).

[49] P. F. Fewster, J. Appl. Cryst. **22**, 64 (1989).

[50] P. F. Fewster, Crit. Rev. Solid State Mater. Sci. **22**, 69 (1997).

[51] W. Van Roosbroeck and W. Shockley, Phys. Rev. **94**, 1558 (1954).

[52] W. Shockley and W. T. Read, Phys. Rev. **87**, 835 (1952).

[53] A. Haug, Solid-State Electron. **21**, 1281 (1978).

[54] L. M. Blinov, E. A. Bobrowa, V. S. Vavilov, and G. N. Galkin, Sov. Phys.-Solid State **9**, 2537 (1968).

[55] K. G. Svantesson, N. G. Nilsson, and L. Huldt, Solid State Commun. **9**, 213 (1971).

[56] R. Conradt and J. Aengenheister, Solid State Commun. **10**, 321 (1972).

[57] A. R. Beattie and P. T. Landsberg, Proc. R. Soc. London A **249**, 16 (1959).

[58] D. Hill and P. T. Landsberg, Proc. R. Soc. London A **347**, 547 (1976); **347**, 565 (1976).

[59] K. Sato, M. Hanafusa, A. Noda, A. Arakawa, M. Uchida, T. Asahi, and O. Oda, J. Cryst. Growth **214**, 1080 (2000).

[60] J. H. Chang, T. Takai, K. Godo, J. S. Song, B. H. Koo, T. Hanada, and T. Yao, Phys. Status Solidi (b) **229**, 995 (2002).

[61] S. Adachi, Handbook on Physical Properties of Semiconductors (Kluwer, Boston, 2004), Vol. II: III-V Compound Semiconductors.

[62] J. Fan, L. Ouyang, X. Liu, D. Ding, J. K. Furdyna, D. J. Smith, and Y.-H. Zhang, J. Cryst. Growth, **323**, 127 (2011).

[63] S. Adachi, Properties of Group-IV III-V and II-VI Semiconductor (Wiley, West Sussex, England, 2005).

[64] V. H. Etgens, M. Sauvagesimkin, R. Pinchaux, J. Massies, N. Jedrecy, A. Waldhauer, S. Tatarenko, and P. H. Jouneau, Phys. Rev. B **47**, 16 (1993).

[65] P. Tomasini, A. Haidoux, M. Maurin, and J. C. Tedenac, J. Cryst. Growth **166**, 590 (1996).

[66] Wikipedia: The Free Encyclopedia, Wikimedia Foundation, Inc., <http://en.wikipedia.org/wiki/ Transmission_electron_microscopy>

[67] L. Ouyang, J. Fan, S. Wang, X. Lu, Y.-H. Zhang, X. Liu, J. K. Furdyna, and D. J. Smith, J. Cryst. Growth **330**, 30 (2011).

[68] C. F. Bohren, D. R. Huffman, Absorption and Scattering of Light by Small Particles (Wiley, New York, 1983).

[69] W. Lee, S. Kim, S. Choi, H. Lee, S. Lee, S. Park, T. Yao, J. Song, H. Ko, and J. Chang, J. Cryst. Growth **305**, 40 (2007).

[70] S. Kim, W. Lee, M. Jung, J. Chang, A. K. Nyi, H. Lee, J. Song, D. Oh, S. Park, and T. Yao, Appl. Surf. Sci. **256**, 1261 (2009).

[71] J. Fan, L. Ouyang, X. Liu, D. Ding, J. K. Furdyna, D. J. Smith, and Y.-H. Zhang, J. Vac. Sci. Technol. B, **30**, 02B122 (2012).

[72] F. Capasso, M. B. Panish and S. Sumski, IEEE J. Quantum Electron. **17**, 273 (1981).

[73] C. Woelk and K. W. Benz, J. Cryst. Growth **27**, 177 (1974).

[74] C. Heinz and W. Schmidt, J. Cryst. Growth **67**, 393 (1984).

[75] S. S. Chandvankar and B. M. Arora, J. Cryst. Growth **80**, 69 (1987).

[76] C. Anayama, T. Tanahashi, H. Kuwatsuka, S. Nishiyama, S. Isozumi, and K. Nakajima, Appl. Phys. Lett. **56**, 239 (1990).

[77] Y. Takeda, S. Noda, and A. Sasaki, Appl. Phys. Lett. **45**, 656 (1984).

[78] Y. Takeda, S. Noda, K. Nakashima, and A. Sasaki, J. Electron. Mater. **13**, 855 (1984).

[79] M. Lee, D. J. Nicholas, K. E. Singer, and B. Hamilton, J. Appl. Phys. **59**, 2895 (1986).

[80] C. Benoit a la Guillaume and P. Lavallard, Phys. Rev. B **5**, 4900 (1972).

[81] W. Rühle, W. Jakowetz, C. Wölk, R. Linnebach, and M. Pilkuhn, Phys. Status Solidi (b) **73**, 255 (1976).

[82] W. Jakowetz, W. Rühle, K. Breuninger, and M. Pilkuhn, Phys. Status Solidi (a) **12**, 169 (1972).

[83] M.-C. Wu and C.-C. Chen, J. Appl. Phys. **72**, 4275 (1992).

[84] G. E. Pikus and G. L. Bir, Fiz. Tverd. Tela (Leningrad) **1**, 1642 (1959) [Sov. Phys. Solid State **1**, 1502 (1960)].

[85] S. L. Chuang, Phys. Rev. B **43**, 9649 (1991).

[86] S. L. Chuang, *Physics of Optoelectronic Devices*, (Wiley, New York, 1995).

[87] Z. I. Alferov, Rev. Mod. Phys. **73**, 767 (2001).

[88] H. Kroemer, Rev. Mod. Phys. **73**, 783 (2001).

[89] W. Shockley, "Circuit element utilizing semiconductor material", U.S. Patent 2 269 347, Sept, 25, 1951.

[90] H. Kroemer, Proc. IRE. **45**, 1535 (1957).

[91] H. Kroemer, RCA Rev. **28**, 332 (1957).

[92] H. Kroemer, Proc. IEEE **51**, 1782 (1963).

[93] Z. I. Alferov and R. F. Kazarinov, "Semiconductor laser with electric pumping", Inventor's Certificate 181737 [in Russian], Appli. 950840, priority as of March 30, 1963.

[94] Z. I. Alferov, V. M. Andreev, E. L. Portnoy, and M. K. Trukan, Fiz. Tekh. Poluprovodn. **3**, 1328 (1969) [Sov. Phys. Semicond. **3**, 1107 (1970)].

[95] Z. I. Alferov, V. M. Andreev, D. Z. Garbuzov, Y. V. Zhilyaev, E. P. Morozov, E. L. Portnoi, and V. G. Trofim, Fiz. Tekh. Poluprovodn. **4**, 1826 (1970) [Sov. Phys. Semicond. **4**, 1573 (1971)].

[96] M. A. Haase, J. Qiu, J. M. DePuydt, and H. Cheng, Appl. Phys. Lett. **59**, 1272 (1991).

[97] H. Jeon, J. Ding, W. Patterson, A. V. Nurmikko, W. Xie, D. C. Grillo, M. Kobayashi, and R. L. Gunshor, Appl. Phys. Lett. **59**, 3619 (1991).

[98] A. Ishibashi, IEEE J. Sel. Top. Quantum Electron. **1**, 741 (1995).

[99] Z. I. Alferov, V. M. Andreev, V. I. Korol'kov, E. L. Portnoi, and D. N. Tret'yakov, Fiz. Tekh. Poluprovodn. **2**, 1545 (1968) [Sov. Phys. Semicond. **2**, 1289 (1969)].

[100] Z. I. Alferov, A. I. Vasil'ev, S. V. Ivanov, P. S. Kop'ev, N. N. Ledentsov, M. E. Lutsenko, B. Y. Mel'tser, and V. M. Ustinov, Pis'maZh. Tekh. Fiz. **14**, 1803 (1988) [Sov. Tech. Phys. Lett. **14**, 782 (1988)].

[101] I. Schinitzer, E. Yablonovitch, C. Caneau, and T. J. Gmitter, Appl. Phys. Lett. **62**, 131 (1993).

[102] F. A. Ponce and D. P. Bour, Nature **386**, 351 (1997).

[103] L. M. Dolginov, L. V. Druzhinina, P. G. Ehseev, A. N. Lapshin, M. G. Mil'vidskii, and B. N. Sverdlov, Sov. J. Quantum Electron. **8**, 416 (1978).

[104] H. K. Choi, S. J. Eglash, and G. W. Turner, Appl. Phys. Lett. **64**, 2474 (1994).

[105] P. S. Dutta, H. L. Bhat, and V. Kumar, J. Appl. Phys. **81**, 5821 (1997).

[106] G. Motosugi and T. Kagawa, Jpn. J. Appl. Phys. **19**, 2303 (1980).

[107] M. B. Z. Morosini, J. L. Herrera-Perez, M. S. S. Loural, A. A. G. Von Zuben, A. C. F. da Silveira, and N. B. Patel, IEEE J. Quantum Electron. **QE-29**, 2103 (1993).

[108] O. Hildebrand, W. Kuebart, K. W. Benz, and M. H. Pilkuhn, IEEE J. Quantum Elelctron. **QE-17**, 284 (1981).

[109] K. Segawa, H. Miki, M. Otsubo, and K. Shirata, Electron. Lett. **12**, 124 (1976).

[110] C. Hilsum and H. D. Rees, Electron. Lett. **6**, 277 (1970).

[111] L. M. Fraas, G. R. Girard, J. E. Avery, B. A. Arau, V. S. Sundaram, A. G. Thompson, and J. M. Gee, J. Appl. Phys. **66**, 3866 (1989).

[112] J. Fan, L. Ouyang, X. Liu, J. K. Furdyna, D. J. Smith, and Y.-H. Zhang, "GaSb/ZnTe double-heterostructures grown using molecular beam epitaxy", submitted for publication to J. Cryst. Growth.

[113] E. A. Kraut, R. W. Grant, J. R. Waldrop, and S. P. Kowalczyk, Phys. Rev. Lett. **44**, 1620 (1980).

[114] P. Zurcher and R. S. Bauer, J. Vac. Sci. Technol. **1**, 695 (1983).

[115] A. D. Katnani and G. Margaritondo, Phys. Rev. B **28**, 1944 (1983).

[116] R. H. Miles, J. O. McCaldin, and T. C. McGill, J. Cryst. Growth **85**, 188 (1987).

[117] E. T. Yu, M. C. Philips, J. O. McCaldin, and T. C. McGill, J. Vac. Sci. Technol. B **9**, 2233 (1991).

[118] T. M. Duc, C. Hsu, and J. P. Faurie, Phys. Rev. Lett. **58**, 1127 (1987).

[119] S.-H. Wei, S. B. Zhang, and A. Zunger, J. Appl. Phys. **87**, 1304 (2000).

[120] W. G. Wilke and K. Horn, J. Vac. Sci. Technol. B **7**, 807 (1989).

[121] E. T. Yu, M. C. Phillips, D. H. Chow, D. A. Collins, M. W. Wang, J. O. McCaldin, and T. C. McGill, Phys. Rev. B **46**, 13379 (1992).

[122] C. R. Li, B. K. Tanner, D. E. Ashenford, J. H. C. Hogg, and B. Lunn, J. Appl. Phys. **82**, 2281 (1997).

[123] M. P. Halsall, D. Wolverson, J. J. Davies, B. Lunn, and D. E. Ashenford, Appl. Phys. Lett. **60**, 2129 (1992).

[124] J. W. Matthews and A. E. Blakeslee, J. Cryst. Growth **27**, 118 (1974); **29**, 273 (1975); **32**, 265 (1976).

[125] D. J. Dunstan, S. Young, and R. H. Dixon, J. Appl. Phys. **70**, 3038 (1991).

[126] G. Cohen-Solal, F. Bailly, and M. Barbe, J. Cryst.Growth **138**, 68 (1994).

[127] P. Tomasini, A. Haidoux, J. Domagala, J. Tedenac, M. Maurin, and B. Ducourant, J. Cryst. Growth **165**, 203 (1996).

[128] J. Chai, O. C. Noriega, J. H. Dinan, and T. H. Myers, J. Electron. Mater. Doi: 10.1007/s11664-012-2120-8, (2012).

[129] K. Iga: Laboratory Notebook (March 22, 1977).

[130] K. Iga, S. Ishikawa, S. Ohkouchi, and T. Nishimura, Appl. Phys. Lett. **45**, 348 (1984).

[131] R. Geels and L. A. Coldren, 12th IEEE Int. Semiconductor Laser Conf. **B1**, 16 (1990).

[132] T. Wipiejewski, K. Panzlaf, E. Zeeb, and K. J. Ebeling, 18th European Conf. Opt. Comn. **92**, PDII-4, (1992).

[133] Y. H. Lee, B. Tell, K. F. Brown-Goebeler, R. E. Leibenguth, and V. D. Mattera, IEEE Photon. Technol. Lett. **3**, 108 (1991).

[134] K. D. Choquette, R. P. Schneider, M. H. Crawford, K. M. Geib, and J. J. Figiel, Electron. Lett. **31**, 1145 (1995).

[135] T. Baba, Y. Yogo, K. Suzuki, F. Koyama, and K. Iga, Electron. Lett. **29**, 913 (1993).

[136] K. Iga, Int. Symp. Blue Laser Light Emitting Diodes, **Th-11**, 263, (1996).

[137] K. Sebald, C. Kruse, and J. Wiersig, Phys. Status Solidi (b) **246**, 255 (2009).

[138] K. Iga, IEEE J. Sel. Top. Quantum Electron. **6**, 1201 (2000).

[139] K. Iga, Jpn. J. Appl. Phys. **47**, 1 (2008).

[140] C. Lei, T. J. Rogers, D. G. Deppe, and B. G. Streetman, J. Appl. Phys. **69**, 7430 (1991).

[141] J. J. Dudley, D. I. Babic, R. Mirin, L. Yang, B. I. Miller, R. J. Ram, T. Reynolds, E. L. Hu, and J. E. Bowers, Appl. Phys. Lett. **64**, 1463, (1994).

[142] M. H. M. Reddy, T. Asano, R. Koda, D. A. Buell, and L. A. Coldren, Electron. Lett. **38**, 1181 (2002).

[143] C.-K. Lin, D. P. Bour, J. Zhu, W. H. Perez, M. H. Leary, A. Tandon, S. W. Corzine, and M. R. T. Tan, IEEE J. Sel. Top. Quantum Electron. **9**, 1415 (2003).

[144] M. Ortsiefer, G. Böhm, M. Grau, K. Windhorn, E. Rönnerberg, J. Rosskopf, R. Shau, O. Dier, and M.-C. Amann, Electron. Lett. **42**, 640 (2006).

[145] A. Ducanchez, L. Cerutti, P. Grech, F. Genty, and E. Tournié, Electron. Lett. **45**, 265 (2009).

[146] L. Cerutti, A. Garnache, A. Ouvrard, M. Garcia, E. Cerda, and F. Genty, Electron. Lett. **40**, 869 (2004).

[147] J. Fan, X. Liu, J. K. Furdyna, and Y.-H. Zhang, "ZnTe/GaSb distributed Bragg reflectors grown on GaSb for mid-wave infrared optoelectronic applications", accepted for publication to Appl. Phys. Lett.

[148] S. Adachi, Optical Constants in Crystalline and Amorphous Semiconductors: Numerical Data and Graphical Information (Kluwer, Boston, 1999).

[149] M. Born and E. Wolf, Principle of Optics, 6th ed., (Pergamon, New York, 1980).